SANDIA REPORT
SAND2012-0480
Unlimited Release
Printed March 2012

Radar-Cross-Section Reduction of Wind Turbines (Part 1)

Jacob J. McDonald, Billy C. Brock, Steven E. Allen, Paul G. Clem, Joshua A. Paquette, Ward E. Patitz, William K. Miller, David A. Calkins, and Hung "Jacques"Loui

Prepared by
Sandia National Laboratories
Albuquerque, New Mexico 87185 and Livermore, California 94550

Sandia National Laboratories is a multi-program laboratory managed and operated by Sandia Corporation, a wholly owned subsidiary of Lockheed Martin Corporation, for the U.S. Department of Energy's National Nuclear Security Administration under contract DE-AC04-94AL85000.

Sandia National Laboratories

Issued by Sandia National Laboratories, operated for the United States Department of Energy by Sandia Corporation.

Available to DOE and DOE contractors from
U.S. Department of Energy
Office of Scientific and Technical Information
P.O. Box 62
Oak Ridge, TN 37831

Telephone: (865) 576-8401
Facsimile: (865) 576-5728
E-Mail: reports@adonis.osti.gov
Online ordering: http://www.osti.gov/bridge

Available to the public from
U.S. Department of Commerce
National Technical Information Service
5285 Port Royal Rd.
Springfield, VA 22161

Telephone: (800) 553-6847
Facsimile: (703) 605-6900
E-Mail: orders@ntis.fedworld.gov
Online order: http://www.ntis.gov/help/ordermethods.asp?loc=7-4-0#online

SAND2012-0480
Unlimited Release
March 2012

Radar-Cross-Section Reduction of Wind Turbines (Part 1)

Jacob J. McDonald, Billy C. Brock, Ward E. Patitz, Steven E. Allen, Hung "Jacques" Loui
SAR Sensor Technologies Department, Microwave Imaging Systems

Paul G. Clem
Ceramic Processing & Inorganic Department, Materials Synthesis & Processing

Joshua A. Paquette
Wind Energy Technologies Department, Renewable Energy Technologies

William K. Miller, David A. Calkins
Organic Materials Department, Manufacturing Process Science & Technology

Sandia National Laboratories
P.O. Box 5800
Albuquerque, NM 87185-0533

Abstract

In recent years, increasing deployment of large wind-turbine farms has become an issue of growing concern for the radar community. The large radar cross section (RCS) presented by wind turbines interferes with radar operation, and the Doppler shift caused by blade rotation causes problems identifying and tracking moving targets. Each new wind-turbine farm installation must be carefully evaluated for potential disruption of radar operation for air defense, air traffic control, weather sensing, and other applications. Several approaches currently exist to minimize conflict between wind-turbine farms and radar installations, including procedural adjustments, radar upgrades, and proper choice of low-impact wind-farm sites, but each has problems with limited effectiveness or prohibitive cost. An alternative approach, heretofore not technically feasible, is to reduce the RCS of wind turbines to the extent that they can be installed near existing radar installations. This report summarizes efforts to reduce wind-turbine RCS, with a particular emphasis on the blades. The report begins with a survey of the wind-turbine RCS-reduction literature to establish a baseline for comparison. The following topics are then addressed: electromagnetic model development and validation, novel material development, integration into wind-turbine fabrication processes, integrated-absorber design, and wind-turbine RCS modeling. Related topics of interest, including alternative mitigation techniques (procedural, at-the-radar, etc.), an introduction to RCS and electromagnetic scattering, and RCS-reduction modeling techniques, can be found in a previous report.

Acknowledgment

The authors would like to thank Jose Zayas and David Minster of Sandia's Wind and Water Power Technologies Department for providing the opportunity to undertake this project, and Kurt Sorensen of Sandia's SAR Sensor Technologies Department for his technical and managerial leadership. We also would like to acknowledge Brian Resor of Sandia's Wind and Water Power Technologies Department for providing the detailed blade model needed for electromagnetic simulation, David Adams of Sandia's Advanced Prototyping Science and Technology Department for providing titanium depositions, and Eric Spoerke of Sandia's Electronic Materials & Nanostructures Department for constructing integrated materials for GR900 characterization.

Contents

1. Introduction and Summary

The wind-turbine industry has successfully followed an evolutionary process moving toward minimum cost, minimum weight, and high-efficiency designs, but interference caused by large wind-turbine farms to radar installations remains problem. This report summarizes recent and on-going effort by Sandia National Laboratories (SNL) to reduce the radar cross section (RCS) of wind turbines, with particular emphasis on the blades. The RCS-reduction structures described in this work are intended for direct integration into the wind-turbine blade with minimal cost and performance impact. The intent is to develop treatments capable of being integrated into the standard construction methods currently in use for manufacturing the blades. Some objectives of this effort include:

- Understanding the radar-to-wind-turbine interaction problem and potential mitigation techniques suitable for application at the turbine;
- Developing wind-turbine radar-cross-section modeling capability for the purpose of understanding the turbine's radar signature and evaluating RCS-reduction approaches;
- Developing and evaluating radar-absorbing materials (RAM); and
- Demonstrating that effective RAM can be integrated into blade-fabrication process.

A prior study of wind-turbine RCS mitigation, in combination with the literature review included in the section titled *Wind-turbine RCS Problem and Background Material*, establishes the baseline for this effort. The literature review describes the state-of-the-art in absorber design, and further investigation confirms that thin external coatings of radar-absorbing material (RAM) are insufficient to reduce blade RCS at frequencies of interest (L- and S-band) [1]. Significant RCS reduction at these frequencies requires a relatively thick multilayer absorber [2]. We describe our approach for designing a multilayer absorber that can be integrated into a wind-turbine blade without severely impacting cost and aerodynamic performance. This effort has been divided into several primary tasks as described below:

- Electromagnetic-Model Development

  We assembled comprehensive models to establish a foundation for future absorber designs and to enable modeling of complete blades and rotors.
- Model Validation (Measurement Phase 1)

  We have fabricated flat-plate absorber samples to validate our modeling approach.
- Materials Development and Characterization

  We have characterized the electromagnetic properties of existing blade materials, developed new materials to improve absorber performance, and developed and evaluated various RAM configurations.
- Integrated Absorber Design

  Based on RAM configurations developed in this study, we have proposed structures for integrating RAM into the blade fabrication process.
- Integration Validation (Measurement Phase 2)

  We plan to build flat plate samples with realistic blade-fabrication processes to demonstrate manufacturability and effectiveness of integrated RAM design (to be included in Part 2 of this report).
- Turbine-Rotor Model Development

We modeled a 126-meter diameter rotor set to gain insight into turbine radar signature. Both metal and fiber-composite blades were compared, and both static RCS and dynamic Doppler spectra were investigated.

Significant Findings:

The need for minimum cost, minimum weight, and high-efficiency turbine-blade designs means imposing limitations on the freedom of choice for materials and geometry, especially thicknesses available for incorporating the treatment in different portions of the blade. Thus significant constraints are in place, and these constraints have the potential to limit the performance that can be achieved in both the depth of RCS reduction and in the bandwidth over which the treatment is effective. Nevertheless, we believe the path toward integrated absorber designs is the right direction for now. However, we also believe that it is prudent to examine other RCS reduction methods that promise much higher performance, even if they do not initially appear to be readily integrable with current manufacturing methods. To date, minimal effort has been expended on this aspect of our research. During the course of the following discussion, some of those ideas are touched on briefly, and a very brief summary of some of the ideas we are entertaining is included in Appendix I.

Our integrated-absorber designs indicate that 20 dB or greater return loss can be achieved by integrating simple RAM into the existing blade-fabrication processes. However, 20 dB return loss does not necessarily correspond to 20 dB RCS reduction for a complete turbine. It is critical to recognize that wind-turbine RCS cannot be captured by a single number. Several considerations create an array of performance metrics, including Doppler spectra, monostatic RCS, and bistatic RCS, all dependent on radar view angle. Nonetheless, it is expected that the RCS of treated blades will be significantly reduced relative to untreated blades, and consequently Doppler effects will be reduced.

Computing the radar cross section and Doppler spectra of wind turbines entails a number of considerations. The large wind turbines that are of current interest have rotor diameters that measure hundreds or even thousands of wavelengths at radar frequencies. The computation of the RCS for such large objects requires considerable computational resources, in addition to requiring appropriate approximations to the physics of the scattering process. While the computation of the static RCS requires significant computing time, calculating the dynamic Doppler spectra is even more intensive. To avoid aliasing of the Doppler shift, a phenomenon whereby the higher frequencies are mistaken for lower frequencies, the computation must sample the scattered signal at a rate greater than the Nyquist rate, requiring more than two samples per period of the highest Doppler shift present in the scattered signal. This can increase the number of computations required by several orders of magnitude.

The RCS modeling reported here addresses the scattering from the turbine blades alone, without the nacelle, tower, or even the hub joining the blades. This approach provides some simplification and focuses on the critical parts contributing to the Doppler spectra. The blades are modeled with realistic composite dielectric materials, not perfect electrical conductors (PEC) as is often the case. In fact, it is demonstrated that the use of PEC instead of realistic dielectric materials can produce misleading results, with predicted Doppler shifts for PEC models as much as 10-20 dB lower than for the dielectric models.

This study has also demonstrated that internal components of the turbine blade can provide significant, even dominant, contributions to the Doppler spectrum when the blade is made of fiberglass composites, a result that would not have been discovered had the blade been modeled with only PEC materials. However, this work has also shown that correct modeling of the blade using dielectric composites is considerably more costly in terms of computing resources. Consequently, some methods for improving the speed of computation have been identified and are discussed briefly.

The RCS computations have also shown that, while certain structures such as the spar caps may dominate the RCS at some aspect angles, all components of the blade will require some RCS-mitigation treatment if substantial reduction in the RCS and associated Doppler spectra is to be obtained. Importantly, this work has demonstrated that single-number simplistic descriptions of the RCS performance and RCS reduction are of very limited use. The complexity of the static RCS and the Doppler spectra as the radar position is varied indicate the need for complete system-level simulation of specific radar's responses to wind-turbine scattering to enable the proper assessment of the value of a particular RCS reduction treatment.

Recommendations:

We have demonstrated the feasibility of integrating radar absorbing material into wind-turbine blades in a manner compatible with current fabrication processes. Our designs indicate a significantly reduced RCS can be achieved with even simple modifications to blade structures. In light of these findings, fabrication and testing of a small-scale low-RCS rotor set (9-meter to 13-meter blade length) is recommended to demonstrate RAM compatibility with blade fabrication and to allow evaluation of RCS reduction in an operational environment. In addition, we believe future efforts should focus on the following areas:

- Wind-turbine RCS Modeling

  Significant work remains in the area of wind-turbine RCS modeling. Wind-turbine models require an immense amount of computation, and the characterization of the RCS of wind turbines, including static, Doppler, and multipath effects, is an extremely complex endeavor. Integration with super-computing resources available at SNL would reduce computation times and enable a better understanding of turbine radar signature through more thorough and complete simulations.

  Current absorber designs, though compatible with blade fabrication processes, apply to flat plate structures. The simulation of the radar scattering from absorbers integrated into a blade model would provide insight into achievable RCS reduction for an actual turbine.

- Materials Development

  Resins doped with ferrites, titanates, and glass micro-balloons expand the material options available to RF engineers. Initial progress from this effort should be continued, particularly in the area of integration with blade fabrication processes.

  Carbon has desirable electrical and mechanical properties. Carbon-based materials have been used in EMI, shielding, and absorption, indicating a wide range of electrical properties based on composition (graphene, fullerenes, fibers). As the use of carbon in structural components of large blades increases, finding the appropriate composition for both electrical and aerodynamic design could have immense cost impact.

  Material solutions developed in this study (thin metal deposition, polymer coated fabrics, doped resins) should be further investigated to determine suitability for mass production. The practicality of these technically viable approaches must be determined with regard to size and cost scaling.

- Analysis and Design Process Improvement

  The treatments designed in this study used standard computing resources and electromagnetic design tools. Optimized absorber performance is limited by available optimization techniques, whether random, gradient, or algorithmic, and by computing resources. Development of custom code and integration with supercomputing resources at Sandia would expand available optimization techniques and do more with existing techniques.

- Advanced Electromagnetic Analysis

  Although significant RCS reduction has already been achieved with a Jaumann absorber approach, many experts claim that Circuit Analog Absorbers (CAA) can improve absorber performance for a given thickness [3]. Investigation into CAA approaches could result in further RCS reduction.

  The solutions presented in this report assume a metal backed absorber. Non-metal backed absorbers would allow RF energy to penetrate into the blade structure and possibly pass through the blade. From a radar perspective, transparent turbines are preferred to absorptive turbines, since absorptive turbines would still create a shadow region where radar visibility is low. Electromagnetic analysis becomes significantly more complex for non-metal backed absorbers, but the potential benefits of applying frequency-selective surfaces [3] to make portions of the blade more transparent to radar signals warrants investigation.

  Techniques using periodic structures to create novel electromagnetic behavior are finding increasing application in a wide range of RF systems. Though of limited near-term applicability, these metamaterials and artificial magnetic conductors hold promise for developing new and novel low-observable structures, and should be considered in forward-looking research.

2. Wind-turbine RCS Problem and Background Material

Prior to the generation of new absorber designs and RCS models, a literature review was performed to determine current status and best approaches. In the interest of clarity, the review has been broken into two sections: one addressing general absorber theory, with the other addressing wind-turbine RCS in particular. The *Absorber Theory* section focuses on optimal absorption of radio-frequency (RF) energy without regard to application, whereas the *Wind-turbine RCS Reduction* section addresses RCS considerations and modeling approaches specific to wind-turbine blades. A previous report also contains a substantial literature review on wind-turbine RCS [1].

2.1 Absorber Theory

Since the development of radar in the 1930's and 1940's, avoiding detection by reducing radar signature has been an area of significant military interest. RCS reduction techniques can be categorized in one of two categories: shaping and radar absorbing material [4, 5, 6]. Shaping alters the geometry of a plane, missile, or other object to direct RF energy away from the radar. Shaping can only reduce RCS over a limited range of angles, which is often an effective solution when the target is illuminated by a single radar, and the radar location relative to the target is known (as is often the case for planes flying over radar). RAM, on the other hand, seeks to reduce RCS by absorbing the incident RF energy and converting it to heat. Most RCS reduction techniques use a combination of shaping and RAM. Only RAM was considered for this effort because the wind turbine-blade geometry has significant mechanical and aerodynamic constraints that prevent significant shaping.

RF absorbers and RAM are mature topics in electromagnetics [4, 5, 6]; nonetheless, significant discussion remains regarding what constitutes an optimal absorber. Metrics for absorber performance include:

- Thickness
- Weight
- Reflection Coefficient
- Transmission Coefficient

- Frequency of operation
- Bandwidth
- Angle of Incidence

The comprehensive goal in absorber design is to minimize thickness, weight, and reflection coefficient while maximizing bandwidth over the chosen operating frequencies and angles of incidence. Transmission coefficient is zero for all absorbers discussed in this report, since all absorbers are terminated in a metal backing.

2.1.1 Fundamental Absorber Limits

Before a large set of absorber designs is generated, performance limits should be determined and a figure of merit established to evaluate the quality of each individual design. For each design, the designer must be able to verify that the reflection coefficient achieved over the bandwidth and angles of incidence is near optimal for given thickness, weight, and material constraints. In [2], Rozanov calculated analytic limits for absorber bandwidth and reflection coefficient given absorber thickness and magnetic permeability according to

$$\left|\ln(\rho_0)\right|(\lambda_{\max}-\lambda_{\min}) < 2\pi^2 \sum_i \mu_i d_i, \tag{1.1}$$

in which ρ_0 is the magnitude of the reflection coefficient, $\lambda_{\max}$ and $\lambda_{\min}$ are the maximum and minimum wavelengths, i is the layer number, μ_i is the magnetic permeability of layer i, and d_i is the thickness of layer i. As can be seen from (1.1), and as expected from electromagnetic theory, the following principles apply:

- Increased bandwidth requires increased reflection coefficient, all else being equal
- Increased thickness allows lower frequency operation, all else being equal
- Increased thickness increases bandwidth, all else being equal
- Increased thickness reduces reflection coefficient, all else being equal
- Magnetic materials ($\mu_i > 1$) improve bandwidth and reflection coefficient, all else being equal
- Magnetic materials ($\mu_i > 1$) reduce thickness, all else being equal

These principles are illustrated in Figure 1. The limits derived in [2] strictly apply only at normal incidence. Since absorber treatments integrated into wind turbines must perform over a range of incident angles, the limits shown in Figure 1 have limited applicability. The principles above nonetheless provide an approximate figure of merit for normal incidence and establish several useful design principles. Additional figures of merit will be established in the *Development of Absorptive Treatment* section.

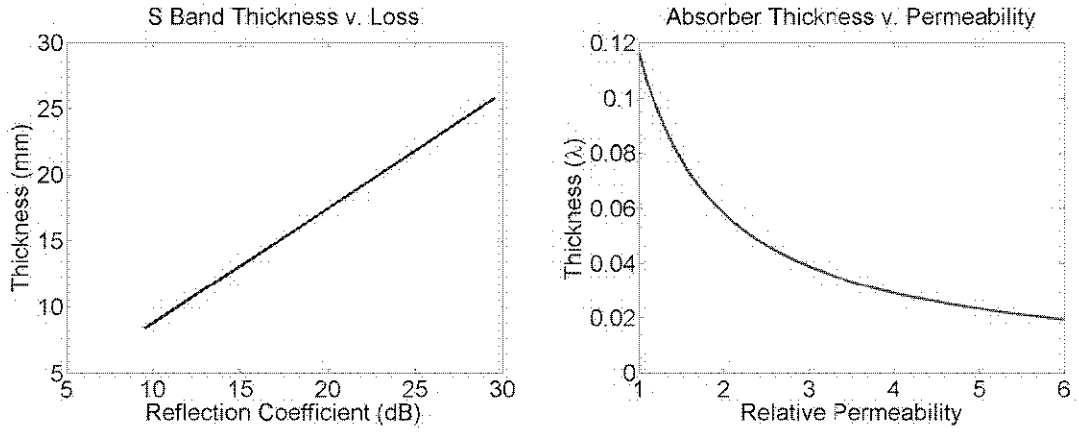

Figure 1 *Absorber performance limitations. Left - Thickness needed for a certain reflection coefficient, all else being equal. Right - Thickness vs. permeability, all else being equal.*

2.1.2 Types of Absorber

Radar absorbing materials can be categorized as either magnetic or non-magnetic. As demonstrated in the previous section, magnetic materials allow significant performance enhancement or thickness reduction. Magnetic materials tend to be extremely heavy and are thus used primarily in applications where weight is not a concern (stationary land-based systems, etc.). Although magnetic materials have not been ruled out *a priori* as a RAM technique for wind turbines, weight constraints indicate that their use will be limited.

Non-magnetic absorbers fall into one of several categories: Jaumann absorbers, Dallenbach absorbers, and circuit-analog absorbers (CAA) [4, 5, 6]. Jaumann absorbers consist of resistive sheets separated by low-loss dielectric materials. In Jaumann absorbers, the resistive sheets convert RF energy to heat, and the dielectric material properties and thickness determine the frequency of operation and bandwidth [7, 8, 9]. Dallenbach absorbers consist of layers of high-loss dielectric material, in which the layered materials both absorb RF energy and determine the frequency of operation [4, 5, 6]. Figure 2 provides a schematic comparison of Jaumann and Dallenbach absorbers.

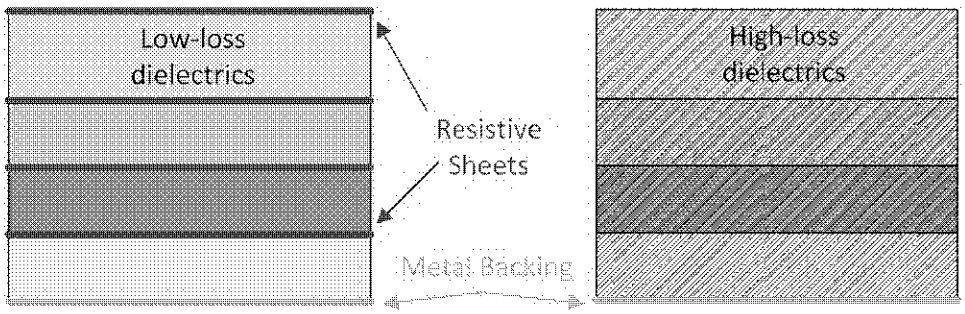

Figure 2 *Schematic comparison of Jaumann and Dallenbach absorbers. Jaumann absorbers confine loss to layer interfaces, whereas Dallenbach absorbers provide continuous loss throughout.*

Circuit-analog absorbers are actually a variant of Jaumann absorbers. Whereas Jaumann absorbers contain uniform resistive sheets, circuit analog absorbers insert sheets consisting of periodic patterned circuits, also known as frequency selective surfaces (FSS), containing both conductive and resistive materials [3, 10, 11, 12, 13, 14, 15, 16, 17, 18, 19, 20]. Figure 3 illustrates some common CAA circuit patterns. These patterns determine equivalent circuit parameters (resistance, inductance, and capacitance) that can be used to reduce

absorber thickness, improve bandwidth, or improve performance over angle of incidence. An absorber can contain more than one of the approaches above (e.g. both Jaumann and Dallenbach, or CAA with magnetic layers); in fact, combining loss mechanisms tends to improve performance at the cost of additional fabrication complexity.

Much debate remains concerning the optimal selection of CAA dielectric constant and resistive or conductive pattern to reduce thickness and weight while maximizing bandwidth and oblique angle performance. Jaumann absorbers, on the other hand, are a mature technology well suited to simple fabrication techniques. Jaumann absorbers are the focus in this effort. Initial comparisons between Jaumann and CAAs did not indicate that the improved electromagnetic performance for CAAs was worth the additional design and fabrication complexity. The capacitive circuit absorber (CCA) concept and associated design processes presented in [10, 11] showed the greatest promise for thin, wideband CAAs. CCAs could be investigated further in future phases to improve electromagnetic performance while maintaining a relatively simple design and fabrication process.

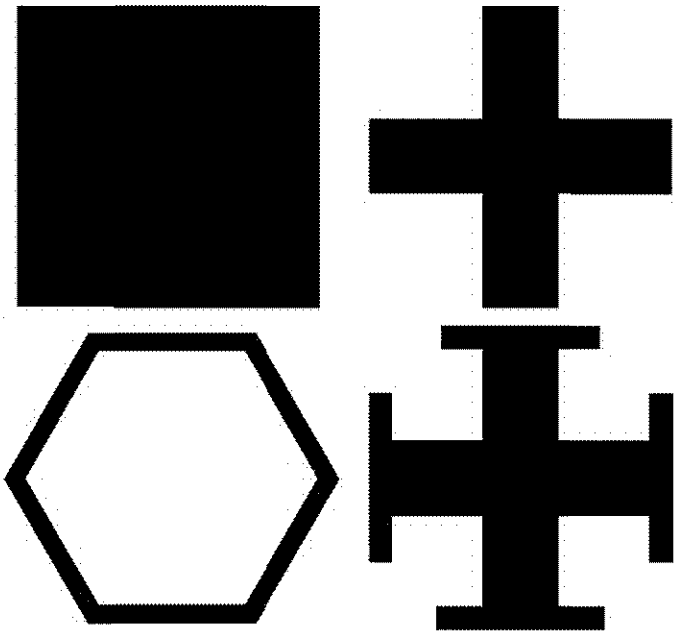

Figure 3 *Common CAA or FSS circuit patterns. Upper left – square patch, upper right – cross, lower right – Jerusalem cross, and lower left – hexagonal loop. Patterns can be conductive, resistive, or a combination of the two.*

In addition to the absorber categories outlined above, significant research continues on the application of metamaterials, artificial magnetic conductors (AMC), and high impedance surfaces to improve absorber performance [21, 22, 23, 24]. Since these technologies remain unproven, further research on their absorber applications was considered beyond the scope of this effort.

2.2 Wind-turbine RCS Reduction

The above discussion illustrates the established state-of-the-art in absorber design and creates metrics for design evaluation. However, actual integration of RAM into a working wind turbine further constrains the design space by limiting material options and constraining fabrication processes. Furthermore, several issues specific to the radar-windfarm problem, such as the impacted radars, turbine-to-turbine RF interaction, and turbine blade aerodynamics, determine the salient performance considerations. A list of design considerations and the practical factors that drive them is provided below:

- Does the absorber need to be broadband or narrowband?

What radars are impacted?
Are said radars broadband or narrowband?
Are multiple radars impacted by a single wind farm?

- Does the absorber need to operate well over a wide range of incident angles?
  Is multipath (turbine-to-turbine RF scattering) a significant factor in interference with radar?
  How does blade curvature and flexing under aerodynamic loads affect absorber performance?
- Does the absorber need to be integrated into the blade construction, or can it be applied externally?
  How well must the blade perform aerodynamically?
  How much cost does RAM add to blade fabrication?
  How much weight and thickness does RAM, external or integrated, add to a blade?

As can be seen from the list above, scope definition and initial assumptions determine the critical performance metrics. To prevent an inappropriate scope, a literature review on radar-windfarm interaction and prior approaches to wind-turbine RCS reduction was performed. RCS reduction of the wind-turbine blades was emphasized, since the demanding weight and aerodynamic constraints make the blade the most difficult component. Solutions that effectively lower blade RCS are likely to be implemented for the tower and nacelle without significant technical difficulty or increased cost.

2.2.1 Radar-Windfarm Interaction

This section attempts to highlight important aspects of the radar-windfarm interaction problem, thus providing a framework for potential solutions, particularly rotor RCS reduction. Studies on radar-windfarm interaction tend to focus on one of two areas: radar operation, with a focus on radar application (air surveillance, weather, or air traffic control), or RF scattering effects of wind turbines. General RF characteristics of wind turbines will be addressed first, followed by impact on specific types of radar.

Numerous studies have characterized wind turbine RF scattering behavior, either in isolation or in a farm [25, 26, 27, 28, 29, 30, 31, 32, 33, 34, 35, 36]. Due to the significant effort required to measure a structure as large as a wind turbine while calibrating for outdoor effects (interfering RF signals, wind speed and direction, etc.), several of these studies are restricted to simulated results. An alternative approach to full-scale measurement is measuring a scaled turbine at higher frequency in a controlled anechoic chamber [28, 35], assuming the high frequency radar signature of a miniaturized turbine mimics that of an actual turbine at low frequency. This is a valid assumption if material properties are stable over frequency, and it appears that turbine RF scattering shows similar behavior at both low and high frequencies.

Several conclusions can be drawn from previous efforts. The predominant scatterer (not considering Doppler effects) is the tower (80%), followed by the nacelle (15%), and blades (5% each). Stationary returns from tower and nacelle could be compensated for in a similar manner to large buildings, but blade rotation creates time-varying Doppler spectra which prevent radar from filtering out rotor returns (see Figure 4). Furthermore, the nacelle and blades rotate to align with the wind, so wind direction changes create unpredictable variations in both radar signature and Doppler spectra. Large, transitory RCS increases occur when the rotating turbine blades pass through certain configurations. Most of these effects apply to backscatter (or monostatic RCS). Forward scatter has received little attention, and bistatic turbine RCS remains largely uninvestigated due to monumental measurement and computational difficulty.

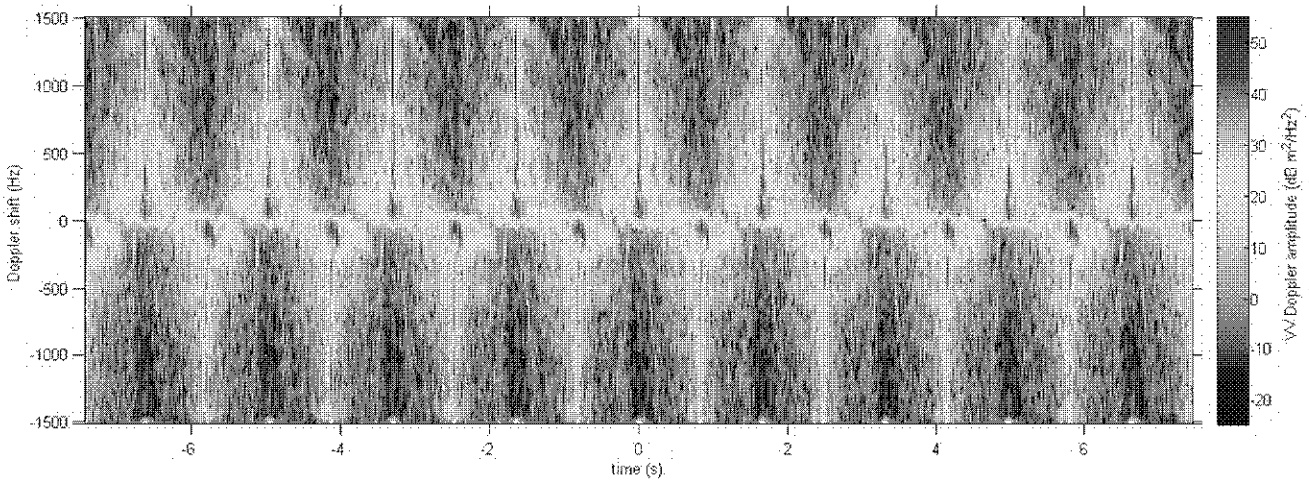

Figure 4 Representative Doppler spectrum, showing monostatic response over time and frequency.

Analysis of wind-turbine scattering has several implications for both radar-based and turbine-based solutions. Radar signal processing needs significant refinement to compensate for Doppler effects and blade flash variations with yaw and blade rotation, but these factors should not complicate absorber design, as long as the absorber bandwidth encompasses a narrow band of Doppler frequencies. Furthermore, perhaps tower and nacelle returns can be filtered out at the radar if the Doppler effect can be addressed by radar absorbing blades. Further studies on bistatic turbine RCS would shed light on multipath effects in a farm environment and help establish performance metrics for absorber designs, in addition to providing valuable insight into turbine spacing to maximize RF signal propagation through wind farms.

Other studies focused on the problem from the radar perspective, with emphasis on empirical analysis of radar performance in the presence of wind farms [37]. Several flight tests have been performed [38, 39, 40, 41, 42, 43, 44, 45, 46] in the presence of large wind farms, and radar performance evaluated. Studies reveal a number of problems created by wind farms, including the creation of shadow regions that hide targets, increased clutter that reduces the likelihood of target detection, and multipath that creates false plots of target location.

Wind farms can create a shadow region in which radar signal does not propagate, as shown in Figure 5. The same phenomenon occurs for large buildings, but wind farms spanning several miles with turbines approaching 200 meters high can create extremely large voids in which the radar system is blind. Diffraction effects reduce shadow region size, indicating appropriate turbine placement can mitigate this problem. Increasing wind farm distance from the radar also reduces shadow region impact.

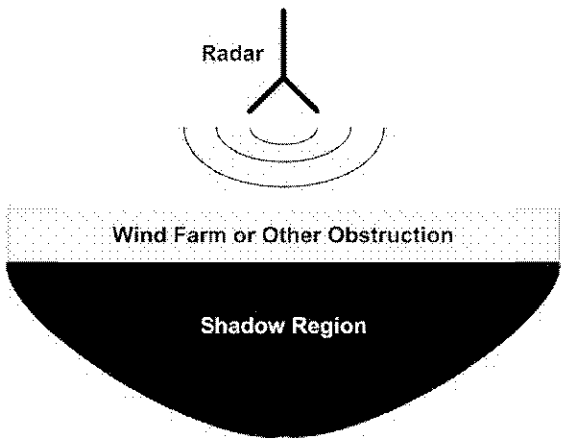

Figure 5 Shadow region caused by obstructions to RF propagation.

Radars operate by transmitting an RF signal from an antenna, and receiving the reflections of that signal from illuminated objects or targets. Clutter consists of reflections off of non-targeted environment (buildings, birds, ground traffic, etc.). Modern radars operate using statistical methods in which a power detection threshold determines the probability that the received signal reflected from a target, as opposed to the non-targeted environment. When the received power crosses a certain threshold (indicating a high target probability), the radar plots and tracks the target. A high detection threshold will cause the radar to miss targets, whereas a low detection threshold will cause the radar to detect non-existent targets, also known as false alarms

Air surveillance and air traffic control share a common goal, to detect and track airborne targets. As a result, windfarms cause similar problems for these two types of radar [47, 48]. Target-tracking radar has numerous performance metrics, with probability of detection, constant false alarm rate, and false plots being the most important. A false alarm is the detection of a target that does not exist. A false plot is the inaccurate mapping of a detected target. High-performance radar maximizes probability of detection and minimizes constant false alarm rate and false plots. Increased clutter raises the detection threshold, reducing probability of detection or, if the detection threshold remains low, increasing constant false alarm rate and false plots. Flight tests near wind farms have documented both effects [38, 39, 40, 41, 42, 43, 44, 45, 46].

Weather radar suffers many of the same effects of increased clutter, Doppler shift, and creation of shadow regions, but the operational impacts manifest differently. For weather radar, windfarm interaction results in inaccurate precipitation estimation, misidentification of thunderstorm features, and false tornadic vortex readings [49, 50, 51, 52, 53]. These effects directly impact the quality and reliability of meteorological data.

Radar-windfarm interaction has been investigated from many different perspectives, both at the radar and turbine. The outline above is intended to summarize current status and highlight key features, rather than provide a comprehensive analysis of radar-windfarm interaction. Nonetheless, it provides insight into areas in which particular solutions will have the most impact.

A number of radar upgrades or changes to radar procedure have been suggested to mitigate interaction with wind farms, however, each increases radar cost or operational complexity [54, 55, 56, 57, 58, 59, 60]. At the radar solutions include gap filling, track initiation inhibit, range azimuth gating, statistical techniques to reduce clutter, among others [21, 22, 23, 24]. In all likelihood, a combination of radar upgrades, procedural modifications, and low RCS turbine designs will be required to address all aspects of radar wind farm interaction [61, 62, 63, 64].

2.2.2 At-The-Turbine Solutions

At-the-turbine solutions fall into three approaches: shaping, applying radar absorbing material (RAM), or including active components to aid in radar identification and filtering [65]. Shaping applies primarily to the tower and nacelle regions, since blade shape controls aerodynamic performance and energy efficiency. Active component solutions alter blade Doppler response with a phase-switched screen, either by shifting Doppler reflections outside of the detectable spectrum, or by adding a high intensity Doppler response that can be used to identify wind turbines [66, 67, 68, 69, 70]. Both approaches require active switches or similar components which increase fabrication complexity and cost. Active components also have a higher failure rate than passive layers and increase the likelihood that RAM would have to be maintained in fielded wind turbines. Although active approaches show long-term promise, the technical benefit (Doppler spectrum control) was not considered substantial enough to investigate in this effort, given increased fabrication complexity, increased cost, and the viability of passive RAM solutions [71, 72, 73, 74, 75, 76].

Passive RAM solutions can be external, in which a coating is applied after construction, or integrated, in which construction is altered to include RAM while maintaining structural and aerodynamic performance. Initial studies indicated that a high performance absorber (wideband absorption over a wide range of incident angles) must be approximately 1-1.5 inches thick at S-band and 2-3 inches thick at L-band. Coating a blade with such

thicknesses would be extremely difficult, not to mention operationally impractical in terms of blade weight and shape; as a result, integrated RAM is critical to successful at-the-turbine solutions.

3. Development of Absorptive Treatment

Given the lack of agreement in the literature regarding absorber design processes, a significant modeling effort was performed in order to provide a foundational design process and obtain the best possible absorber performance. This chapter outlines four modeling tools: ADS® [77], HFSS® [78], CST MWS® [79], and Xpatch® [80]. HFSS and CST MWS, full-wave electromagnetic (EM) solvers capable of analyzing the RCS of complex structures, were used to develop unit-cell models for multilayer absorbers. ADS models were then developed to reduce time between design iterations and allow access to powerful optimization tools. HFSS models for large flat plates were created for comparison to measured structures.

As measurement of complete blades was outside the scope of this effort, Xpatch blade models will provide simulated data that can be compared to future measurements. Xpatch blade models incorporating absorber designs developed in ADS and HFSS into a complete wind-turbine blade will provide a comparison with existing blades, and give feedback regarding multipath and the effect of blade curvature on RCS. Table 1 summarizes the limitations and strengths of the various modeling tools, and Figure 6 illustrates the project design flow from tool to tool. The following sections discuss the capabilities of each modeling tool in order of their use in the process flow.

Table 1 Strengths and limitations of the EM design tools used in this effort.

Tools	ADS	HFSS & CST MWS	Xpatch
Strengths	• Extremely fast solve time • Optimization tools • Statistical/process tools	• No simplifying approximations	• Models extremely large structures
Limitations	• Assumes flat, infinite absorber	• Time-limited to small structures	• Physical optics approximations

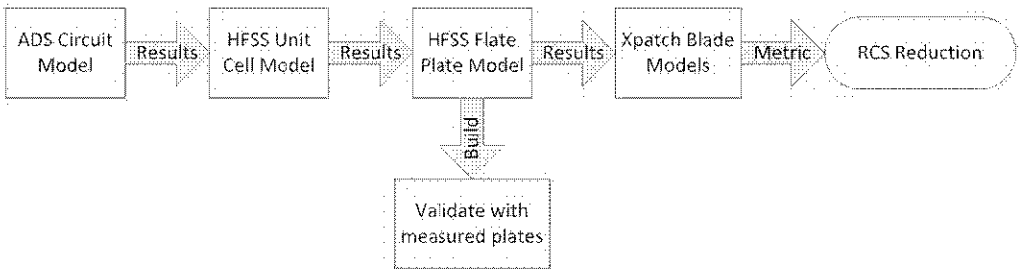

Figure 6 Process flow for blade integrated absorber design, including measurement of flat plates to prove model validity and full blade models to establish an RCS reduction metric.

3.1 ADS Models

ADS is an RF circuit simulator, and is commonly used to design RF circuits and systems. It provides access to a wealth of design equations that have been compiled from decades of research and development. Since ADS calculates circuit performance based on closed-form equations (rather than numerical solutions, as will be discussed in the following sections), it runs much quicker than HFSS or CST MWS. Numerical solvers such as HFSS and CST MWS can model almost any structure, whereas ADS is limited to those structures for which design equations have been derived. ADS also has access to a suite of powerful optimization and statistical analysis tools that are unavailable in numerical solvers at this time. These tools are critical to the design of a

high performance multilayer absorber with constrained design parameters and practical fabrication limitations. In order to leverage ADS' quick run time and powerful optimization techniques, the following assumptions must be made to simplify absorber design into a circuit model.

- The absorber is flat or curvature is small relative to a wavelength.
- The absorber is infinite in extent or very large relative to a wavelength.

Although these assumptions may seem unrealistic in light of the curvature and size of an actual blade, the following sections on numerical solvers will clarify how designs generated in ADS apply to an actual wind-turbine blade. Results from ADS circuit models have a firm physical foundation, and agreement with numerical solvers is excellent.

3.1.1 Transmission-Line Equivalent-Circuit Model

Figure 7 illustrates a multilayer absorber and the equivalent circuit model in ADS. Each absorber layer is modeled as an equivalent transmission line; the resistive layers are modeled as shunt resistors, and the metal backing terminates the absorber with a short circuit. For CAA, the shunt elements would have an equivalent capacitance or inductance (determined by CAA geometry) as well. For Dallenbach absorbers, the equivalent transmission line sections would be lossy. The model in Figure 7 assumes that the absorber is perfectly flat and infinite.

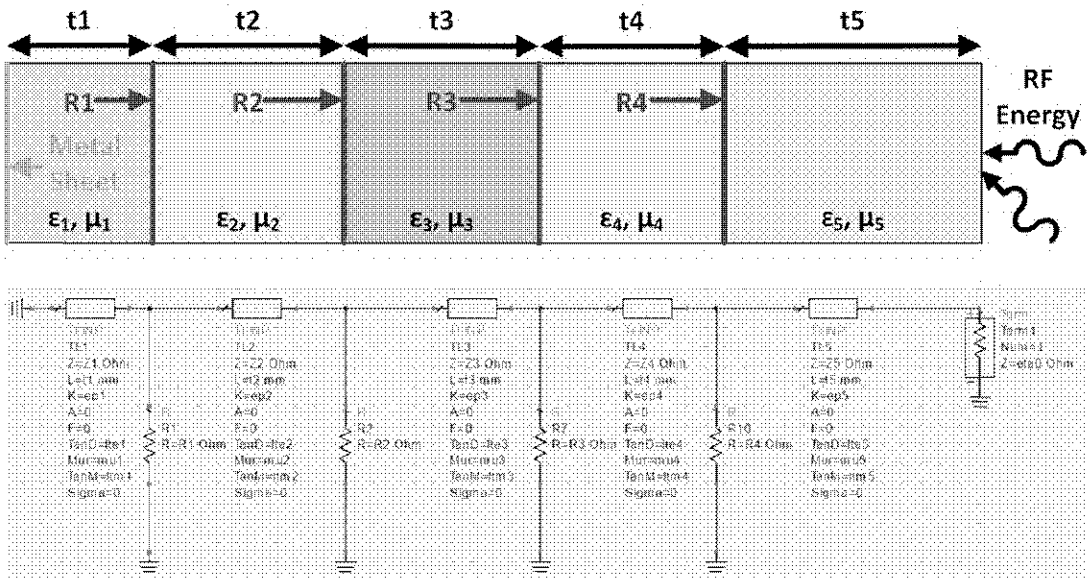

Figure 7 Multilayer Jaumann absorber (top) and equivalent ADS circuit model (bottom).

The bottom half of Figure 7 shows a circuit model for normal incidence, but incident RF energy can arrive at any angle, as indicated in the top half of the figure. Absorption over a range of oblique angles of incidence is an important metric of absorber performance, as the vast majority of RF energy does not arrive at normal incidence. Improving absorber performance over a range of angles of incidence typically increases thickness and weight.

An equivalent circuit model was derived to calculate absorber performance over a broad bandwidth at all angles of incidence. The derivation is based on theory from [81], which can be referenced for further detail. At normal incidence, the goal in Jaumann absorber design is to match the impedance of

the metal backing (short circuit), to that of free space ($\eta_0 = 377\Omega$). This is achieved with transmission lines whose properties are

$$Z_x = \sqrt{\varepsilon_x / \mu_x}$$
$$t_x = \frac{L_x \sqrt{\varepsilon_x \mu_x}}{\lambda}, \tag{2.1}$$

where λ is wavelength, ε is permittivity, μ is permeability, L_x is the physical length for each layer, t_x is the electrical length for each layer, Z_x is the characteristic impedance, and x is the layer number. Shunt resistance values are determined by the sheet resistance, in ohm/square, of the infinite resistive sheets between layers.

For oblique incidence, transmission line impedances vary according to

$$Z_{x,TE} = \cos\theta_x \sqrt{\varepsilon_x / \mu_x}$$
$$Z_{x,TM} = \frac{\sqrt{\varepsilon_x / \mu_x}}{\cos\theta_x}$$
$$t_{x,TE} = \frac{L_x \cos\theta_x \sqrt{\varepsilon_x \mu_x}}{\lambda} \tag{2.2}$$
$$t_{x,TM} = \frac{L_x \sqrt{\varepsilon_x \mu_x}}{\lambda \cos\theta_x},$$

where TE and TM refer to the electric field polarization (also known as parallel and perpendicular, according to whether the E-field is parallel or perpendicular to the page, reference Figure 7), and θ_x is the incident angle in each layer according to Snell's law. Shunt resistance values remain the same as for normal incidence. The impedance of free space Z_0 varies according to

$$Z_{0,TE} = (377\Omega)\cos\theta_0$$
$$Z_{0,TM} = \frac{(377\Omega)}{\cos\theta_0} \tag{2.3}$$

for oblique incident angles. With the electrical properties of transmission lines and resistive sheets characterized over frequency and incident angle, circuit models in ADS were used to design broadband multilayer absorbers with high absorption over a wide range of incident angles.

3.1.2 Comparison with Full-Wave Models

ADS results were compared with full-wave solutions from HFSS unit-cell models to validate circuit model accuracy. Figure 8 shows perfect agreement between exact solutions from ADS and numerical solutions from HFSS over a wide range of incident angles. A single ADS circuit model takes less than 1 second to run, whereas a comparable unit-cell model in HFSS takes 10-15 minutes. This corresponds to a 600-1000X reduction in design time. When each design solves on the order of a second, optimization algorithms can vary

design parameters (layer thicknesses, material parameters, resistor values) over thousands of iterations to determine a best solution. In addition, Monte Carlo analysis of several thousand solves allows the designer to identify critical process tolerances and compensate for fabrication issues during the design phase. Given its powerful optimization and statistical tools, ADS was used to optimize absorber designs and account for statistical process tolerances (e.g. layer thickness variation). HFSS and Xpatch will be used in future phases to validate absorber performance for measured plates and treated wind-turbine blades.

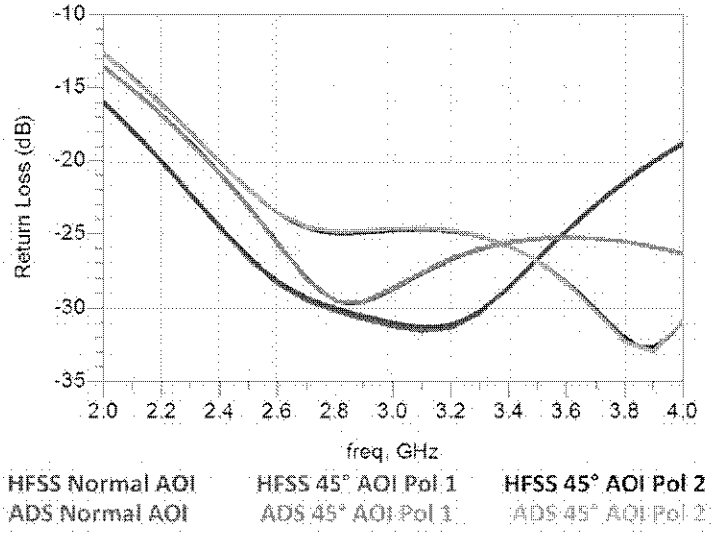

Figure 8 *Agreement between ADS circuit models and HFSS unit-cell models at normal and oblique angles of incidence (AIO) over S-band.*

3.2 Full-Wave Models: HFSS & CST MWS

Although circuit models in ADS enable extremely quick-turn design and the use of powerful optimization and statistical analysis tools, the assumption of flat, infinite plate absorbers does not apply to measured plates or wind-turbine blades. Numerical solvers are used to transition from ADS to measured data and models of a treated blade. HFSS and CST MWS were used to model multiple aspects of RF absorbers, so a brief description of tool capabilities and various model types will clarify simplifying approximations and model correspondence to reality. HFSS uses the finite element method (FEM), and CST uses the finite difference time domain (FDTD) method. Both FEM and FDTD are numerical solutions of Maxwell's Equations; as such, both HFSS and CST model the exact physics that occur in reality. As is the case with all numerical solvers, the agreement between HFSS or CST and the true solution depends on convergence criteria, which directly impact simulation time. In addition to convergence criteria, inaccurate dimensions or material properties can cause modeled results to disagree with reality; nonetheless, a well-dimensioned model with accurate material properties and strong convergence should predict reality with a high degree of accuracy.

3.2.1 Floquet Unit-Cell Models

Although full-wave solvers provide the greatest agreement with reality, models larger than a few wavelengths require significant computation time. Structures larger than 10 - 20 wavelengths become time prohibitive altogether. A 60-meter wind-turbine blade is 400 wavelengths long at S-band, far too large to be completely modeled in HFSS or CST MWS. For large, flat, periodic structures, unit-cell models based on Floquet modes can reduce an electrically large problem to a much smaller size. Structures that are several dozen or hundred wavelengths long can often be modeled in a unit-cell smaller than a single wavelength. Figure 9 illustrates this concept. Small structures with a small radius of curvature and non-periodic features cannot be modeled with a unit-cell, whereas infinitely large, periodic plates with no curvature will perform exactly as predicted by unit-cell models. In actuality, most structures lie somewhere between the two extremes, and agreement between

unit-cell models and the actual structure depends on the degree of curvature, structure size, and periodicity. Wind-turbine blades are very large, and the curvature in most regions of the blade is large with respect to a wavelength, making blades a good candidate for the unit-cell approach. HFSS unit-cell models provide an initial validation of ADS circuit models, as both assume an infinitely large, flat absorber.

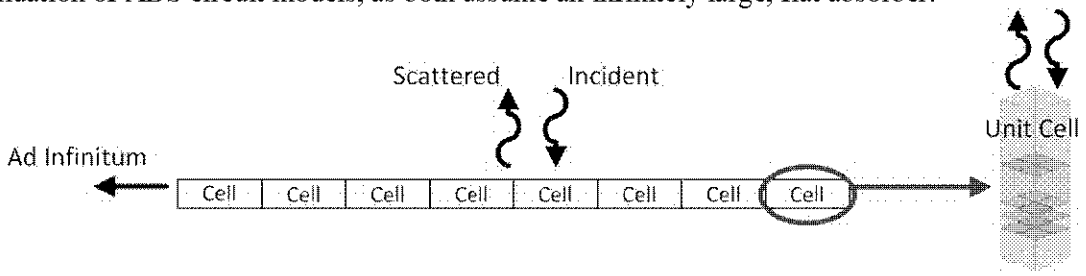

Figure 9 Reduction of a large structure to small unit-cells.

3.2.2 Large Plate RCS Models

Since unit-cell models assume an infinitely large plate, the finite plates that are actually built and tested will differ from unit-cell predictions. Plate models were used to characterize the effects of finite size on measured absorber performance. Unit-cell models allow quick-turn absorber design, and large plate models validate that the edge effects, due to the finite size, do not significantly impact absorber measurements. Figure 10 shows an example of agreement between unit-cell and plate models. Agreement is near perfect at normal incidence and degrades slightly at 45° oblique incidence due to edge effects. As frequency decreases, the plate looks smaller relative to a wavelength, so plate size must increase to minimize edge effects. Perfect agreement should not be expected between unit-cell and plate models, as extremely large plates are difficult to measure. Since flat plate absorbers were actually measured, large plate RCS models provide the best comparison with measured data. Figure 11 outlines the process flow from initial design to final measurement.

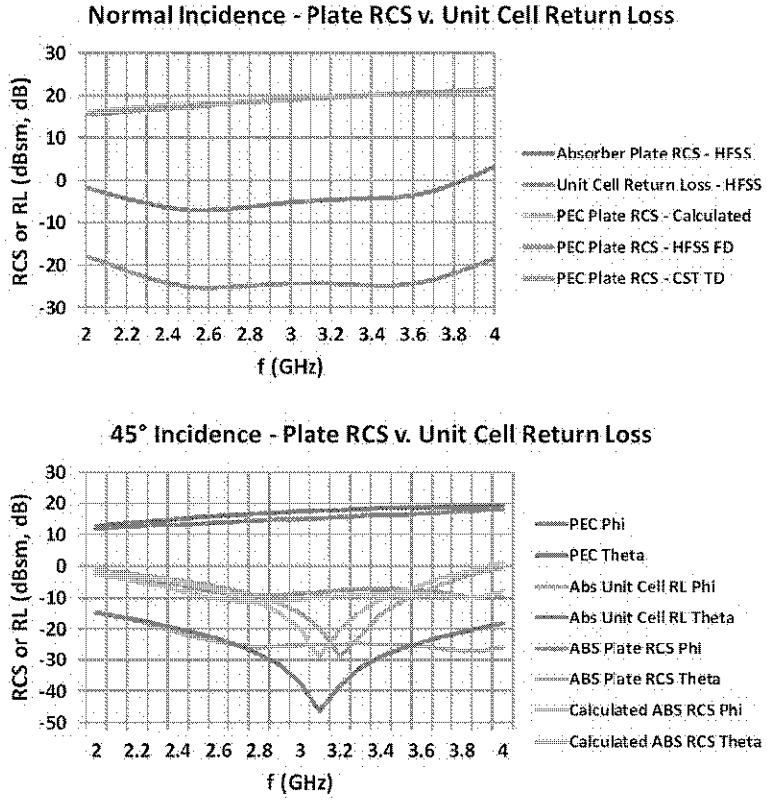

Figure 10 Agreement between HFSS unit-cell and large plate RCS models (S-band, 0.5 meter x 0.5 meter plate).

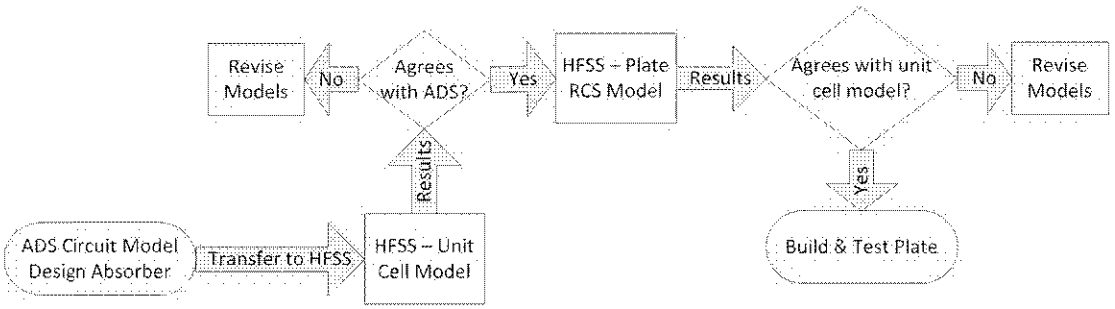

Figure 11 Process flow from absorber modeling to flat plate measurements. Decision points verify that the assumptions made in each design stage are accurate.

3.3 Xpatch Models

Figure 12 illustrates how material measurements enabled models of wind-turbine blades, both standard and with integrated RAM, to determine an RCS reduction metric. Various blade materials were measured to determine electrical properties, which were then imported into Xpatch to model a realistic, untreated wind-turbine blade. Measurement of blade materials will be discussed in greater detail in *Material Development and Integration*. Electrical properties were used in ADS to design an integrated absorber. In future phases, integrated absorber designs from ADS will be imported into Xpatch to create a treated blade. Simulation of treated and untreated blades allows a determination of radar signature reduction.

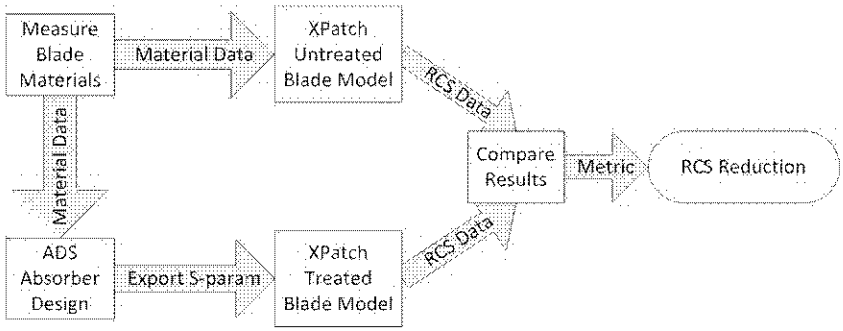

Figure 12 Process flow from material measurement to modeling of treated and untreated blades in Xpatch.

3.4 Model Validation

3.4.1 Purpose - Model Validation

To gain confidence in the modeling approach, the first measurement phase used commercially-available RF printed-circuit-board (PCB) based absorbers. Once the models have been validated with well-controlled materials and fabrication, uncertainties in the final treatment designs can be limited to material formulation and blade-fabrication processes, rather than EM modeling techniques.

Although the initial goal was to verify models using multilayer S-band absorbers, high-performance S-band absorbers must be approximately one-inch thick, and RF circuit fabricators cannot laminate boards that thick. Furthermore, high-performance multilayer absorber designs require tight control over each individual board thickness resulting in custom board thicknesses that increase material costs. As discussed in *Large Plate RCS Models*, board sizes must increase with decreasing frequency to minimize edge effects, further increasing material costs. These considerations limited the first measurement phase to three absorber designs, two single layer and one multilayer, operating within C-, X-, and Ku-band. The physics governing EM design apply at L- and S-band just as well as at C-, X-, and Ku-band. Validating models at higher frequencies provides the same

level of confidence in the modeling approach while aligning fabrication processes and dimensions within common board shop capabilities.

The boards were designed using Rogers Corporation PCB materials clad with Ohmegaply resistive material from Ohmega Technologies, Inc., although other vendors produce similar products. The sheet resistivity values available from Ohmega are limited to 25, 50, 100, and 250 Ω/square; consequently, discrete etched resistors were used to achieve effective sheet resistances with 100 Ω/square resistive material, since values ranging continuously from 100-1000 Ω/square were needed (e.g. 377, 600, and 950 Ω/square) [82]. This design approach is illustrated in Figure 14. HFSS models of designed resistor geometries account for all variations due to discrete resistors. Boards will be etched and bonded by a RF board shop specializing in low quantity, high performance prototypes. Figure 13 illustrates the three model-validation designs.

3.4.2 Fabrication Process

The first-measurement-phase boards are currently being fabricated. Details of the fabrication process and a comparison of modeled and measured results will be provided in Part 2 of this report.

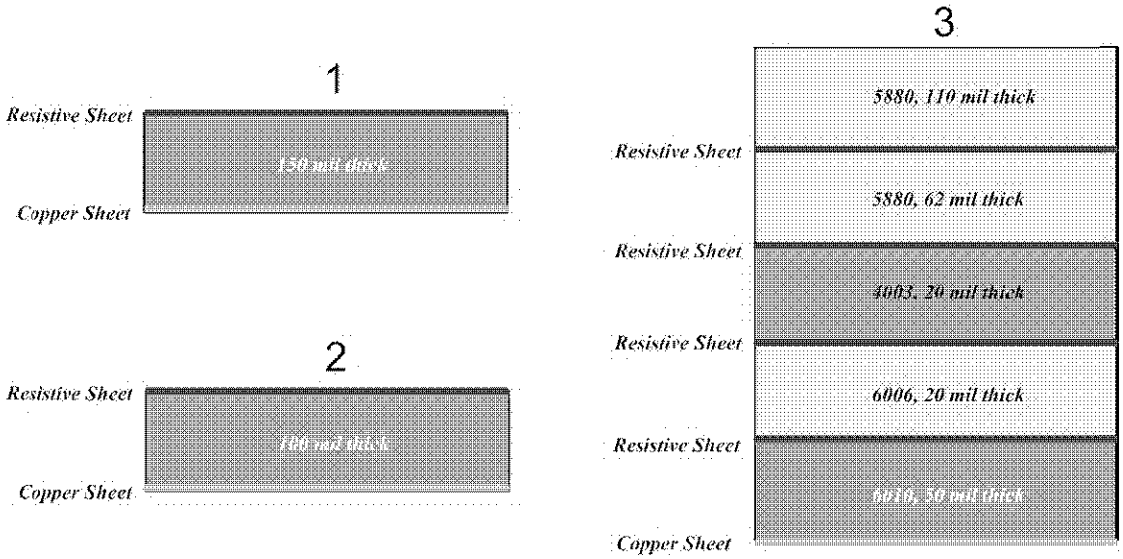

Figure 13 Cross-section of the three measurement validation designs.

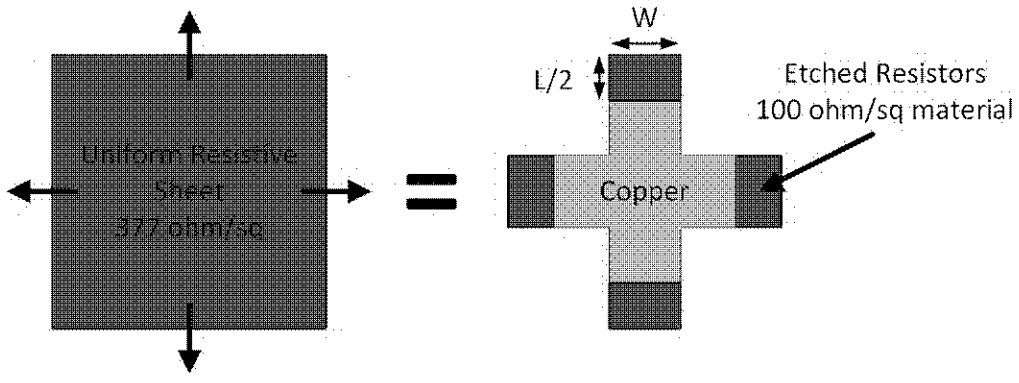

Figure 14 Equivalence of a uniform resistive sheet and an etched resistor grid network.

4. Material Development and Integration

The realization of electrically-useful materials imposes a practical limit to absorber performance. The EM engineer can design ultra-thin, wideband absorbers with high-loss magnetic materials, but practical implementation depends on the existence of such materials and on other properties such as density and cost. Material development efforts include both characterizing existing blade materials and developing novel materials with desirable electrical properties for low-impact integration into blades. Materials were developed to be incorporated in a vacuum-assisted resin-transfer molding (VARTM) process, as VARTM is commonly used in blade construction and SNL has existing VARTM fabrication capabilities.

Materials currently used in wind-turbine blades have been developed and optimized primarily based on mechanical performance, reliability, and materials and manufacturing cost. In this study, we aimed to design optimal materials that both enable exceptional radar performance as well as facile integration into conventional VARTM turbine-blade manufacturing processes. The motivation is to retain established mechanical properties and manufacturing methods, while allowing significant reduction of composite-blade RCS. *Design of Blade-Representative Test Samples* discusses how these new materials designs enabled optimization of Jaumann absorber designs, which consist of multiple dielectric layers, each backed with a layer of some zero to high resistivity value, as shown in Figure 15. The two main areas of investigation have been (i) investigating resistive layers which may be integrated and tested for RCS properties within manufacturable wind-turbine composites, and (ii) design of new, manufacturable dielectric materials (electrical permittivity $\varepsilon \neq 1$) and magnetodielectric materials (magnetic permeability $\mu \neq 1$).

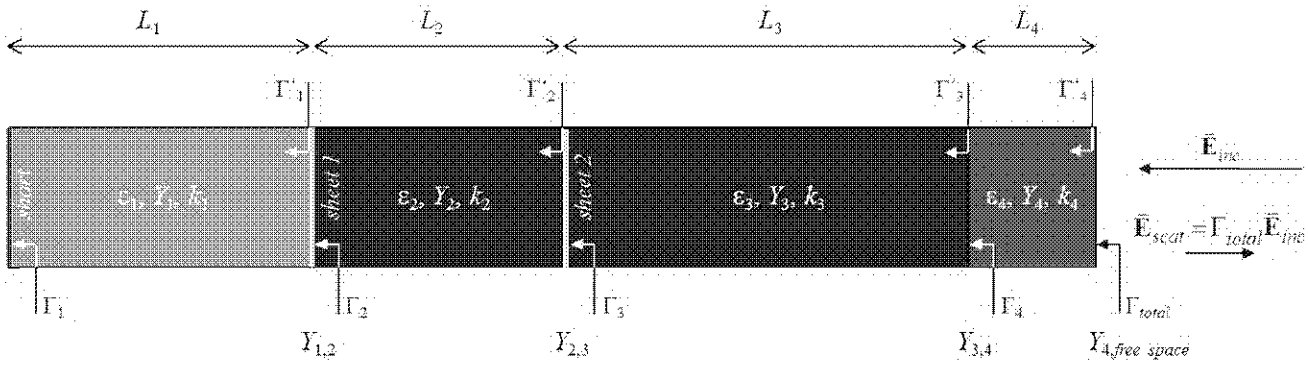

Figure 15 Structure of a 4-layer Jaumann absorber, based on magnetodielectric layers each of electric permittivity ε_i, magnetic permeability μ_i and thickness L_i, with resistive sheets between each layer, and a highly conductive back plane which creates an electrical short circuit condition.

There are two primary structural components in a typical blade, spar caps and foam- or balsa-sandwich panels as shown in Figure 16. These structures are comprised of four components, whose permittivity ε' is noted below; all regions are nonmagnetic, high-resistance dielectrics with $\varepsilon'' < 0.02$, $\mu' = 1$ and $\mu'' < 0.02$:

- Uniaxial fiberglass infiltrated with resin, $\varepsilon' \sim 4.3\text{-}4.5$
- Biaxial fiberglass infiltrated with resin, $\varepsilon' \sim 4\text{-}4.2$
- Closed cell polyurethane foam, $\varepsilon' \sim 1.1$
- Balsa wood, $\varepsilon' \sim 1.2$

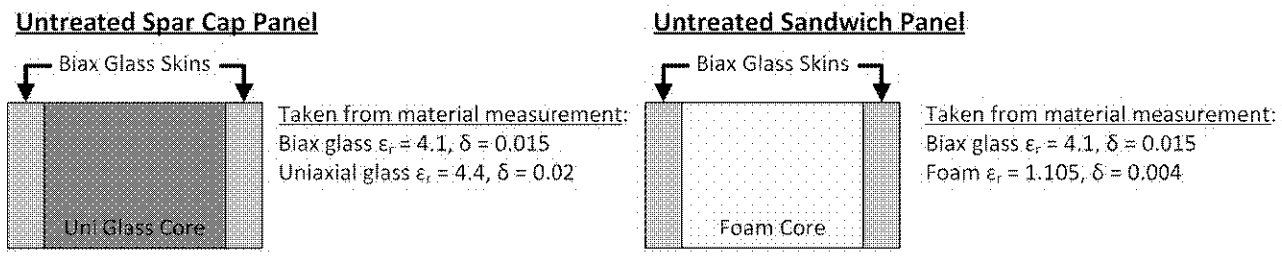

Figure 16 Blade structure and typical cross section of turbine blade panel and spar-cap regions.

In this report, we have (i) characterized standard composite blade electrical properties, and (ii) considered means of designing and integrating designed conductivity layers and designed dielectric composites into standard blade manufacturing methods.

4.1 Wind Turbine Electrical Properties

Numerous wind-turbine-blade materials were measured in a GR900 coaxial line in order to characterize electrical properties for use in integrated absorber design. Previous studies have validated the use of GR900 samples to determine material properties [83], and a plethora of algorithms exist that extract electrical properties from S-parameter data [84, 85, 86, 87]. Agilent 85071 material extraction software, which implements many of these algorithms, was used with an Agilent E8363B Programmable Network Analyzer (PNA) to determine complex permittivity and permeability. Figure 17 illustrates the GR900 coaxial fixture and several samples. Material samples shown include fiberglass composite, foam- and balsa-sandwich samples, fiberglass with embedded resistive material, carbon composite, and various commercial board materials.

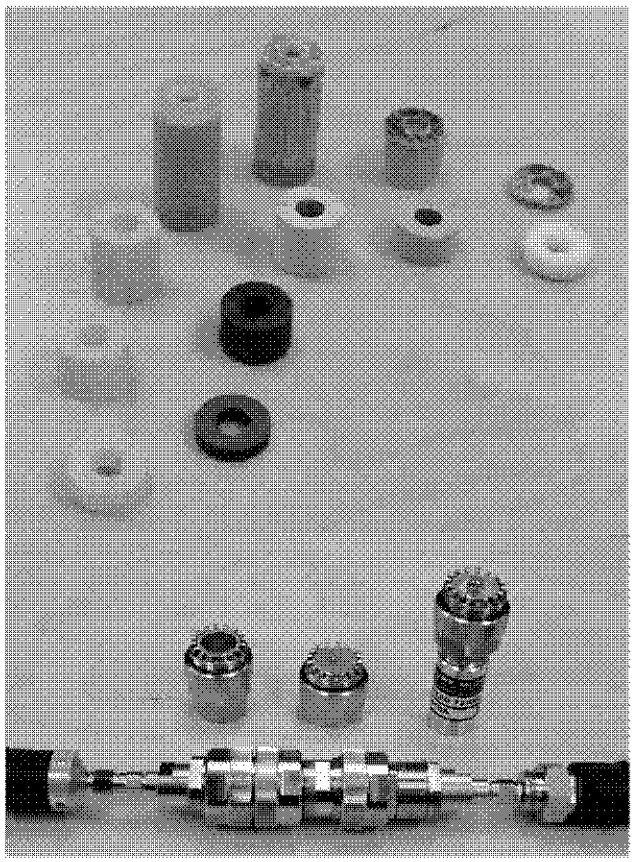

Figure 17 GR900 material samples (top) and coaxial measurement fixture with calibration standards (bottom).

To validate the calibration technique and material extraction software, several samples of common board materials were measured and compared against vendor data. Table 2 lists all board materials measured and summarizes the electrical properties for each. All measurements agree with vendor data to within ± 5%, with the exception of Rogers TMM10i (ε_r = 8.6-9 versus 9.8 claimed) and Arlon DiClad 522 (ε_r = 2.78 versus 2.35-2.65 claimed). Measured loss tangents are typically higher than vendor claims, likely because of copper losses through the coaxial line. Disagreement between measured material properties and vendor data can be attributed to imperfect calibration, radial gaps between the sample and sample holder, sample positioning errors, and material aging. Radial gaps introduce greater error for high permittivity samples. All calibration and standard blade materials were measured with position invariant iterative techniques, which assume non-magnetic materials.

Table 2 Measured material properties of common RF PCB materials compared to vendor data.

Material	Measured ε'	Measured ε"/ε'	Expected ε'	Expected ε"/ε'
Rohacell	1.008	0.005-0.015	1.05-1.1	0.002-0.005
Teflon	2	0.0015	2	0.0015
Rogers 5880	2.2-2.26	0-0.005	2.2	0.0009
Cstock .0005	2.43-2.48	0.003	2.54	0.0005
Arlon DiClad 522	2.78	0.002-0.003	2.35-2.65	0.001
Rogers TMM3	3.25-3.29	0.001-0.002	3.27	0.002
Rogers TMM4	4.49-4.51	0.001-0.002	4.5	0.002
Rogers TMM10i	8.6-9	0-0.02	9.8	0.002

With the calibration and material extraction approach validated by samples of common board materials, several composite and core materials commonly used in blades were measured. Table 3 lists all blade materials measured and summarizes the electrical properties for each. Composite materials were measured twice, with fibers running both parallel and perpendicular to the axis of the coaxial line, to determine whether permittivity varied with electric field polarization. Composite material properties did not change significantly with polarization. Samples of blade materials were both constructed in-house and machined from blade materials supplied by a commercial blade manufacturer. The electrical properties of materials prepared in-house correspond well with commercial material properties. Values from the table were used as inputs for integrated absorber designs.

Table 3 Summary of GR900 measurements of blade materials.

Material	Measured ε' Range	Measured ε"/ ε' Range	Nominal ε'	Nominal ε"/ ε'
Resin	2.8 - 2.9	0.025 - 0.035	2.85	0.03
Biax Glass 2400	3.95 - 4.25	0.015 - 0.025	4.1	0.02
Uniaxial Glass 5500	4.3 - 4.7	0.01 - 0.02	4.5	0.02
Quadaxial Glass SXQ	4.1 - 4.5	0.01 - 0.03	4.3	0.02
Commercial Glass	4.1 - 4.5	0.015 - 0.035	4.3	0.02
Commercial Foam	1.11 - 1.12	0.008 - 0.014	1.11	0.01
Urethane Foam	1.1 1.2	0 - 0.006	1.105	0.004
Balsa Wood	1.2 - 1.3	0.015 - 0.02	1.25	0.015

The material properties shown in Table 3, along with custom materials and resistive sheet properties discussed below, were fed into ADS to design integrated absorbers. Measurement variations were accounted for in the

design process with statistical simulation tools in ADS, as this was determined to be a more robust and lower effort approach than trying to improve measurement precision through better calibration or sample machining.

Detailed material measurement data clarifies several measurement considerations. Data in Figure 18 through Figure 27 provides S-parameters for several calibration standards and the material sample holder before and after measurement. As can be seen from the figures, the calibration quality declines over the course of the measurements. This degradation can be attributed to cable movements, PNA drift, residual material contaminating connectors, and a lack of repeatability in the coaxial fixture as samples are removed and replaced. The post-measurement S-parameters of the sample holder indicate a significantly increased loss from 3 - 3.75 GHz due to degradation over the measurement interval; this results in artificially high loss-tangent measurements in this frequency range. This measurement error can be corrected manually by taking either the 2 GHz or 4 GHz loss-tangent value (which are approximately the same in most cases) and applying it over all of S-band. Measurement of calibration standards before and after measurement did not indicate any other significant errors.

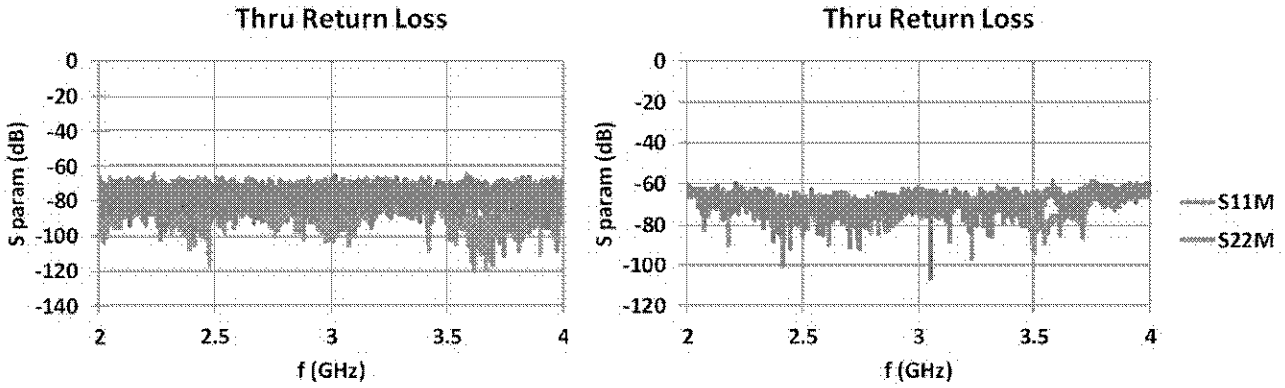

Figure 18 Return loss of the thru before measurement (left) and after measurement (right).

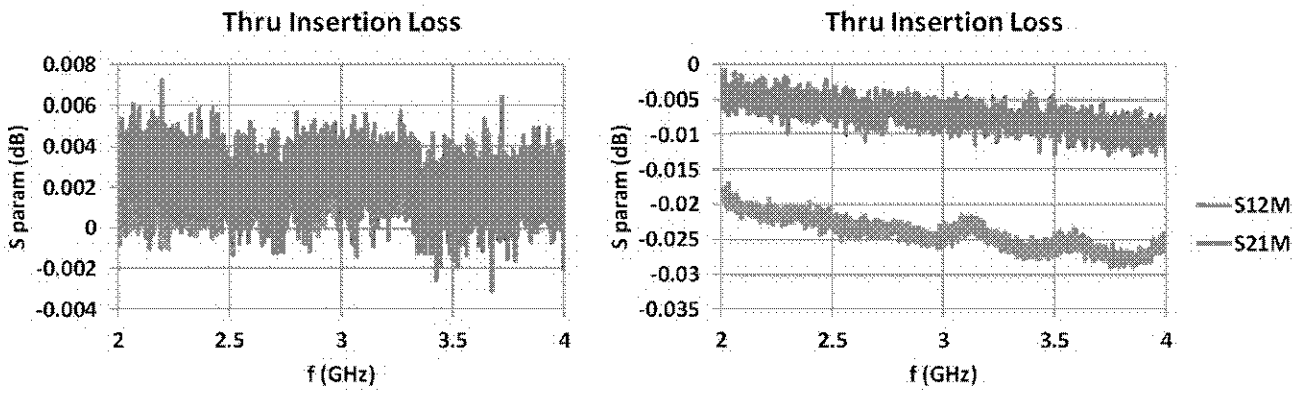

Figure 19 Insertion loss of the thru before measurement (left) and after measurement (right).

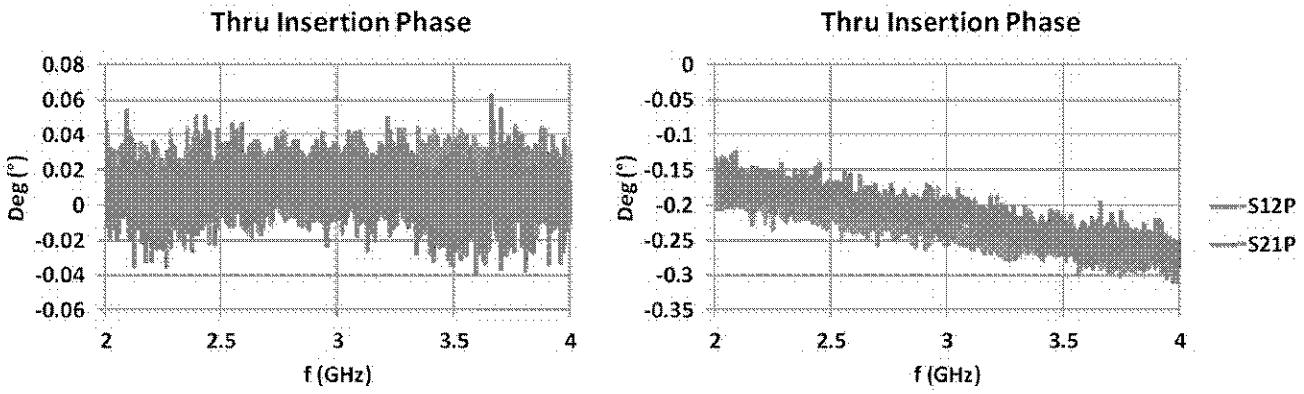

Figure 20 Insertion phase of the thru before measurement (left) and after measurement (right).

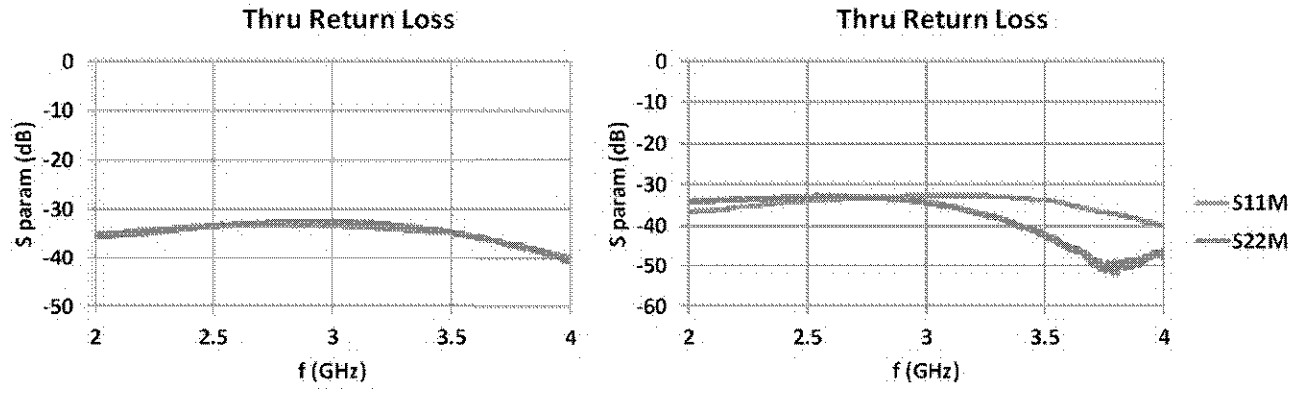

Figure 21 Return loss of the sample holder before measurement (left) and after measurement (right).

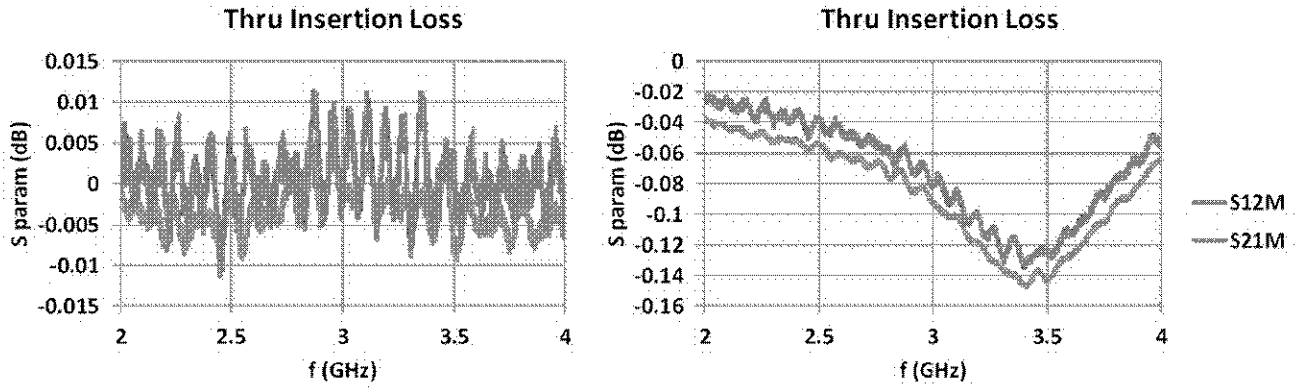

Figure 22 Insertion loss of the sample holder before measurement (left) and after measurement (right).

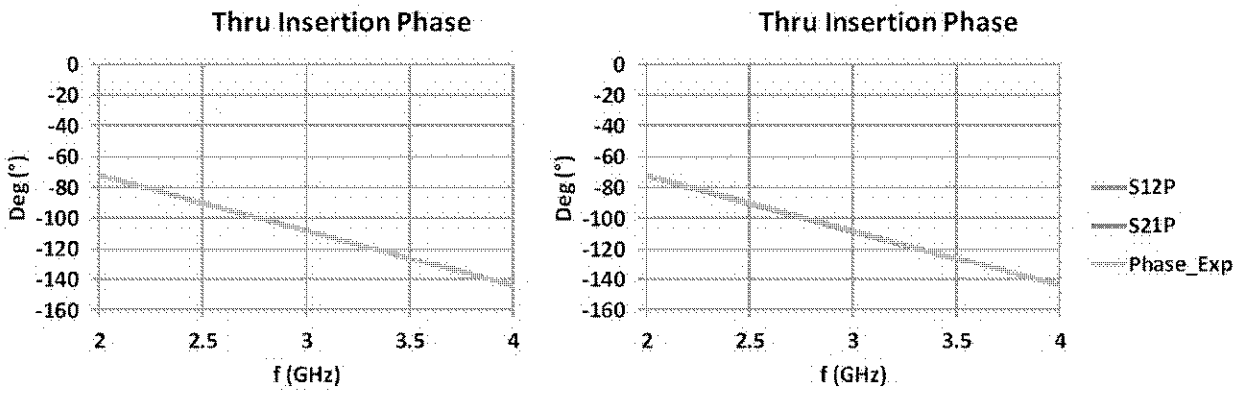

Figure 23 *Insertion phase of the sample holder before measurement (left) and after measurement (right), compared to expected phase delay for a 30 mm coaxial air-line.*

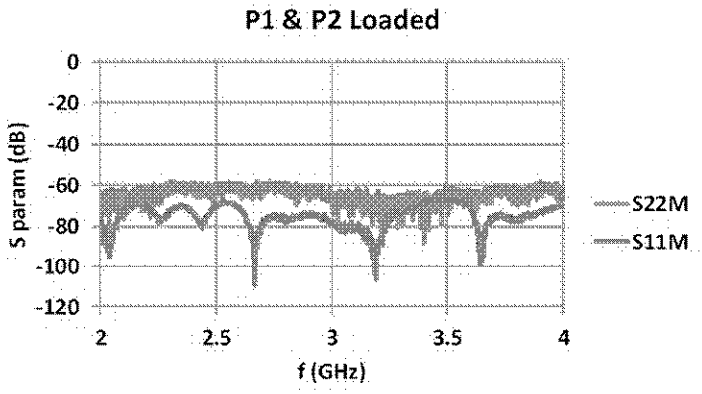

Figure 24 *Return loss after measurement of port 1 and port 2 with load standard connected.*

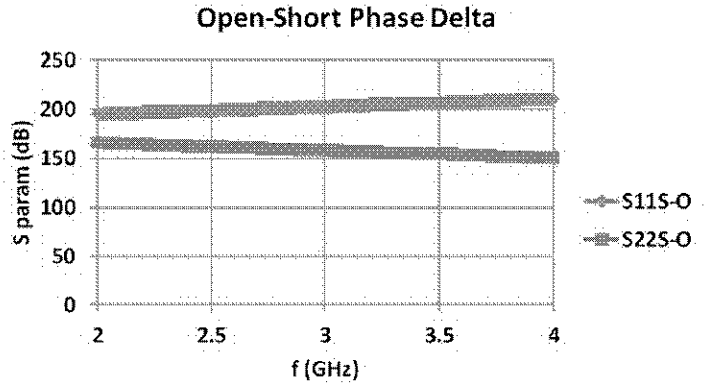

Figure 25 *Phase difference after measurement between open and short standards for port 1 and port 2.*

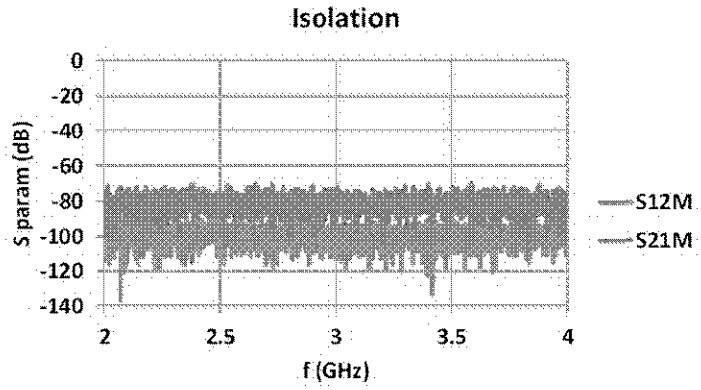

Figure 26 Isolation between ports 1 and 2 after measurement, with short connected to port 1 and open connected to port 2.

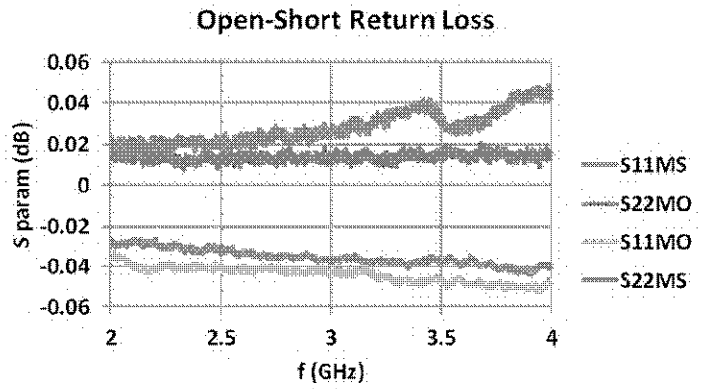

Figure 27 Return loss after measurement of open and short standards connected to ports 1 and 2.

Figure 29 through Figure 36 contain extracted material data for common board materials. The increased loss tangent due to calibration drift over the measurement interval can be seen in many of the measurements, but the values at the band edges agree well with one another. Even with calibration drift, almost all materials agree with vendor's dielectric-constant claims within ± 5%. Loss tangents are consistently high compared to vendor's claims, likely due to sample holder losses. The sample holder was inserted after calibration, preventing correction for sample holder losses. The materials were measured in the following order:

- Cstock .0005
- Rogers TMM10i, 12.7 mm and 5.1 mm
- Arlon Diclad 522, 6.2 mm
- Rogers TMM4, 3.16 mm
- Rogers TMM3, 7.6 mm
- Rogers 5880, 3.2 mm
- Resin, 15, 10, and 5 mm
- Urethane Foam, 15, 10, and 5 mm
- Vectorply 2400, biaxial, perpendicular and parallel fiber orientations, 15, 10, and 5 mm
- Vectorply 5500, uniaxial, perpendicular and parallel fiber orientations, 15, 10, and 5 mm
- SXQ Glass, quadaxial, perpendicular and parallel fiber orientations, 15, 10, and 5 mm
- Teflon, 22.3 mm

- Rogers 5880, 3.15 mm
- TPI blade, Glass, 6.55, 4.85, and 2.02 mm
- TPI blade, foam, 7.2 mm

The measurement progression reveals the likely cause of measurement error. The error did not increase constantly with time, as several materials (Teflon, 5880, TMM3, TMM4) that were measured at the middle or end of the measurement interval agree extremely well with vendor's claims, while others measured at the beginning do not agree well with vendor's claims. This indicates that errors are due primarily to lack of repeatability in the coaxial fixture, as opposed to PNA and cable drift with time.

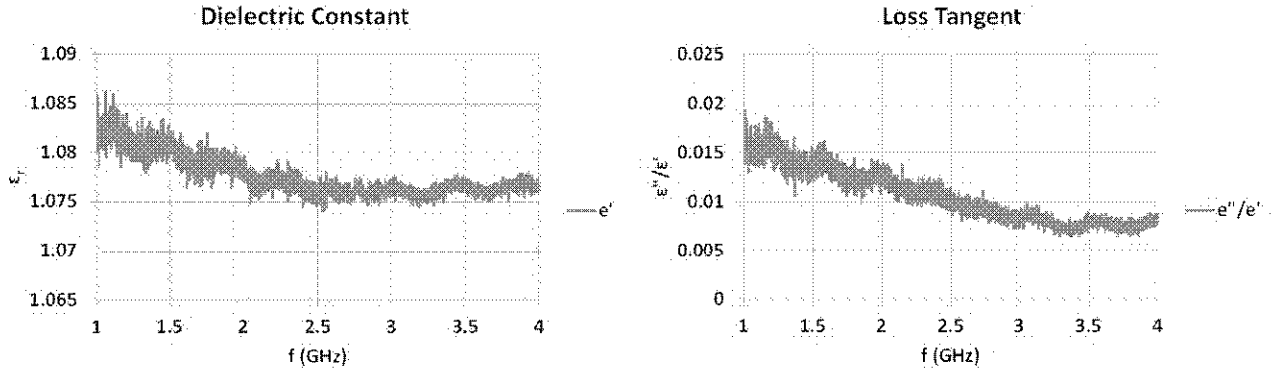

Figure 28 Measured permittivity and loss tangent of Rohacell sample, 1 cm thick. Expected permittivity is 1.05-1.1, loss tangent 0.002-0.05.

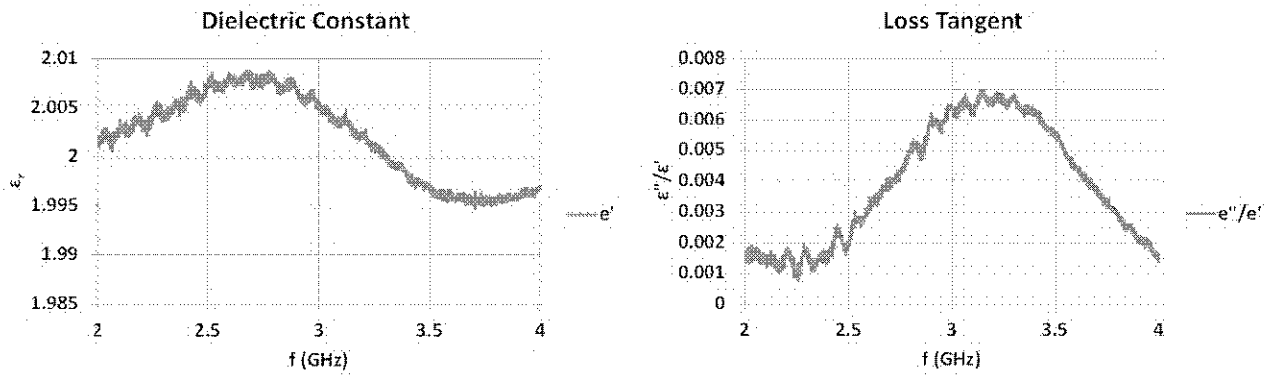

Figure 29 Measured permittivity and loss tangent of teflon sample, 22.3 mm thick. Expected permittivity is 2, loss tangent 0.0015.

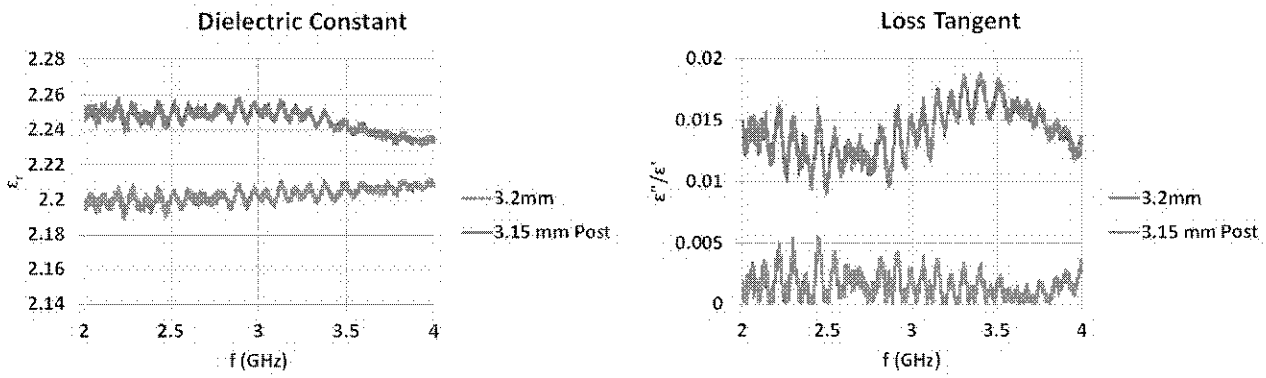

Figure 30 *Measured permittivity and loss tangent of Rogers 5880 samples, before and after measurement. Note the increased error after the measurement interval. Vendor claims permittivity of 2.2, loss tangent of 0.0009.*

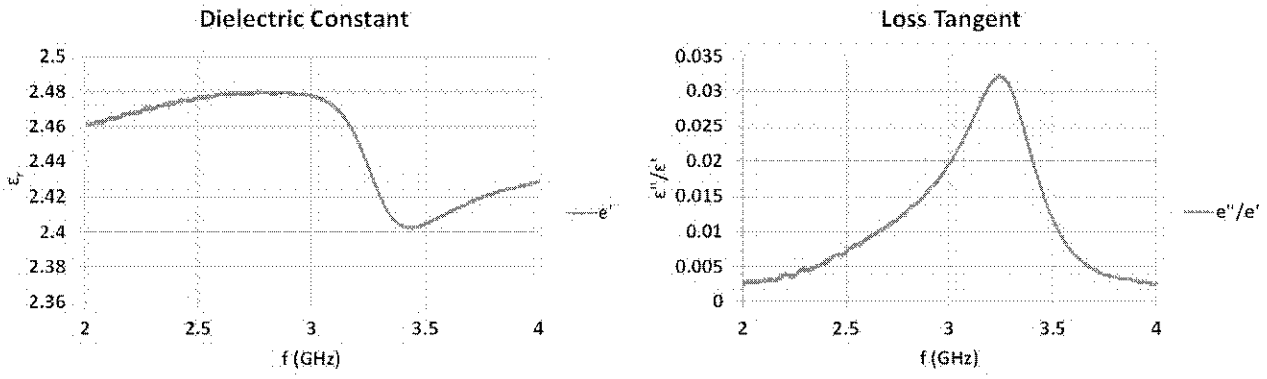

Figure 31 *Measured permittivity and loss tangent of Cuming Cstock .0005 sample. Vendor claims permittivity of 2.54, loss tangent of 0.0005.*

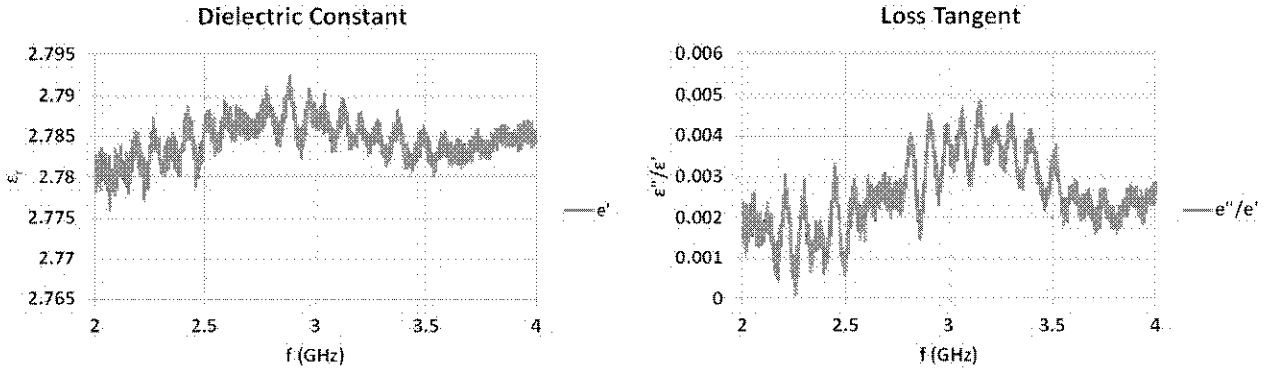

Figure 32 *Measured permittivity and loss tangent of Arlon DiCladd 522 sample. Vendor claims permittivity of 2.35-2.65, loss tangent of 0.001.*

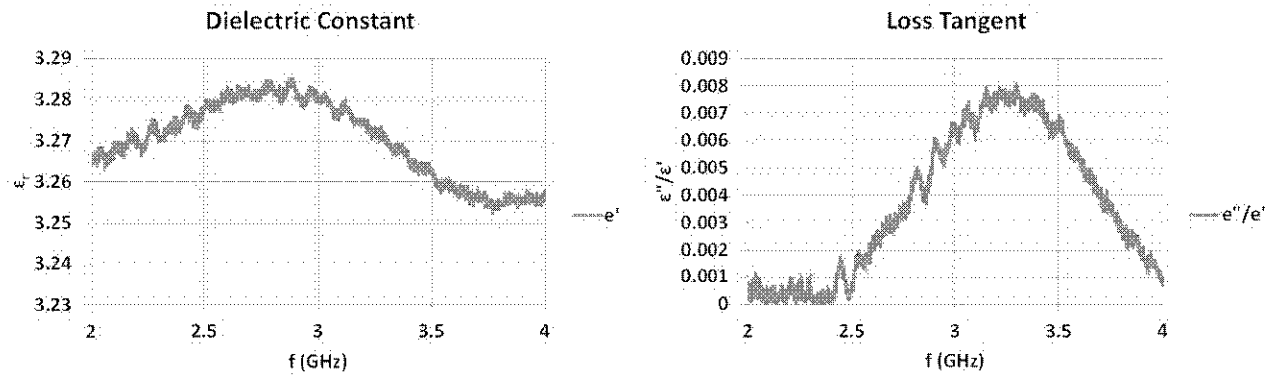

Figure 33 *Measured permittivity and loss tangent of Rogers TMM3 sample. Vendor claims permittivity of 3.27, loss tangent of 0.002.*

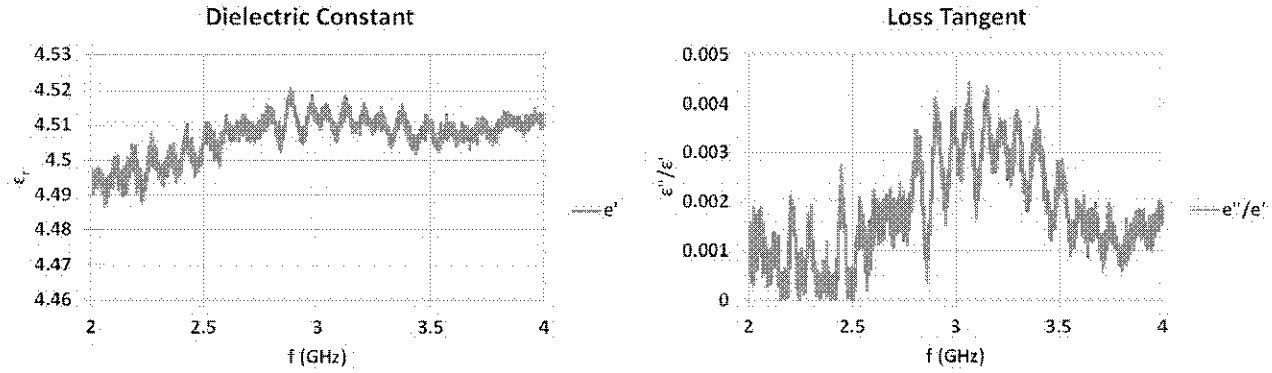

Figure 34 *Measured permittivity and loss tangent of Rogers TMM4 sample. Vendor claims permittivity of 4.5, loss tangent of 0.002.*

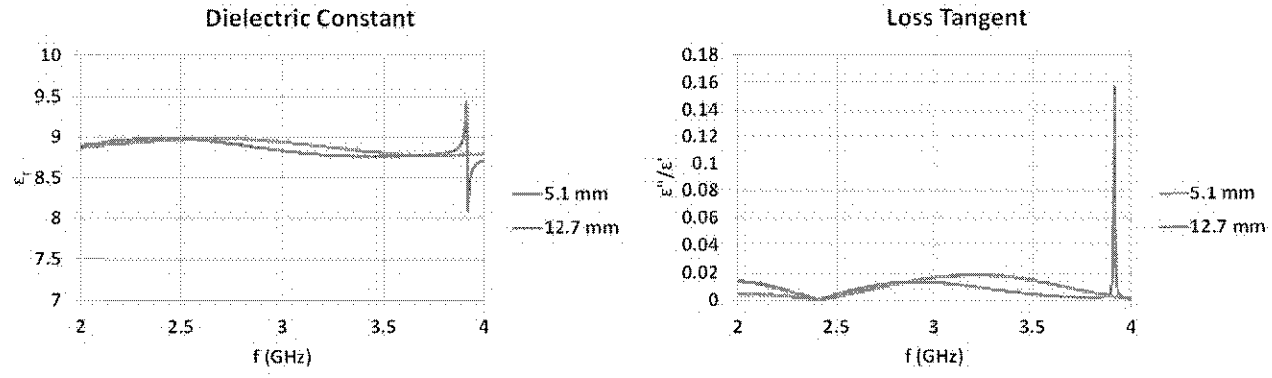

Figure 35 *Measured permittivity and loss tangent of Rogers TMM10i sample. Vendor claims permittivity of 9.8, loss tangent of 0.002. The spike near 3.9 GHz is due to the sample being a resonant half-wavelength. Disagreement with vendor claims could be due to material mislabeling (as TMM10 has permittivity closer to 9).*

Figure 36 through Figure 38 contain extracted material data for common wind-turbine blade materials. Samples of several thicknesses were taken from various locations across a reference panel to determine the extent of dielectric-constant variation across the plate. Measurements indicate that the measurement precision is significantly less than the sample-to-sample variation. This is an important consideration, as the sample-to-sample variation determines the process tolerances for integrated absorbers and thus the performance

degradation due to fabrication variations. *Absorber Integration into Turbine-Blade Fabrication* provides detailed information on fabrication variations. Samples were both prepared in-house using VARTM processes and machined from a commercial blade section provided by commercial blade manufacturer. Samples prepared in-house compare favorably with commercial materials.

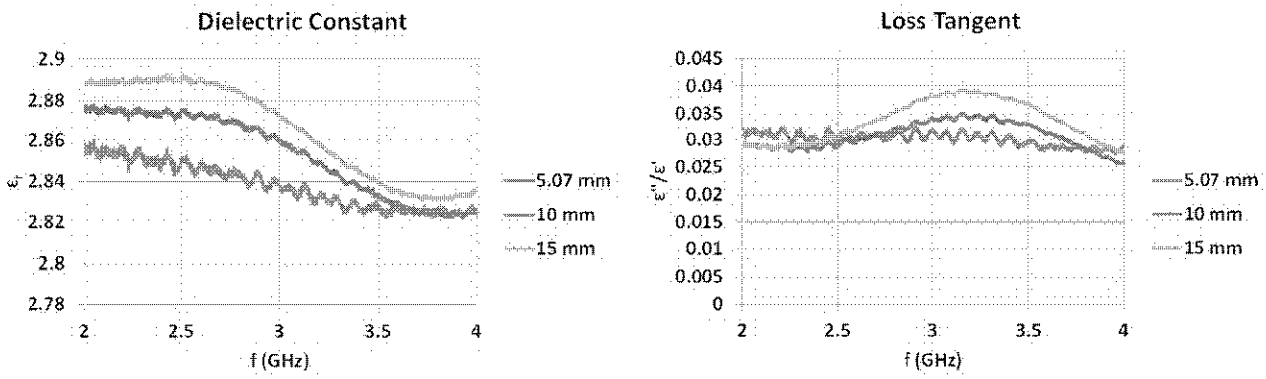

Figure 36 Measured permittivity and loss tangent of Hexion Epikote resin samples, no glass included. Sample to sample variation indicates permittivity ranges from 2.8-2.9, loss tangent ranges from 0.03-0.04.

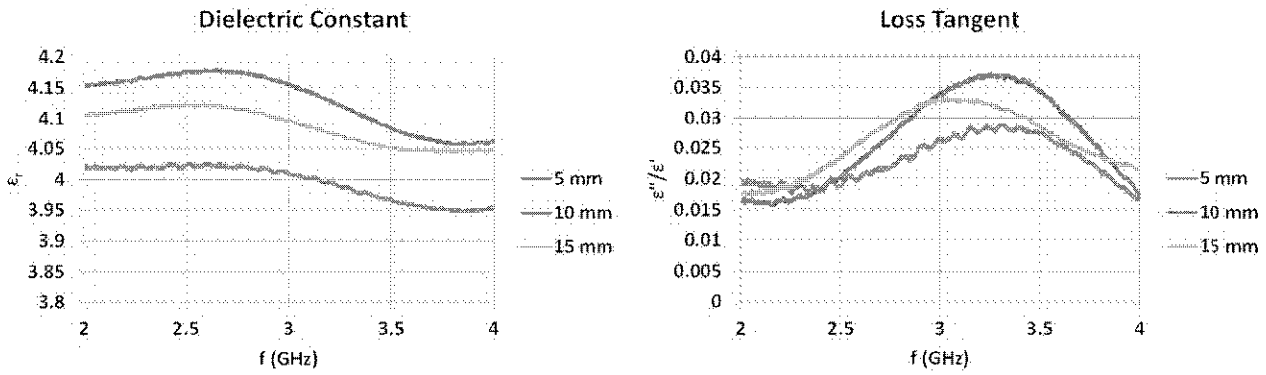

Figure 37 Measured permittivity and loss tangent of Vectorply E-LT 2400-7P composite samples, fiber oriented parallel to coaxial center conductor. Sample to sample variation indicates permittivity ranges from 3.95 - 4.2, loss tangent ranges from 0.015 - 0.04.

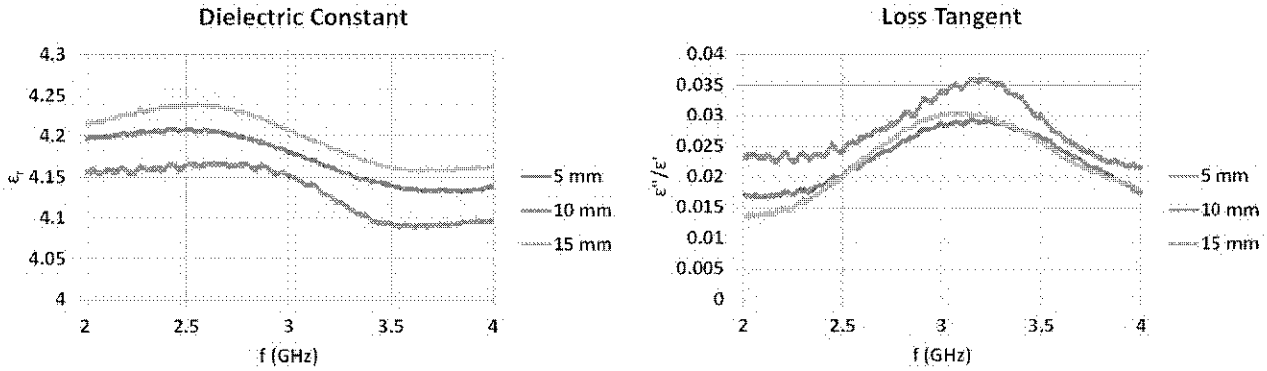

Figure 38 Measured permittivity and loss tangent of Vectorply E-LT 2400-7P composite samples, fiber oriented perpendicular to coaxial center conductor. Sample to sample variation indicates permittivity ranges from 4.1 - 4.25, loss tangent ranges from 0.015 - 0.035.

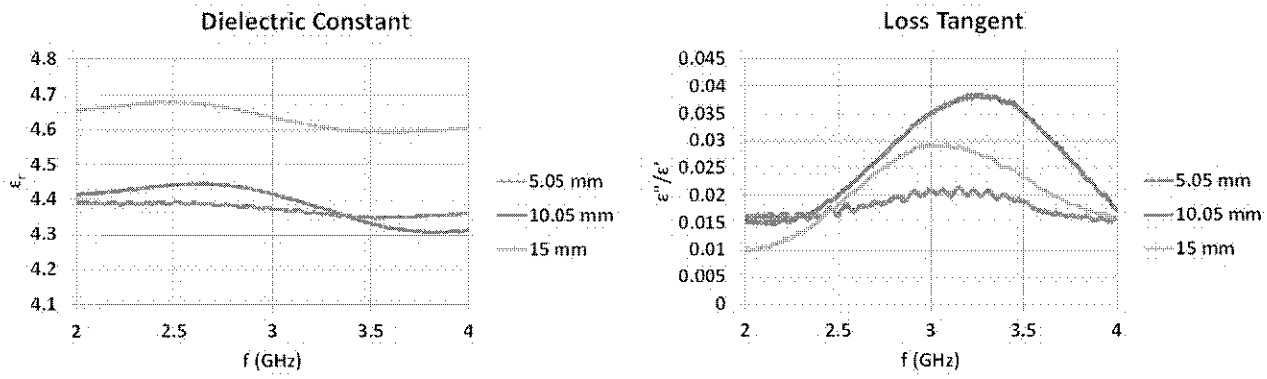

Figure 39 *Measurements of Vectorply E-LT 5500-10 composite samples, fiber oriented parallel to center conductor. Variation indicates permittivity range from 4.3 - 4.7, loss tangent range from 0.01 - 0.04.*

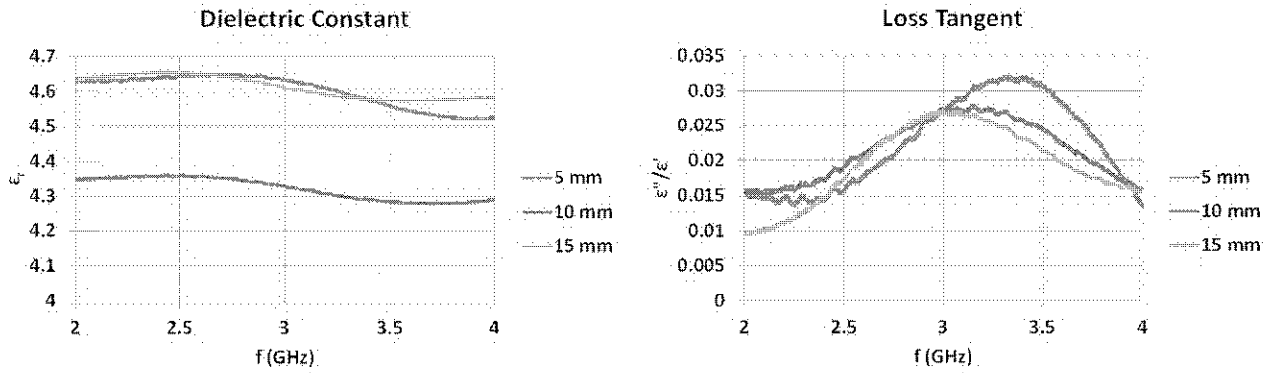

Figure 40 *Measured permittivity and loss tangent of Vectorply E-LT 5500-10 composite samples, fiber oriented perpendicular to coaxial center conductor. Sample to sample variation indicates permittivity ranges from 4.3 - 4.7, loss tangent ranges from 0.01 - 0.035.*

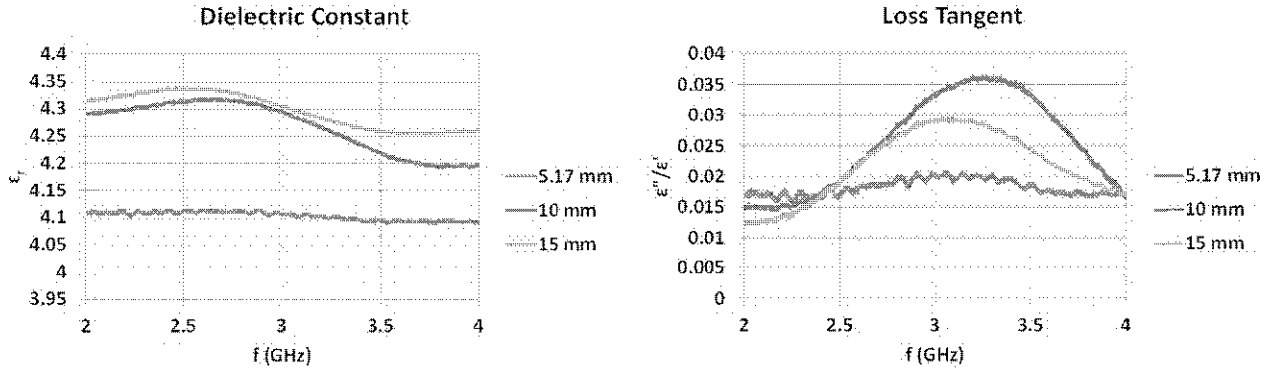

Figure 41 *Measurements of SXQ3600R1 composite samples, fiber oriented parallel to center conductor. Variation indicates permittivity range from 4.1 - 4.35, loss tangent range from 0.01 - 0.035.*

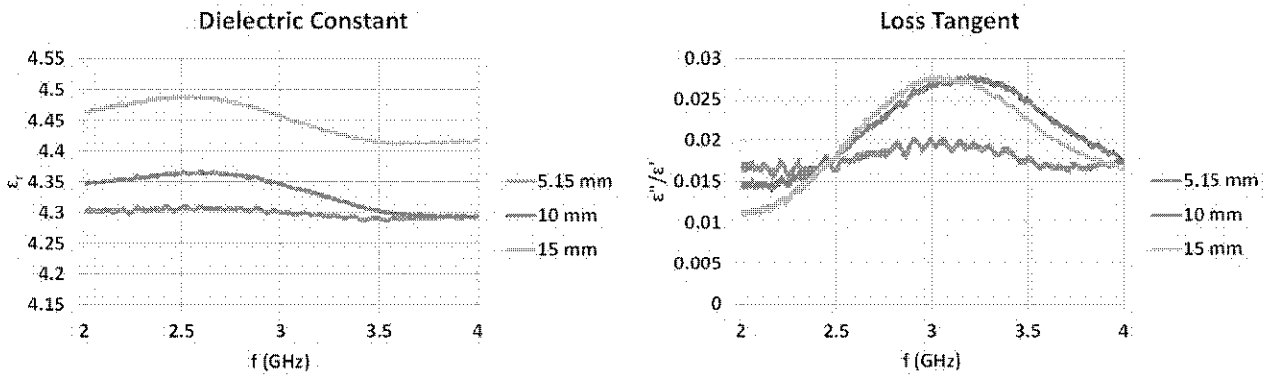

Figure 42 *Measured permittivity and loss tangent of SXQ3600R1 composite samples, fiber oriented perpendicular to coaxial center conductor. Sample to sample variation indicates permittivity ranges from 4.3 - 4.5, loss tangent ranges from 0.01 - 0.03.*

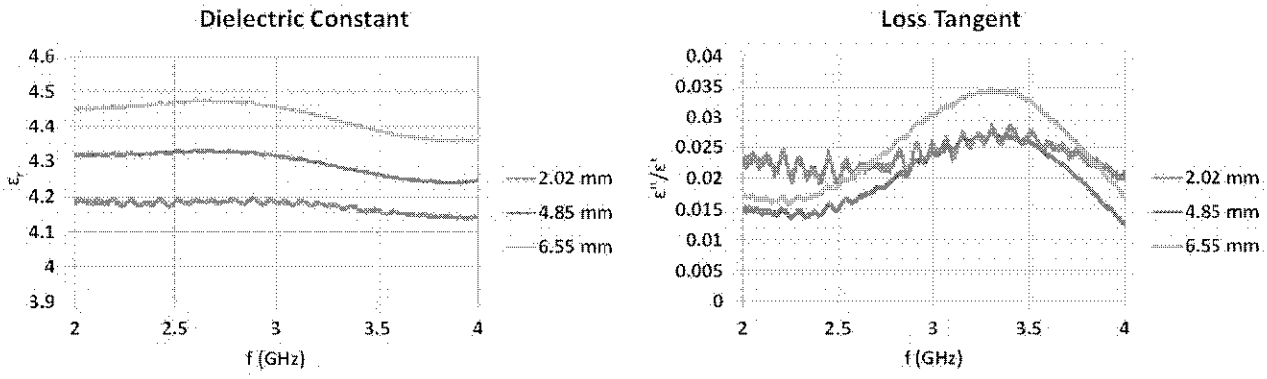

Figure 43 *Measurements of glass from commercial blade, fiber orientation unknown. Variation indicates permittivity range from 4.1 - 4.5, loss tangent range from 0.01 - 0.035.*

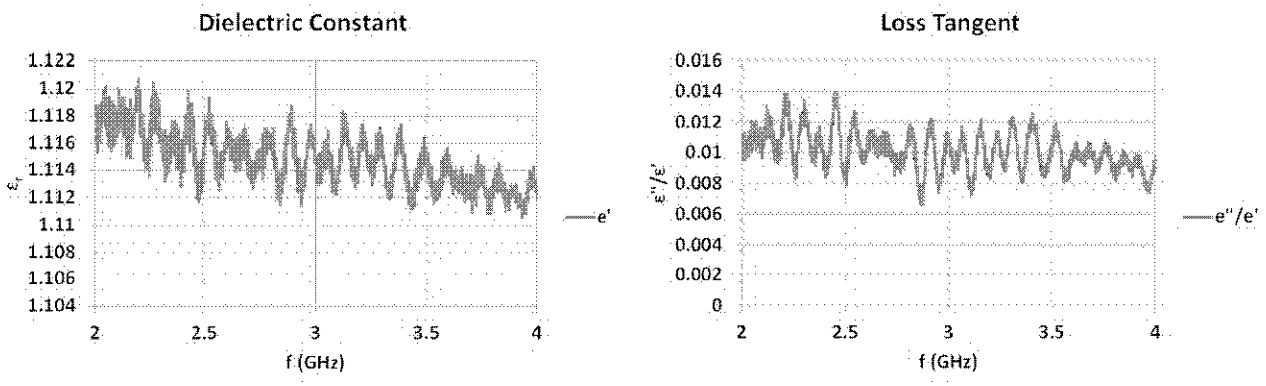

Figure 44 *Measured permittivity and loss tangent of foam core from commercial blade. Sample to sample variation indicates permittivity ranges from 1.11 - 1.12, loss tangent ranges from 0.006 - 0.014.*

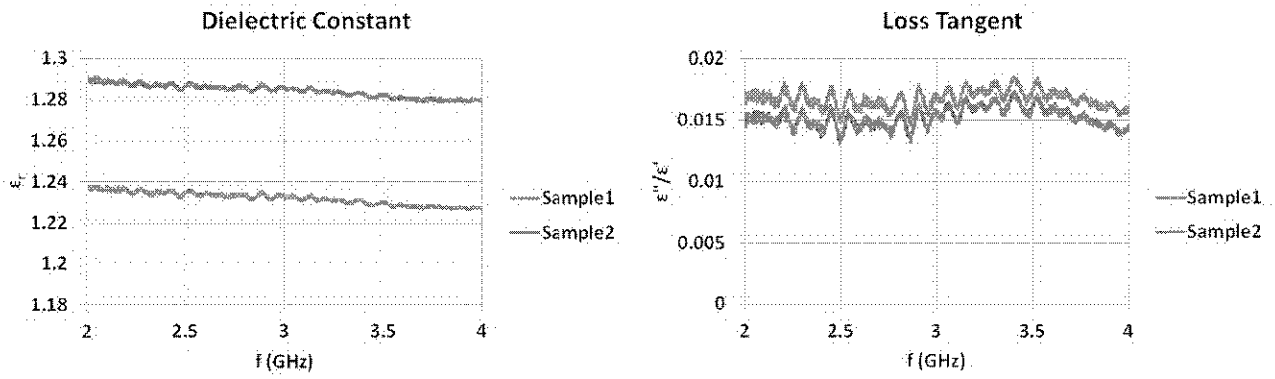

Figure 45 *Measured permittivity and loss tangent of balsa core from balsa reference panel. Sample to sample variation indicates permittivity ranges from 1.2 - 1.3, loss tangent ranges from 0.015 - 0.02.*

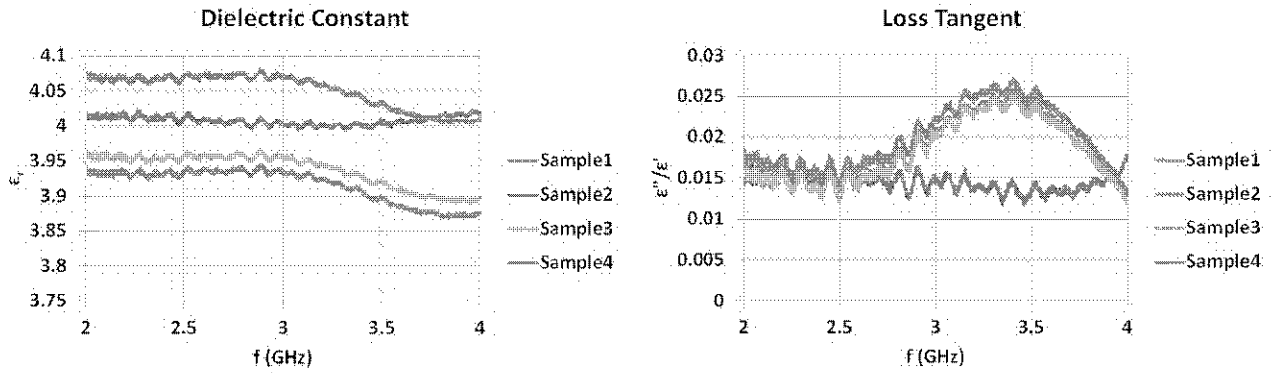

Figure 46 *Measured permittivity and loss tangent of glass skins from balsa reference panel. Sample to sample variation indicates permittivity ranges from 3.9 - 4.1, loss tangent ranges from 0.01 - 0.025.*

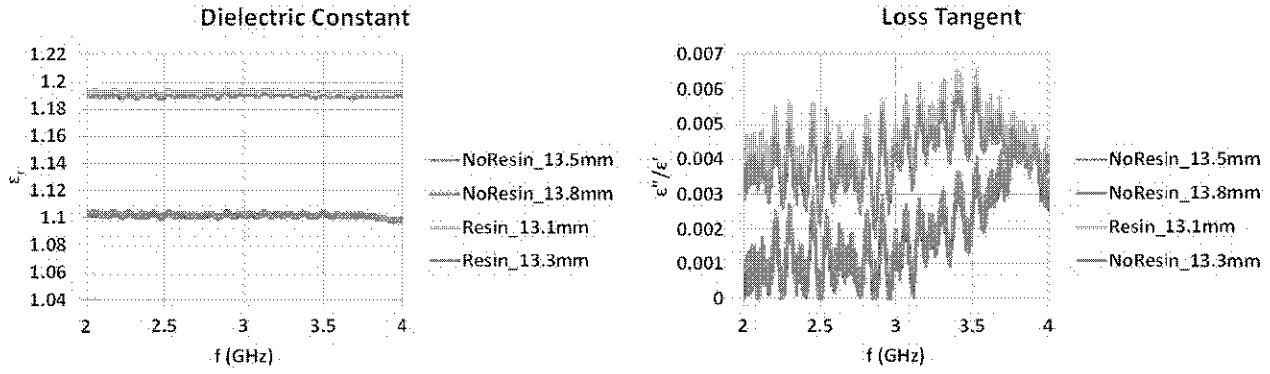

Figure 47 *Measured permittivity and loss tangent of foam core from foam reference panel. Sample to sample variation indicates permittivity ranges from 1.1 - 1.2, loss tangent ranges from 0.0 - 0.006.*

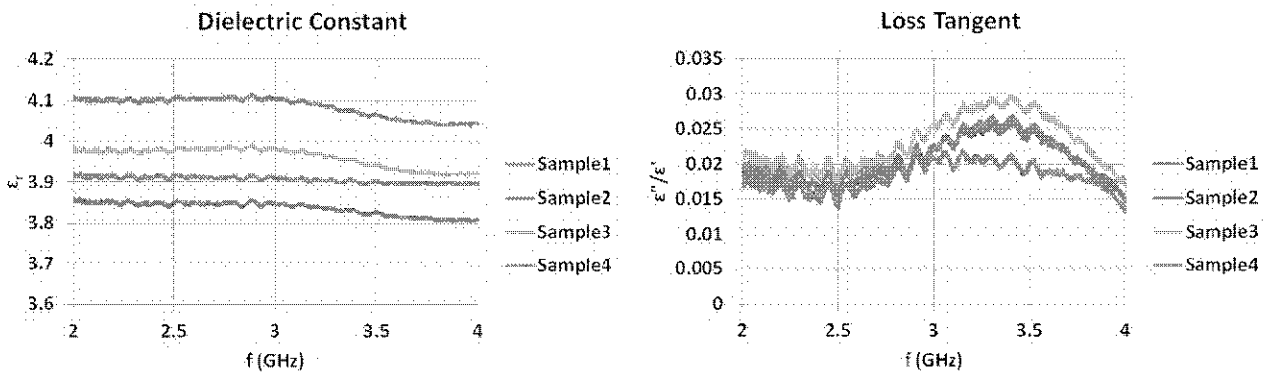

Figure 48 Measured permittivity and loss tangent of glass skins from foam reference panel. Sample to sample variation indicates permittivity ranges from 3.8 - 4.1, loss tangent ranges from 0.015 - 0.025.

4.2 Resistive Materials

In order to achieve an integrated absorber, electrically lossy materials must be introduced into blade fabrication. For Jaumann absorbers, the loss mechanism consists of resistive sheets. For Dallenbach absorbers, the loss mechanism consists of thick layers. Since most fabric tows used in VARTM processes have a finite thickness (30-50 mils), the chosen approach could be characterized as a combination of Jaumann and Dallenbach absorbers. The following approaches were investigated to fabricate resistive sheets, or thin lossy layers, with well-controlled electrical properties:

- Coating glass fabrics with conductive polymers or carbon.
- Deposition of thin metal layers.
- Growing carbon nanostructures on glass fabrics
- Various other carbon based treatments

Coated fabrics were procured from two companies: Eeonyx Company supplied EeonTex, a textile coated with conductive polyaniline or polypyrrole [88, 89], and Cuming Microwave Company supplied space cloth, a lightweight woven fiberglass coated with carbon.

The carbon nanostructure approach is based directly on work by Owens Corning and Applied Nanostrucure Solutions. These companies are developing carbon enhanced reinforcements (CER), in which carbon nanostructure are grown directly on glass fibers to control both mechanical and electrical properties. As carbon fiber is commonly used in wind-turbine blades, and its use will likely increase as blades grow larger, this technology has great potential to meet both mechanical and electrical design constraints with no modification to fabrication processes. Carbon is a common absorber material with natural abundance that has been used as a loss mechanism in numerous forms [90, 91, 92, 93, 94, 95, 96]. Although time and scope prevented a more in-depth investigation of various carbon based absorbers (graphene-based, nanostructures, fabrics) carbon based loss mechanisms should be investigated more thoroughly.

Thin metal layer deposition is commonly used in the semiconductor and integrated circuit industry to print resistors and other electronic devices. Although typically used on a significantly smaller scale than a wind-turbine blade, scaling deposition technologies to print large tape or pre-preg sheets could be a viable treatment option (e.g. aluminized Mylar™ or Kapton™). Thin metal layers of aluminum, silver and titanium are readily commercially sputtered or evaporated onto looms of polymer film for manufacturing processes such as hermetic food packaging, metallized displays/balloons/wrapping paper and high thermal reflectance "space" blankets. At Sandia, ready access to a 24" x 24" (0.6 x 0.6 meter) area titanium sputtering tool enabled fabrication of a range of sheet resistance values, and evaluation of suitability of these films in a resin curing

blade manufacturing process. Titanium was chosen because a titanium target was already loaded in the deposition chamber; cheaper materials such as aluminum could be used at larger scales with little performance change.

To determine the resistivity control of deposition processes, several titanium layers of varying thickness were deposited on silicon wafers and measured with a four-point probe thickness to produce and evaluate a wide range of sheet resistance values. Validation of these models will be reported in Part 2 of this report, on 18" wide fiberglass/resin composite panels containing integrated conductive layers of titanium on perforated Mylar™ or Kapton™ sheets. Films of titanium from 2.3 to 16 nm thick were deposited on silicon, Mylar™ and Kapton™ substrates to develop a map of sheet resistance values vs. film thickness as shown in Figure 49. A range of sheet resistance values from 100 Ω/square to 2000 Ω/square was readily developed using this method; the process has predictable resistivity change with thickness and can be well controlled to achieve desired sheet resistances. Sheet resistance is defined as resistivity divided by film thickness, and the expected linear 1/t dependence is observed experimentally, as shown at right in Figure 49. The slight deviation from pure 1/t behavior, 1/(t-3nm), is attributed to the finite surface roughness of the silicon and polymer substrates, and potential oxidation of titanium during film deposition. Titanium oxidation rate varies with temperature, so resistivity was measured both before and after temperature anneal to characterize oxidation effects and compensate for elevated temperature curing steps used during VARTM.

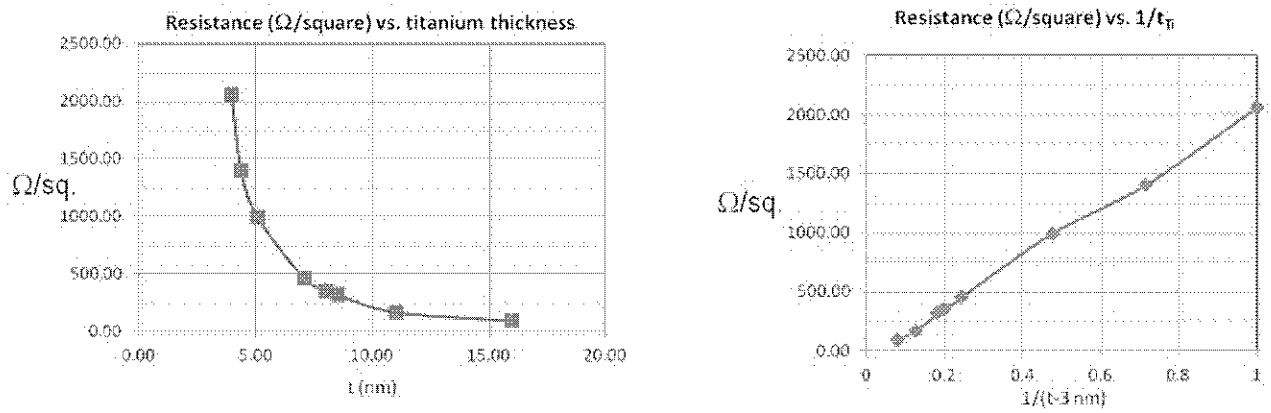

Figure 49 Sheet resistance of sputtered Ti films (left) and linear dependence of sheet resistance on inverse film thickness 1/t (right).

Perforated polymer sheets of designed sheet resistance values are currently being integrated into VARTM resin/fiberglass composite blade panel manufacturing process, in order to produce 18" x 18" panels of the reduced RCS spar cap and panel sections shown in *Design of Blade-Representative Test Samples*. The RCS evaluation results of these manufacturable, modified spar-cap and panel designs will be reported in Part 2 of this report. It appears that both coated fiberglass and thin metallized layers of perforated polymer sheets may enable straightforward integration of quantitative, designed resistance-value layers into commercial blade manufacturing processes, a first step to achieving Jaumann absorber type RCS reduction.

4.3 Designed Dielectric Composite Materials

To achieve low-RCS composites without materially changing composite blade manufacturing processes, mechanical reliability or cost, it is desirable to modify the electrical properties of blades by either subtly changing the fiber orientation or content, or by including minor additions in the manufacturing process that may dramatically alter composite blade electrical properties. To achieve this, reliable electromagnetic models of blades as a function of structure (i.e. fiberglass lay-up and orientation) and blade-material composition is necessary. Toward this end, we have considered in this study the range of electrical-property modification

feasible with minor changes in fiberglass or second phase content. The prediction and analysis of composite electrical properties is described below, using dielectric mixing rules and validation.

4.3.1 Designed Composites: Series, Parallel and Effective Medium Mixing

Preparing designed electrical or electromagnetic composites of polymer, dielectrics, and magnetic materials is an active area for reducing RF interference in electronic devices, as well as for production of low-cost RF-circuit elements. Binary mixture rules have been widely developed to enable fabrication of designed permittivity polymer-dielectric electromagnetic composites for wireless electronics applications. Modeling of mixtures of dissimilar materials has developed effective mixing rules for predicting properties of composite materials. Three approaches that serve as guides are modeling mixtures as capacitors in parallel (parallel mixing), as capacitors in series (series mixing), or as an effective medium, in which dielectric particles are small compared to wavelength, so the entire structure may be treated as a composite material of uniform property. The parallel mixing rule applied to dielectrics simply results in the algebraic average of the two permittivities as a function of volume fraction, or $\varepsilon_r = x_1 \varepsilon_1 + x_2 \varepsilon_2$, where x_i is the volume fraction of each phase and ε_i is the dielectric constant of that phase; this may be envisioned as parallel columns of uniform material in the direction of applied electric field. This condition may be observed when uniaxial fiberglass is in the plane of the electric field – a solid column of glass surrounded by solid columns of resin. The series mixing rule models two materials as one layer atop the other or $1/\varepsilon_r = x_1/\varepsilon_1 + x_2/\varepsilon_2$, which is equivalent to $\varepsilon_r = (\varepsilon_1\varepsilon_2,)/(x_1\varepsilon_2 + x_2\varepsilon_1)$. In the series mixing rule, the low permittivity phase dominates the composite behavior, since electric field is concentrated in this phase by the ratio $\varepsilon_{high}/\varepsilon_{low}$. The practical effect of this is that porosity ($\varepsilon = 1$) or a low permittivity matrix phase may dominate electrical behavior for laminate materials, such as layers of woven biaxial fiberglass interspersed with resin, with the electric field perpendicular to the biaxial glass direction.

In a third class of condition, known as effective medium theory (EMT), Maxwell-Garnett mixtures, or the Bruggeman formula, a matrix with a well-dispersed second phase, where the particle size is much smaller than the incident wavelength, and where there is no columnar or plate-like orientation, allows treatment of the composite as a medium with isotropic properties. This method is typically accurate for spheroidal, non-percolating inclusions in a 3D matrix, termed a 0-3 composite. The three formulae provide similar predictions, using either the simplified logarithmic form, derived from Maxwell's equations, and termed the Lichtenecker logarithmic formula: $\log \varepsilon_r = x_1 (\log \varepsilon_1) + x_2 (\log \varepsilon_2)$, or the full effective medium theory equation $\varepsilon_r = \varepsilon_1 + [x_2 \varepsilon_1 (\varepsilon_2 - \varepsilon_1)] / [\varepsilon_1 + x_1 (\varepsilon_2 - \varepsilon_1)]$.

These theories may be modified further to include resin-rich layers in parallel or series with resin/fiberglass layers, to develop accurate models of electromagnetic properties for real turbine composites. In addition, this approach enables design of custom dielectric materials by inclusion of low ε_r or high ε_r filler particles in resin alone, or in a resin-fiberglass composite. Property predictions for a mixture of wind-turbine resin, electrical permittivity 2.9, and E-glass fiberglass, permittivity 6.2, are in Figure 50, along with measured results. Here, both fiberglass composites measured with electrical field parallel and perpendicular to the fiber direction are shown. The observed behavior of 50 volume% Epikote resin and Vectorply E-glass composites appears to fall between the lower bound predicted by series mixing (fibers perpendicular to electric field) and that predicted by a 0-3 composite effective medium approximation.

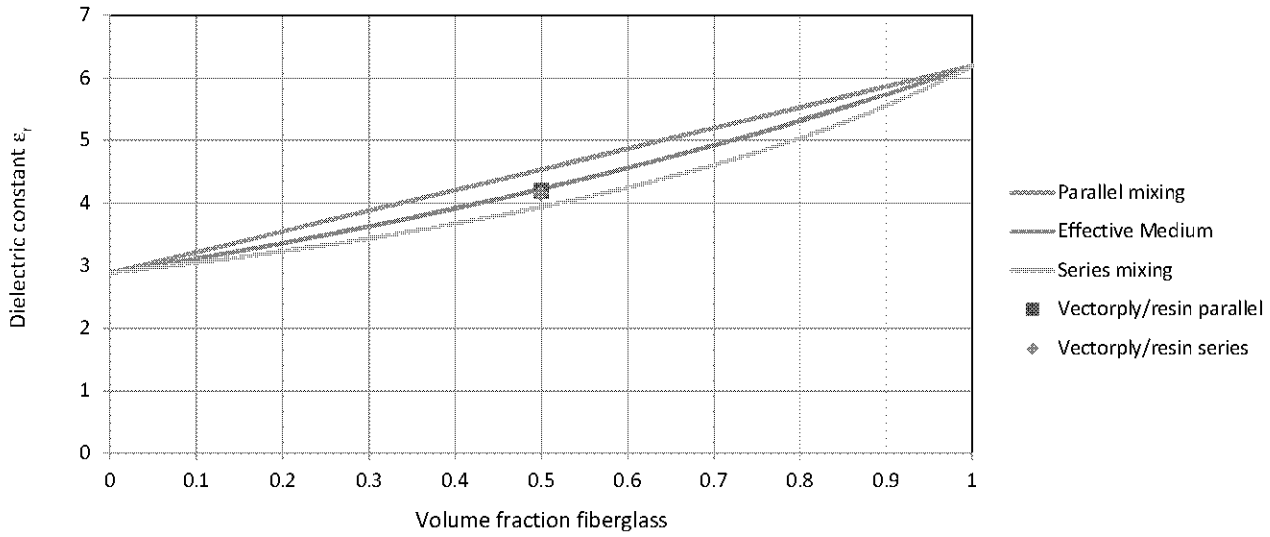

Figure 50 *Comparison of dielectric mixing rules for Epikote resin, ε_r = 2.9, and Vectorply E-glass, ε_r = 6.2 used in turbine-blade manufacturing. The data points show real data for a 50 volume % biaxial E-glass sample, where the electric field is parallel to the fiberglass columns (parallel electrical mixing) or perpendicular to the fiberglass columns (series mixing).*

Historically, the effective medium or Lichtenecker logarithmic approximations have been most accurate for widely developed dielectric-polymer composites used for control of electromagnetic interference from wireless electronics. While the three models provide similar predictions for the resin/fiberglass system, which displays low dielectric contrast, the models provide starkly different results for high dielectric contrast systems, as will be shown below.

4.4 Designed Composites using Dielectric Fillers

Limiting bulk materials to those already existing in wind blades significantly constrains absorber design. As can be seen from the measurements above, existing dielectric constants are constrained to ε_r = 1.2 - 4.6, and magnetic materials are not available in standard blades. Several novel dielectric materials were developed to expand the design space.

Modeling using effective medium methods, in which $\log \varepsilon_{total} = x_1 \log \varepsilon_1 + x_2 \log \varepsilon_2$, suggests the largest modification of blade electrical properties would be achieved by inclusion of a high permittivity material with temperature-stable properties such as $BaTiO_3$, with $\varepsilon' \sim 3000$. As shown in Figure 51, the addition of varying amounts of $BaTiO_3$ to the base resin, with a permittivity of 2.9, would enable significant changes to materials permittivity, while still using a low enough volume fraction of filler phase to allow composite processing.

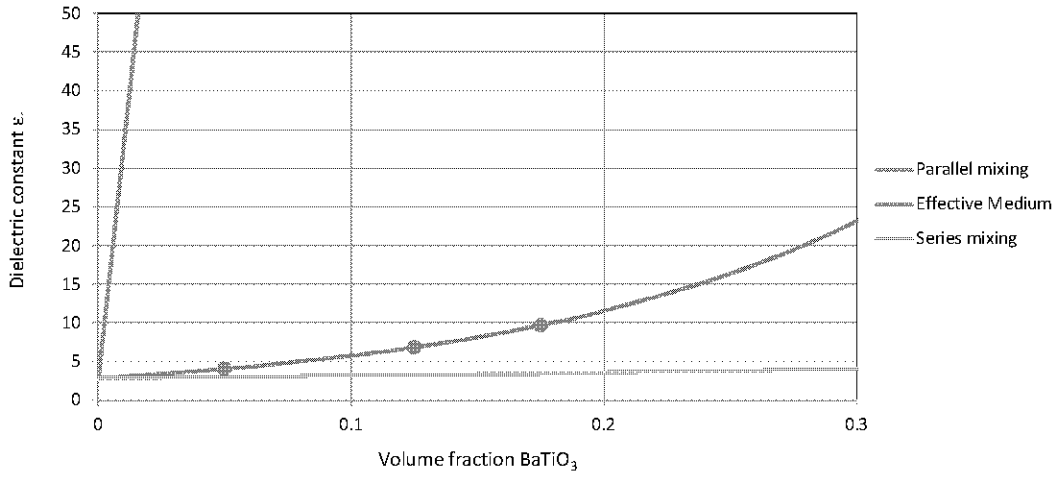

Figure 51 *Three achievable, low viscosity loadings of high permittivity BaTiO3 to modify the permittivity of the base Epikote turbine-blade composite resin (e ~ 2.9):*
5 volume % BaTiO3/95% resin, ε ~ 4
12.5 volume % BaTiO3/87.5% resin, ε ~ 7
17.5 volume % BaTiO3/82.5% resin, ε ~ 10

For volume fractions above 20 volume % $BaTiO_3$, there is a significant increase in resin viscosity, which would require significant modifications to traditional resin-flow blade manufacturing processes, such as pursuing a pre-preg process in which partially-cured layers are laminated instead of vacuum-infused with resin. Additionally, $BaTiO_3$ and other high permittivity dielectrics possess a high density ($BaTiO_3$ ρ = 6 g/cc, while resin ρ ~ 1.2 g/cc) which could cause very large increases in blade mass. Because of this weight penalty, and the potential for a more-costly manufacturing process, we have not considered higher volume-fraction loadings than 20%. By using combinations of closed-cell foams, resin/fiberglass of variable loadings, and high-permittivity loaded resin composites, a range of permittivity values from 1.1 to 10 appears achievable in VARTM or pre-preg composite processing, to achieve the types of low RCS designs discussed in *Design of Blade-Representative Test Samples*. Use of the 50 volume % of the permittivity 10 resin/$BaTiO_3$ composite with 50 volume % fiberglass may enable wind-turbine composites with permittivity 7.9, compared to 4.2 for traditional composites, using a similar mechanical structure. Additions of such particles to resin/fiber systems has been examined previously and, in many cases been beneficial to fracture toughness, but the mechanical properties and reliability of such filled composites would require testing and qualification in future development work.

4.5 Integration into Wind-Turbine Fabrication Processes

RCS reduction treatments must not only maintain blade structural integrity; they must also be built in a manner that is minimally invasive to existing fabrication processes. Balancing these two drivers, it appears Jaumann absorbers with resistivity values of 100-2000 Ω/square and dielectric layers of permittivity 1.2 - 10 may be achieved using traditional fiberglass layup and resin vacuum infiltration processes. Two approaches were taken to modify blade electrical properties:

- Replace glass fabric layers with resistive layers, or insert thin resistive layers in a standard stack-up.
- Replace standard resins and core materials with doped variants which increase electrical permittivity, permeability, conductivity, or a combination of the three.

Both approaches require minimal adjustment to fabrication processes. For the first, replacing or adding layers requires minimal oversight, as long as the inserted layers do not significantly reduce mechanical strength. For the second, resin and/or core materials, bought in bulk, are simply replaced with doped variants. Vacuum-assisted resin transfer molding (VARTM) processes remain the same if doped materials maintain a viscosity

comparable to untreated resin. Due to existing capabilities at SNL, VARTM processes were chosen to demonstrate RAM compatibility with blade fabrication processes. The RAM treatments discussed in this report could be implemented with modification in a pre-preg process.

5. Design of Blade-Representative Test Samples

5.1 Introduction

In this section, material measurements from *Material Development and Integration* are provided as inputs into models developed in *Development of Absorptive Treatment* to design absorbers which can be integrated into a wind-turbine blade with minimal impact on blade fabrication process and mechanical performance. Integrated absorbers were designed for both sandwich (glass-foam-glass) and spar-cap (biaxial glass-uniaxial glass-biaxial glass) structures. All absorbers are 1.2 inches thick, since this represented a reasonable thickness for a significant portion of 45–60 meter blades. Absorbers were designed for optimal performance over 2.7-2.9 GHz, as this band covers many airport surveillance radars (ASR-8, ASR-9, ASR-11, etc.).

Absorbers integrated into sandwich structures indicate a high level of RF performance can be achieved with a relatively simple absorber design. At normal incidence, a nominal reflection loss of 23 dB or greater is achieved from 2.7-5.0 GHz. At oblique angles of incidence 30° or less, a nominal reflection loss of approximately 20 dB or greater is achieved over the same bandwidth. RF performance is more limited for absorbers integrated into spar-cap structures. At normal incidence, a nominal reflection loss of 20 dB or greater is achieved from 2.6-3.0 GHz. At oblique angles of incidence 20° or less, a nominal reflection loss of 20 dB or greater is achieved over the same bandwidth. Statistical analyses were performed to evaluate design sensitivity to fabrication variations. Analysis indicates that, although process tolerances will be an important consideration in actually building low RCS blades, designs are robust and insensitive to fabrication variation.

5.2 Design Approach

Two integrated absorbers were designed – one solid glass, representing a spar-cap structure, and one foam and glass, representing a sandwich panel. These two structures cover a significant area of a wind-turbine blade, making them good candidates for integrated absorber designs from both a fabrication and RF performance perspective. Figure 52 illustrates the integrated absorber design for the sandwich structure, along with an untreated sandwich structure for comparison. The absorptive treatment consists of two resistive sheets, one of which is embedded into the foam core, along with a metal or carbon backing. Figure 53 illustrates the integrated absorber design for the spar-cap structure, along with an untreated spar-cap structure for comparison. The absorptive treatment consists of one resistive sheet embedded into the uniaxial glass core, along with a metal or carbon backing.

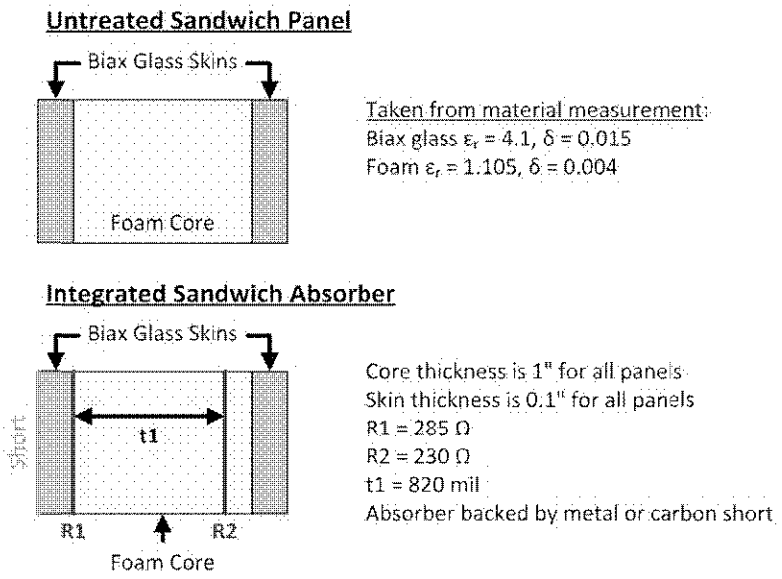

Figure 52 Untreated sandwich panel compared to sandwich panel with integrated absorber.

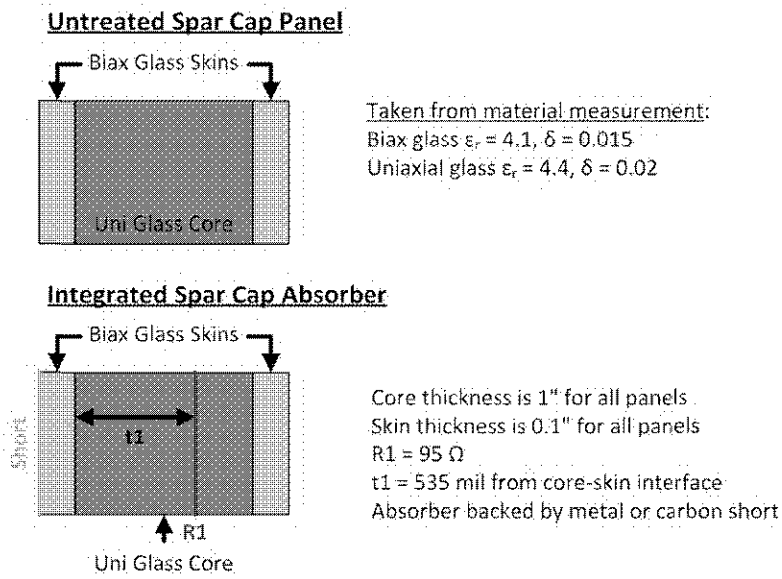

Figure 53 Untreated spar-cap panel compared to a spar cap with integrated absorber.

Material properties (permittivity and loss tangent) were based on Table 3. Resistive sheets were assumed to be infinitely thin. Actual thicknesses can be incorporated with little to no change in design performance, since the sheets will be thin relative to a wavelength at S-band.

Both sandwich and spar-cap absorbers were designed with simplicity in mind, i.e. the impact of absorber integration should be relatively minimal in terms of both process changes and mechanical performance. The goal was to achieve moderate electrical performance with low fabrication complexity and high mechanical performance. Alternative approaches such as improving RF performance at the cost of additional fabrication complexity or reduced mechanical strength could be investigated in the future. As further material developments enable control of dielectric or magnetic properties, future designs could achieve improved RF performance with doped materials. Furthermore, additional resistive sheets, or Dallenbach resistive layers, could be inserted to improve performance or reduce sensitivity to fabrication variation. The trade space between electrical performance, mechanical performance, process simplicity, and cost is extremely large.

Due to the constrained design space (thickness and material properties set), the design process used random and gradient optimization techniques to achieve the best performance over a reasonable range of incident angles at 2.7 -2.9 GHz. The optimization goals and design parameters are contained in Table 4 through Table 7.

Table 4 Optimization Goals: Integrated Sandwich Absorber

Goal	Weight	Bandwidth	Return Loss	Angles Of Incidence	Polarization
1	1	2.7-5.0 GHz	< -20 dB	0°	Both
2	1	2.7-5.0 GHz	< -20 dB	30°	TE
3	1	2.7-5.0 GHz	< - 20 dB	30°	TM

Table 5 Optimization Goals: Integrated Spar-cap Absorber

Goal	Weight	Bandwidth	Return Loss	Angles Of Incidence	Polarization
1	1	2.6-3.0 GHz	< -20 dB	0°	Both
2	1	2.6-3.0 GHz	< -20 dB	20°	TE
3	1	2.6-3.0 GHz	< - 20 dB	20°	TM

Table 6 Design Parameters: Integrated Sandwich Absorber

Parameter	Unit	Range	Optimized Value
R1	Ω/square	1-1000	285
R2	Ω/square	1-1000	230
t1	mil	1-999	820

Table 7 Design Parameters: Integrated Spar-cap Absorber

Parameter	Unit	Range	Optimized Value
R1	Ω/square	1-1000	95
t1	mil	1-999	535

5.3 Nominal Designs – RF Performance

Figure 54 contains RF performance for the integrated sandwich absorber shown in Figure 52, and Figure 55 contains RF performance for the integrated spar-cap absorber shown in Figure 53. Both figures contain return loss at normal and oblique incidence angles. Comparing RF performance to the optimization goals indicates that the goals were well met. ADS' optimization tools calculate an error function based on the goals provided in Table 4 and Table 5, each of which is assigned a weighting function to represent relative importance. In this case, the weighting function is 1 for all goals; RF performance at normal incidence and oblique incidence carry the same weight. Optimization techniques, whether random or gradient, attempt to minimize the error function by varying appropriate design parameters. The error function (EF) provides a figure of merit for each design, with EF = 0 representing a design that meets all goals. For the integrated sandwich absorber, the EF = 0.125. For the integrated spar-cap absorber, the EF = 0. Note that the optimization goals for the spar cap apply over a narrower bandwidth, as initial attempts to create a broadband spar-cap absorber failed.

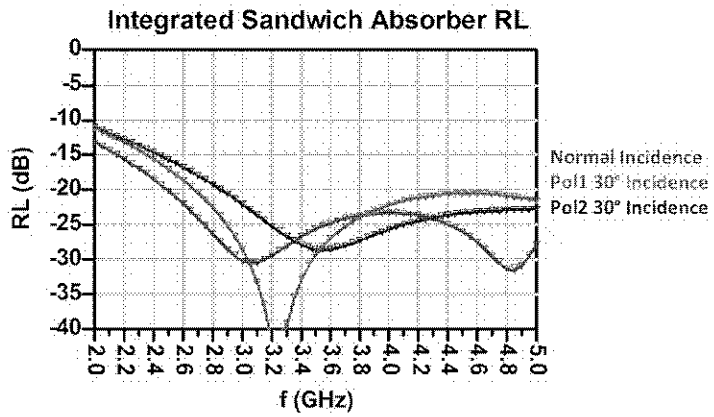

Figure 54 *Return Loss at normal and oblique incidence for an integrated sandwich absorber. Excellent agreement between ADS and HFSS validates the ADS model and design approach. Return loss of 20 dB or better is achieved over 2.8-5 GHz out to a 30° incident angle.*

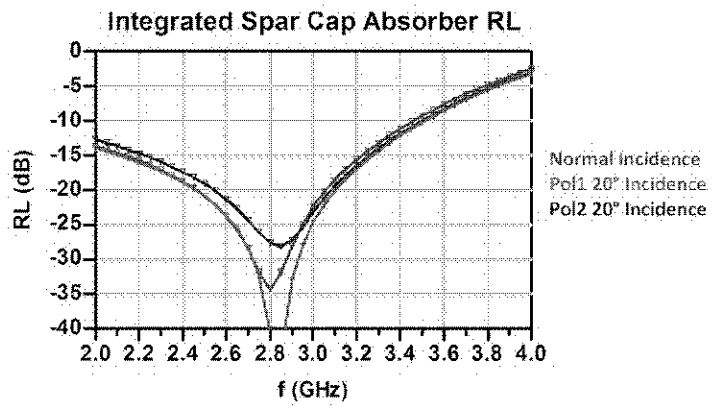

Figure 55 *Return Loss at normal and oblique incidence for an integrated spar-cap absorber. Excellent agreement between ADS and HFSS validates the ADS model and design approach. Return loss of 20 dB or better is achieved over 2.6-3 GHz out to a 20° incident angle.*

The RF performance of the integrated absorbers is exceptional considering the simplicity of the design (insert two or three resistive or conductive sheets in an existing VARTM fabrication process). Design simplicity and the reliability of design parameters (designs are based on measurements of foam, glass composites, and resistive materials) indicate a smooth transition to prototyping and validation measurements.

5.4 Statistical Analysis & Fabrication Considerations

The designs presented in the previous section assume a perfect fabrication process. All design parameters are exact values. In reality, a number of design parameters will vary across a range determined by process controls during fabrication. To evaluate whether the designs perform well during an actual fabrication process, a series of statistical analyses was performed to reveal how process variations determine performance variation. The following design parameters were allowed to vary according to a Gaussian distribution:

- Biaxial glass skin dielectric constant – Varied from 3.95 - 4.25
- Uniaxial glass core dielectric constant – Varied from 4.3 - 4.5
- Glass skin thickness – Varied +/- 0.02”
- Resistive sheets – Varied +/- 5%
- Resistive sheet location – Varied +/- 0.02”

Dielectric constant variations were taken from material measurements (see *Material Development and Integration*), which represent the worst case in terms of process control. Resistive sheet values were chosen based on vendor claims and in-house capabilities (see *Resistive Materials*). Sheet locations and thickness variations were based on measurements of reference plates and GR900 samples (see *Fabrication of Test Panels*). Loss tangents did not vary, as initial analysis indicated their impact on performance was minimal. Foam core thickness did not vary, as thickness measurements of core material before and after reference panel fabrication indicated excellent control. Foam core dielectric constant did not vary, as measurements indicated little to no variation in foam dielectric constant. Resin flow through the core will modify the effective dielectric constant in a predictable manner.

Process variations will result in degraded performance; however, metrics are needed to determine acceptable RF performance and establish percent yield. RF performance goals for the statistical analysis are presented in Table 8 and Table 9, along with the yield for each set of goals. These goals represent the criteria by which boards (or blades) would be evaluated to determine pass/fail in a mass-production environment. Yield analysis goals differ from those for the nominal design. The broadband nature of the sandwich absorber allowed yield evaluation over several frequency bands and performance metrics, whereas the spar-cap absorber was limited to narrowband goals from the nominal design.

Table 8 RF Performance Goals and Yield: Integrated Sandwich Absorber

Goal Set	Weight	Bandwidth	Return Loss	Angles Of Incidence	Polarization	Yield
1	1	2.7-4.0 GHz	< -20 dB	0°	Both	96.40%
1	1	2.7-4.0 GHz	< -15 dB	30°	TE	96.40%
1	1	2.7-4.0 GHz	< - 15 dB	30°	TM	96.40%
2	1	3-4 GHz	< - 20 dB	0°	Both	92%
2	1	3-4 GHz	< - 20 dB	30°	TE	92%
2	1	3-4GHz	< - 20 dB	30°	TM	92%
3	1	3.2-3.5 GHz	< - 20 dB	0°	Both	98.10%
3	1	3.2-3.5 GHz	< -20 dB	30°	TE	98.10%
3	1	3.2-3.5 GHz	< - 20 dB	30°	TM	98.10%

Table 9 RF Performance Goals and Yield: Integrated Spar-cap Absorber

Goal Set	Weight	Bandwidth	Return Loss	Angles Of Incidence	Polarization	Yield
1	1	2.7-2.9 GHz	< - 20 dB	0°	Both	97.10%
1	1	2.7-2.9 GHz	< - 20 dB	30°	TE	97.10%
1	1	2.7-2.9 GHz	< - 20 dB	30°	TM	97.10%

Figure 56 shows RF performance variation due to process tolerances for the integrated sandwich absorber. The absorber meets goal set 1 in Table 8 and Table 9 for 96.4% of all cases – this corresponds to yield in a mass-production environment. Figure 57 shows RF performance variation due to process tolerances for the

integrated spar-cap absorber. The absorber yield is 97.1% for 20 dB return loss from 2.7-2.9 GHz out to a 20° incident angle. Figure 58 contains histograms of the various design parameters.

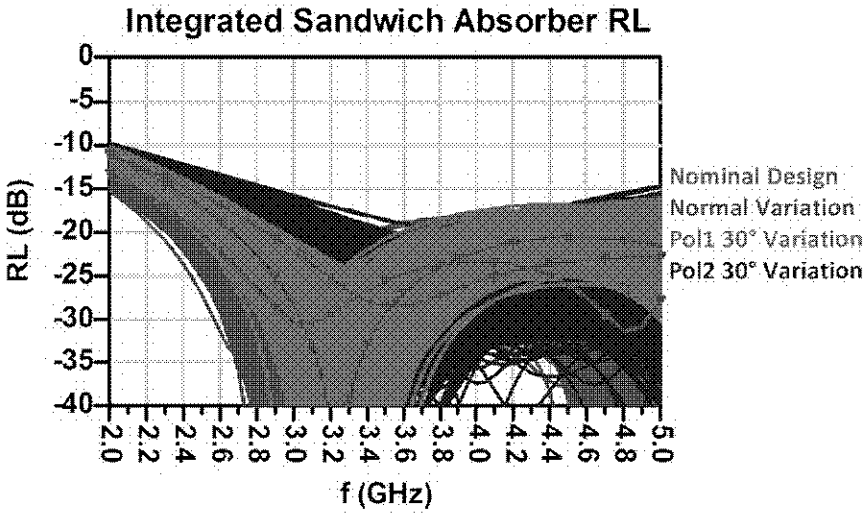

Figure 56 RF performance variation for the integrated sandwich absorber.

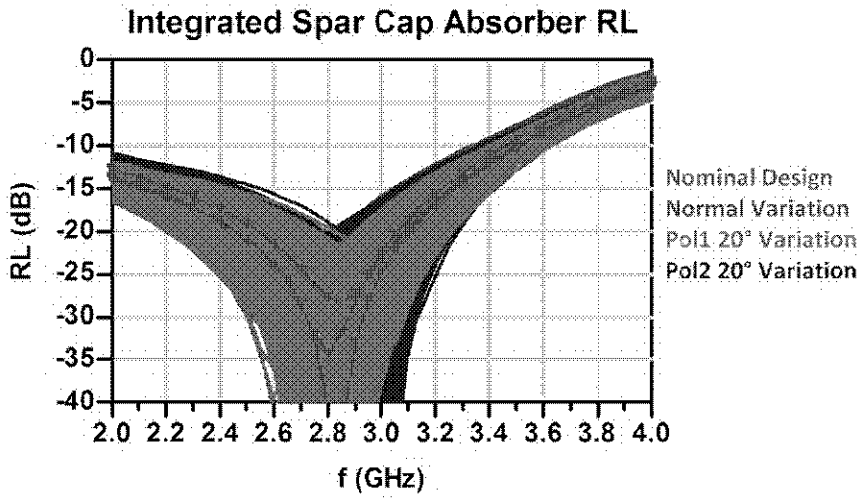

Figure 57 RF performance variation for the integrated spar-cap absorber.

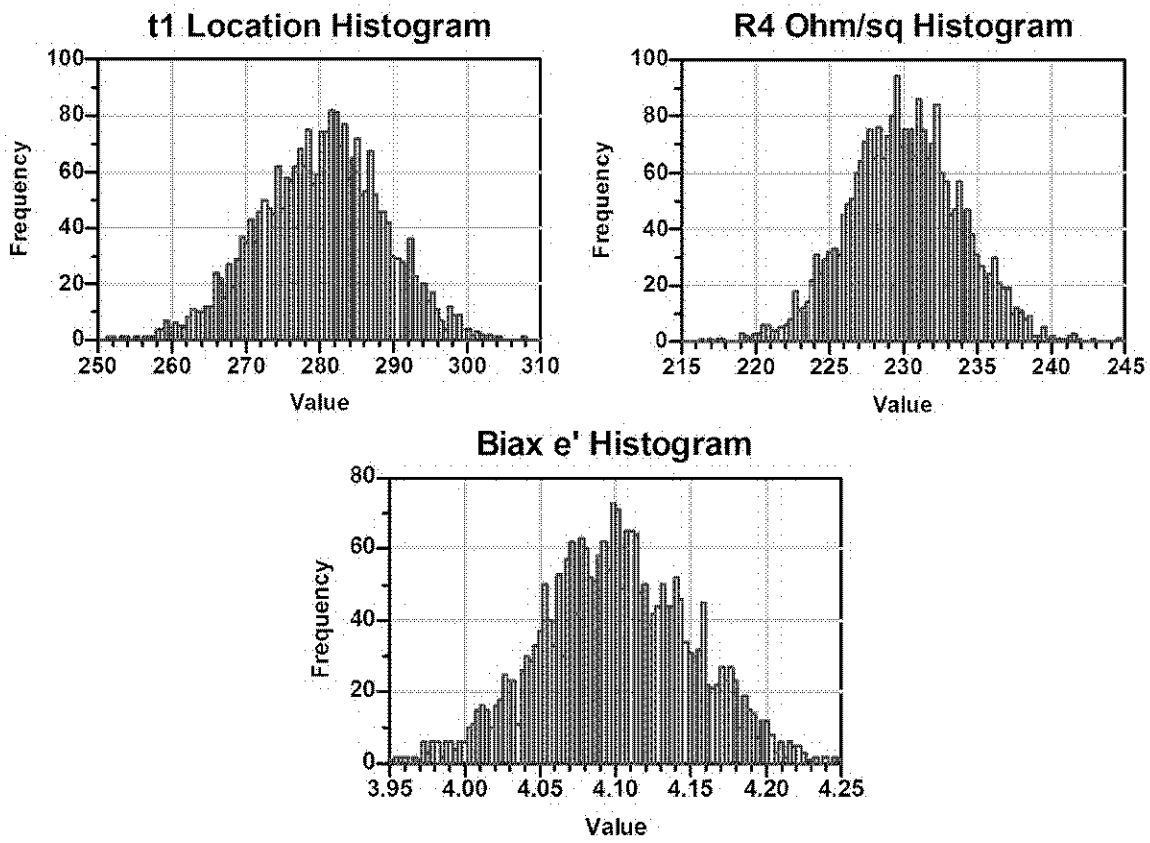

Figure 58 Representative histograms of several design parameters.

The nominal designs presented in the previous section were designed for higher performance over a wider bandwidth to account for the degradation shown in Figure 56 and Figure 57, hence the difference in nominal and statistical design goals. In future designs, yield improvement could be achieved with yield optimization, in which design parameters are optimized to compensate for process tolerances over a limited range. Further analysis could also identify which process tolerances critically impact RF performance. If ten design parameters vary, but only two significantly impact performance, process controls can focus on a more limited scope, reducing cost and effort.

Fabrication of the integrated absorbers presented above is currently in progress; measured results will be provided in Part 2 of this report. As prototype fabrication progresses, realistic process tolerances and design compensation for fabrication variation will be investigated further. All analysis to-date indicates 20 dB return loss over 2.7 - 2.9 GHz can be achieved with standard VARTM processes for both sandwich and spar-cap structures. The analysis presented above is based on standard VARTM processes applied to flat plates. All material and thickness variations were based on actual measurements from VARTM processes in which only standard process controls were applied. The following section addresses blade fabrication and process control in greater detail.

6. Absorber Integration into Turbine-Blade Fabrication

6.1 Typical Blade Fabrication

Modern wind-turbine blades are constructed predominately of E-glass or carbon-fiber reinforced polymers (polyester, vinylester, or epoxy) along with foam- or balsa-core materials. Blades are comprised of a load bearing I-type or box-type beam structure, commonly referred to as a spar enclosed by two aerodynamic shells.

The spar is the main load-bearing structure in the blade with respect to aerodynamic and gravitational bending. The spar consists of top and bottom flanges or spar caps which are made mostly of uni-directional fiber running in the spanwise direction of the blade, connected by one or more shear webs which are constructed of bi-directional fibers. Adjacent to the spar-caps, are panel regions – sandwich structures comprised of bi-directional, tri-directional, or quad-directional fibers on either side of a foam or balsa core. The panel regions provide torsional stiffness to the blade and are reinforced with core materials to prevent panel buckling. The major components of a wind-turbine blade are shown in Figure 59.

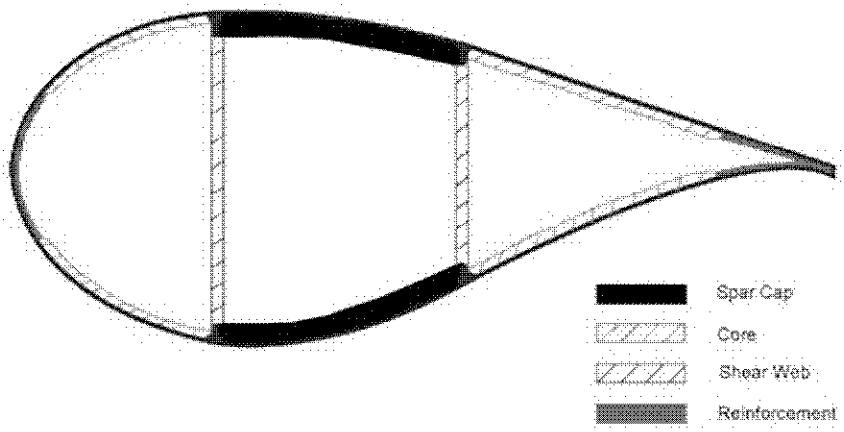

Figure 59 Cross-section showing typical wind-turbine blade construction.

Blades are typically manufactured through wet layup, VARTM, or pre-preg processes. Wet layup involves pre-wetted layers of composite material being laid down into the blade mold, and hand-rolled to remove excess resin. In the VARTM process, dry fabrics are laid in the blade mold, followed by resin being infused into the fibers through vacuum (see Figure 60). Pre-preg construction involves laying down layers of fiber which contains resin in a partially cured state. Of all the manufacturing processes, VARTM is the most common due to higher quality than wet layup and lower cost than pre-preg . In all of these processes, the thickness of individual plies is variable, though manufacturers use the thickest plies possible to speed manufacturing Also, material suppliers do not typically offer custom thicknesses for fiber and core materials, although that may be possible with enough demand. Finally, the layers are dropped, moving from root to tip, reducing the total laminate thickness as the loads on the blade decrease outboard. Thus, root sections might have a 10-15 cm thickness while tips may only be 1 cm or less.

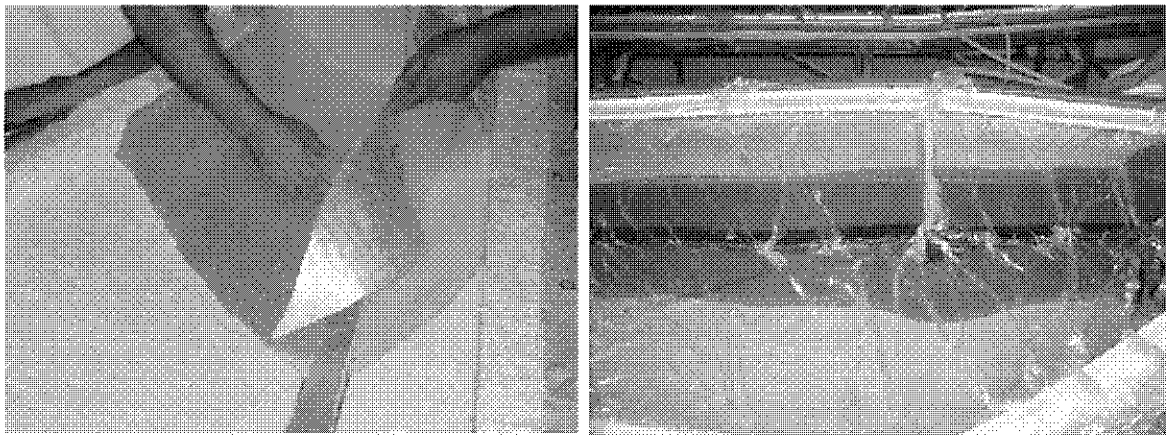

Figure 60 Dry fiber placement (left)and infusion (right) for VARTM blade manufacturing.

Once the fiber and resin have been placed in the mold, the structures are then cured, either at room or elevated temperatures. The separate pieces – skins and shear web or entire spar – are then adhered together (see Figure 61). Exceptions to this process include the use of pre-cured root and spar-cap assemblies that are infused with the skins, and, in the case of one manufacturer, a mold system that allows for the entire blade to be infused at once, eliminating the need for adhesive bonding.

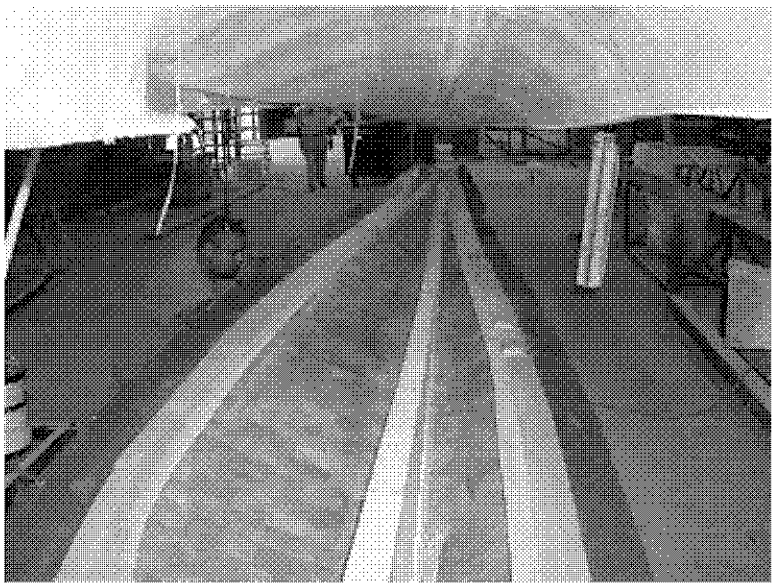

Figure 61 Final assembly of blade components.

6.2 Fabrication of Test Panels

Resin samples, flat laminate materials, and sandwich panels were produced for material-characterization purposes. The VARTM process was used to produce the laminate and sandwich panels. After these raw materials were produced, the material was finished into GR900 disks and sized sandwich panels (18 inches by 18 inches).

6.2.1 Materials:

A Hexion Epikote resin system, consisting of MGS RMR135 resin and MGS RIMH137 curative, was used to produce all of the above items. This resin system is specifically designed for glass and carbon fiber composite applications, including marine and wind energy (turbine blades). It has good mechanical properties (capable of high static and dynamic loading), and is a low-viscosity resin system that is well suited for infusion processes. Hexion also produces filled adhesives that are used for wind-turbine large-gap bonding applications.

Several Vectorply reinforcement materials were used to produce the laminate material and sandwich panels. Two of the three that were used, E-LT 2400-7P and E-LT 5500-10, are stitched (uncrimped – not woven) Biaxial E-glass fabrics specifically engineered for the wind-energy industry. A 12K 2 X 2 twill carbon fabric, TMGC 6003 by Airtech Advanced Materials Group, was also used in one of the panels. Table 10 summarizes the materials used in this effort.

Table 10 Summary of materials used to produce composite parts.

Part No.	Materials	Fiber	Thickness (in)	Areal Weight (oz/sq yd)	Density	Manufacturer
MGS RMR135/RIMH137	Epikote Resin	n/a	n/a	n/a	1.17 gm/cc^3	Hexion
E-LT 2400-7P	Stitched (noncrimped) Biaxial Fabric	E-Glass	0.027	23.74	n/a	Vectorply
E-LT 5500-10	Stitched (noncrimped) Biaxial Fabric	E-Glass	0.055	55.38	n/a	Vectorply
SXQ3600R1	Stitched Quadaxial Fabric	E-Glass	0.055	36.42	n/a	Fiberglass Industries
TMGC 6003	12K 2 x 2 Twill-Weave Fabric	Carbon	0.035	19	n/a	Airtech
C70.55	AirEX Urethane-Foam Core	n/a	1.0	n/a	4 lbs/ft^4	AirEX
I-Core EG	I-Core End-Grain Balsa-Wood Core	n/a	1.0	n/a	10 lbs/ft^4	I-Core

6.2.2 Production of GR900 Samples:

GR900 composite samples of each E-glass material (as listed in Table 10) were constructed for material characterization; a VARTM process produced flat-laminate material for these samples. The three primary methods for constructing wind-turbine blades are: a hand-built wet-layup process, a vacuum- or pressure-infusion process, and layering pre-impregnated (pre-preg) composite material. Hand layup and infusion are commonly used today, but as technology and materials have advanced, vacuum infusion has become the desired process. As pre-preg is still an emerging technology, laying up a wind blade with pre-preg material is less common.

The wet-layup process consists of building the composite by hand, layer by layer. After applying the reinforcement layer, a roller forces the resin into the fabric. Any excess resin is then squeegeed up. Wet layup is an economical fabrication method; however, this process results in fiber-schedule variability, varying material thickness, looser tolerances, rough internal-surface finishes, and higher final blade weights.

Both wet layup and VARTM processes have been used for wind energy applications. The VARTM process was chosen as the most appropriate method for producing representative wind-turbine blade materials. Wind-turbine blades produced using a vacuum-infusion process exhibit improved fiber volume, lower blade weight, improved internal surfaces (secondary bonding), and increased structural strength (due to the composite's higher fiber fractions achieved in the composite). Fabrication nuances that need to be considered during vacuum infusion include resin flow around corners, thorough wetting-out fabric when transitioning across different fiber volumes, and design review to reduce the potential for varying flow fronts.

The following VARTM processes were used for producing the flat laminates:

1. Mold preparation, material cut and layup
2. Building the VARTM setup and checking the bag for leaks
3. Resin preparation
4. Infusing the reinforcement
5. Curing the material

First, the aluminum caul plate was prepared and Frekote 700NC was applied as mold release. Then, all four flat laminate samples, consisting of 30 layers each, were manufactured using one infusion process. The reinforcement material for each laminate was precut to size and then weighed prior to infusion (see Figure 62). Four different resistive fabrics were embedded in one of the E-LT 5500-10 flat laminates. The resistive fabrics were loosely woven and are approximately .020" thick. These fabrics were located both one-ply deep and at the mid-plane of the laminate (see Figure 63).

Before starting infusion, each laminate stack was spaced about 1" apart from each other (see Figure 64). The tops of the individual stacks were covered with consumable vacuum infusion components - release fabric (tan) and flow media (orange). A resin inlet flow line constructed of nylon spiral wrap, release film, and flow media, was located on the left - close to the stacks. A nylon rope, acting as a resin dam is attached to the vacuum line exiting on the right. One vacuum bag encompassing everything was constructed, and a 15-30 minute leak check (18" Hg is achieved at a 5000 ft. elevation) was performed to identify any potential air leaks. Once a suitable leak-free vacuum was achieved, the Hexion resin system was mixed and degassed for 5 minutes (to remove any air entrained in the resin during the mixing process). Under constant vacuum the resin passed through the inlet line, flowed across, and impregnated the individual reinforcement stacks. Any excess resin accumulation was drawn down the rope dam and out to the paint pot (resin catch). Figure 65 shows the resin impregnating the material. The impregnation process took approximately 10 minutes; the exothermic crosslinking process for the resin completed after approximately one hour. Final cure was achieved at 140°F for 16 hours (material was moved to a walk in oven).

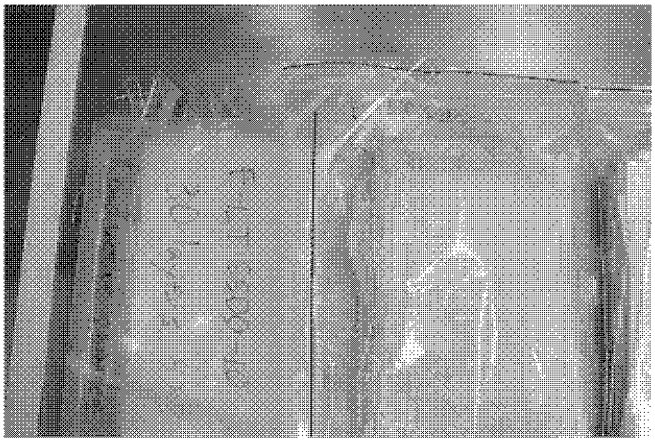

Figure 62 E-glass fiberglass fabric – cut and weighed.

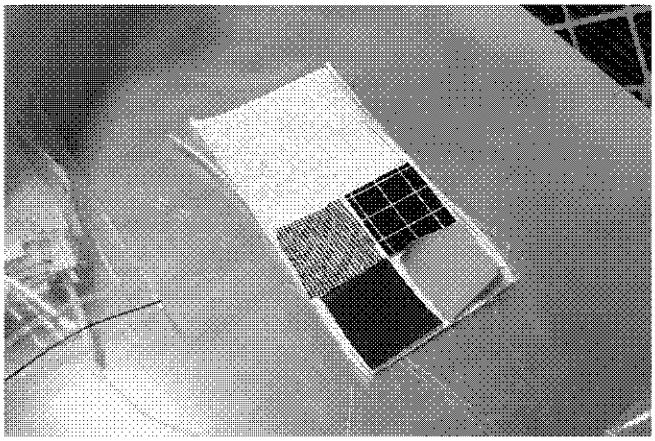

Figure 63 Locating resistive fabrics in fiberglass material.

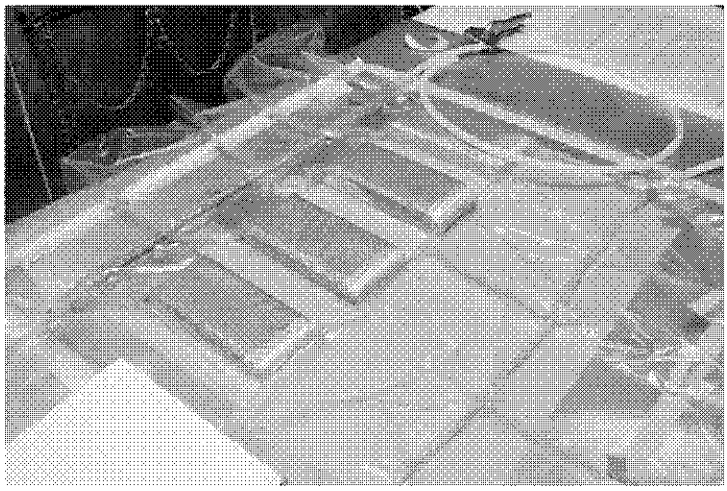

Figure 64 Fiberglass stacks vacuum bagged and leak checked.

Figure 65 Resin infusion of fiberglass material.

Table 11 Summary Table for GR900 Infused Laminate Material

Flat Laminate Material	Cured Laminate Material Height (in)	Weight of:		Fiber Fraction (%)
		Fiber Only (gm)	Cured Laminate (gm)	
E-LT 2400-7P	0.86	515	788	65.36
SXQ 3600-R1	1.20	780	1107	70.46
E-LT 5500-10	1.47	1136.3	1526	74.46
E-LT 550-10 (with resistive fabric)	1.50	1135.3	1524	74.49

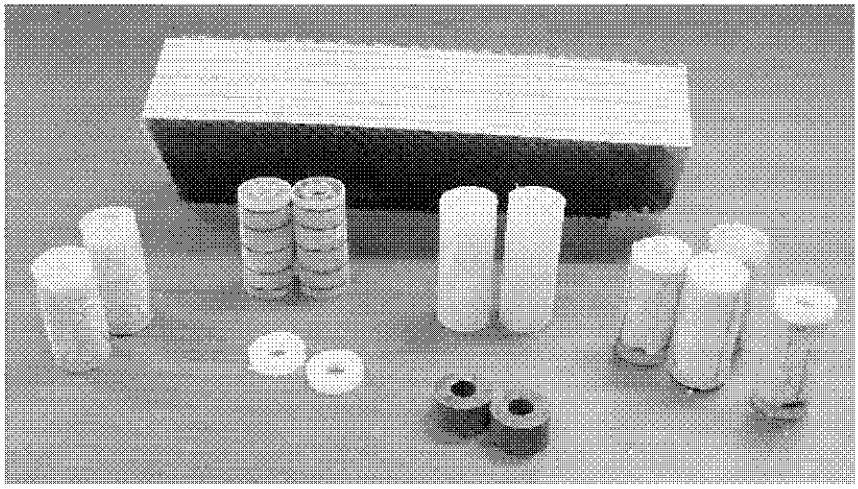

Figure 66 Fiberglass/carbon panel cross section and GR900 samples.

The resin infusion of the laminate material with embedded resistive fabrics was completed without difficulty. After infusion, the material was measured, weighed (see Table 11), and samples were machined to their final GR900 configurations. A visual review indicated that the embedded resistive fabrics wetted-out well and were completely integrated into laminate. Measurement of GR900 samples indicated most of the resistive fabrics fell within ±0.01 inches of the expected depth in the laminate material. No voids or delamination appeared as a result of embedding the resistive fabrics in the composite material. Integrating resistive fabrics in a glass-fiber composite material appeared to be a success; however if these materials are selected for future use, further investigation into appropriate 'sizing' (adhesive preparation) should be followed by material testing to prove that embedded materials do not affect mechanical strength. Figure 66 shows a variety of GR900 samples (glass only, balsa and foam core) and a cross section of the embedded carbon fabric in the glass sandwich panel.

6.2.3 Composite Panels:

Four composite panels were produced. The panel intent was to produce cross-sectional representations of the structural members exhibited in a typical 45-60 meter long wind-turbine blade (shear webs, skin reinforcements, and spar caps as shown in Figure 59). Two sandwich panels were produced to represent shear webs and skin reinforcements, and two glass composite panels were produced to represent spar caps. The panel design included a determination of the facesheet (skin) thickness and lay-up schedule as well as the core material and thickness. All panel materials are common to the wind-energy industry. The VARTM process used to make the panels was identical to the one used to make the GR900 laminate material, although the amount of resin and the infusion time differed based on core material.

Two sandwich panels were produced – one with foam core and one with balsa core. Figure 68 illustrates the balsa-core panel. Balsa- and foam-core materials are commonly used to produce a blade's shear web and as a reinforcement material in the blades outer facesheet (skin). The I-core balsa material was purchased already slotted and perforated. The urethane-foam core material on-hand was blank, so it was modified to match the existing design provided in the balsa material. Each facesheet (skin) for all of the sandwich panels consisted of 4 layers of E-LT 2400-7P laid up in a balanced +/- 45° orientation. All of the panels were built to the same specifications. See Figure 67 for a cross section of the panel's thickness dimensions. Figure 69 shows the balsa-core panel bagged and ready for infusion, and Figure 70 contains the infused balsa-core panel.

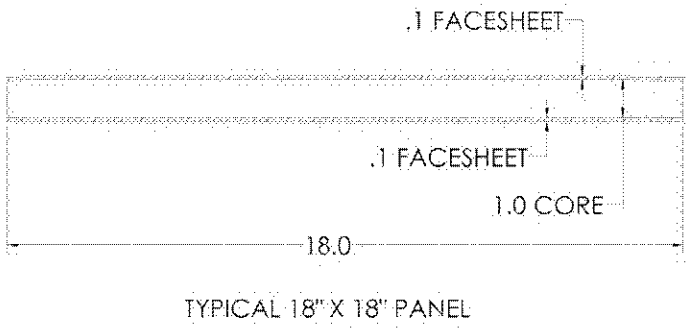

Figure 67 Typical sandwich panel cross-section.

Table 12 Summary Table for the Sandwich Panels

Panel No.	Represented Blade Member	Facesheet Material/Lay-up	Facesheet Thickness (in)	Core Material	Core Thickness (in)	Material Weight (gm)	Impregnated Panel Weight (gm)	Resin Content (%)
1	Skin Reinforcement or Shear Web	Each Skin – Vectorply 4 Plies E-LT-2400-7P	0.1	AirEX C70.55 4lb/ft^3 Urethane Foam	1.0	2097	3527	40.54%
2	Skin Reinforcement or Shear Web	Each Skin – Vectorply 4 Plies E-LT-2400-7P	0.1	I-Core EG 10lb/ft^3 End-Grain Balsa	1.0	1874.5	4551	58.81%
3	Spar Cap	Each Skin – Vectorply 4 Plies E-LT-2400-7P	0.1	25 Plies E-LT-5500-10 UNI orientation	1.0	12884	17482	26.30%
4	Other	Each Skin – Vectorply 4 Plies E-LT-2400-7P	0.1	25 Plies E-LT-5500-10 UNI with Carbon Interspersed with 5 plies Airtech TMGC 6003	1.0	10365	14338	27.71%

The third panel was fabricated with the intent it would be representative of a glass spar cap. A blade's spar cap is a principal load bearing structure composed of glass or carbon material laid up with the unidirectional direction. It was produced via a VARTM process in a manner similar to those explained previously. The fourth panel was fabricated with carbon fiber interspersed to represent a carbon spar cap. Table 12 provides detailed information on the infused resin panels.

There are challenges associated with any composite-infusion process, including race-tracking of the resin (low-flow-resistance channels or gaps in the bag that can prevent a controlled infusion of fabric), vacuum leaks in bag during panel infusion, and converging resin-flow fronts (resin fronts that when they converge can trap air pockets in the panel). These problems can be clearly identified as voids or resin starved areas in composite or sandwich panels. Preventative measures were taken during panel infusion, but some common challenges were encountered. A review of the VARTM-infusion technical issues was performed for process improvement in future VARTM infusion. After further analysis, panel setup adjustments (including using some release fabric underneath the panel and employing a peristaltic pump to control inlet resin flow) were implemented to avoid further issues.

Despite the challenges described above, the resin infusion of the sandwich and composite panels was completed without significant difficulty. A raw infused panel was weighed and cut to a final dimension of 18 inches by 18 inches. GR900 samples were produced from the excess panel material. GR900 samples demonstrated good adhesion between the laminate facesheets and the core material. Cross sections also demonstrate that even though the resin filled the core material voids (natural wood flaws), core materials did not saturate with resin. Measurement of a cross section of Panel #4 indicated that Airtech carbon fabric layers also fell within ±0.01 inches of the expected depth in the laminate material. No anomalies appeared as a result of embedding the carbon material in the glass material. Figure 71 shows the infused composite panels.

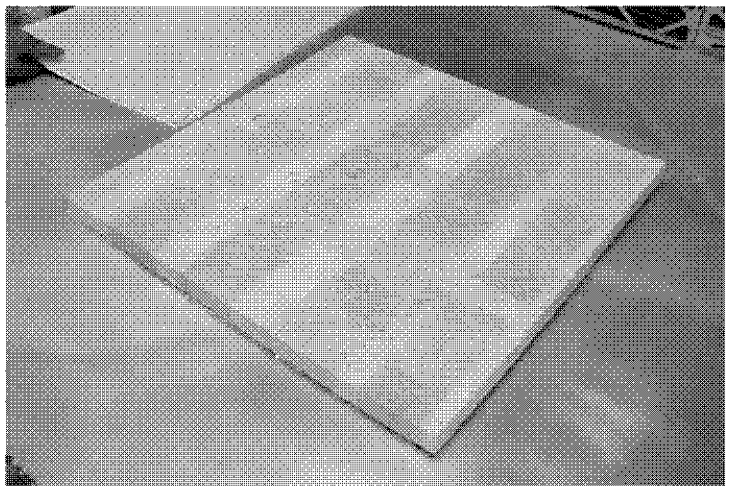

Figure 68 Initial layup of balsa-core sandwich panel.

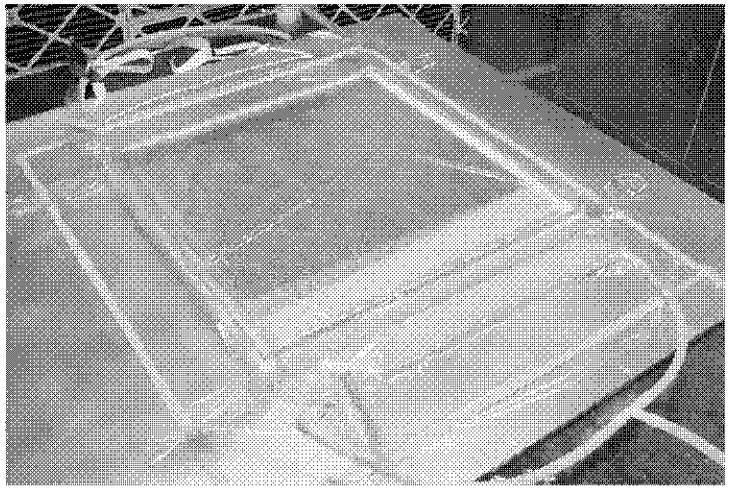

Figure 69 Balsa-core panel bagged and leak checked.

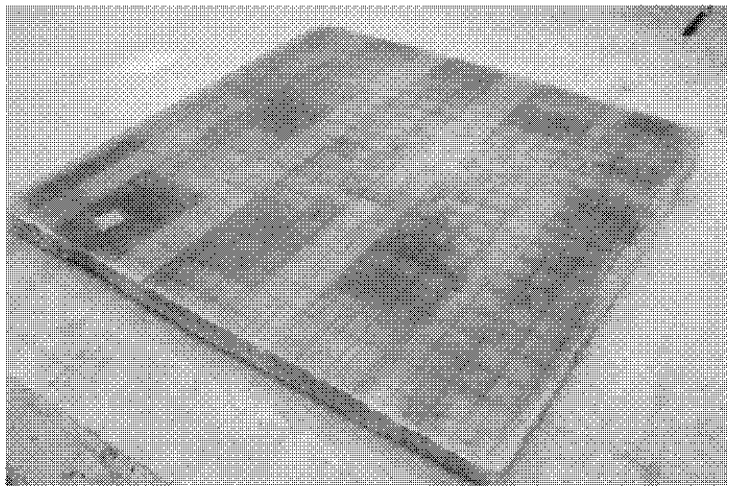

Figure 70 Unfinished balsa-core panel after infusion.

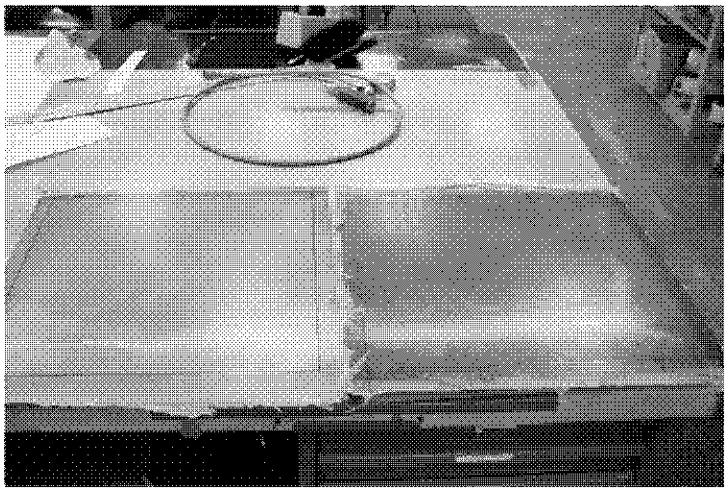

Figure 71 Glass-core panel (left) and glass-core with carbon-fabric interspersed panel (right).

6.2.4 Summary

Embedding resistive fabrics into E-glass composites was a success. The resistive fabrics selected wetted-out well and became an integral part of the material. Fabrics maintained a consistent depth and separation distance when infused, indicating that future treatments can be embedded and maintained in position within reasonable tolerances. Fabrication of sandwich and composite reference panels provided valuable experience in VARTM processes, and has identified techniques for future improvement, which should result in improved process control for both resin percentages and thickness tolerances.

7. Modeling the Radar Cross Section (RCS) of a Wind Turbine

The large wind turbines that are of current interest have rotor diameters that measure hundreds or even thousands of wavelengths at the radar frequency of interest. The computation of the radar cross section (RCS) for such large objects requires considerable computational resources in addition to appropriate approximations to the physics of the scattering process. It is an unfortunate fact that analysis of the electromagnetic scattering using full-wave solutions of Maxwell's equations, without any approximations, is not practical for objects of this size. However, useful approximate solutions are available through the physical-optics approximation [97, 98, 99] and through an extension called the shooting and bouncing ray (SBR) method [100, 101, 102, 103, 104]. Even so, significant computational resources are required to perform a thorough scattering analysis of a large wind turbine.

In the work described here, the computation of the RCS and Doppler spectrum is accomplished with the Xpatch code suite. Xpatch is an implementation of the SBR method, which is essentially an extension of the physical optics method. In the physical optics method, the object is illuminated with a plane wave, which can be represented by geometric-optics rays, and radiating currents are estimated from the tangential fields and boundary conditions at the surface. In the SBR method this approach is extended in that the traditional physical-optics currents (both electric and magnetic) are augmented with contributions from physical-optics currents associated with geometric-optics rays *scattered* from the structures. In this way, interactions between objects are included. This is important when modeling dielectric composite structures such as a turbine blade, since the radar signal can penetrate and reflect inside the structure before returning to the radar. This approach allows a greater degree of fidelity than would physical optics alone, while still allowing practical and accurate *estimation* of the fields associated with models which are very large when measured in terms of the wavelength. Additional discussion of physical optics, SBR, and Xpatch, including validation tests, can be found in [1].

7.1 Description of the Wind-Turbine Model

For the purposes of this study, the turbine is modeled as a set of three blades, without any other structures such as the hub, the nacelle, tower, etc. Thus, only the blades contribute to the computed radar cross section in the data presented below. Since the Doppler spectrum is of primary interest, it is appropriate to only model the moving rotor, as the stationary structures do not contribute to the Doppler shift. That will be the approach taken here. However, it is noted that these other components do contribute to the total radar cross section, and will increase the zero-Doppler (no Doppler shift) contribution to the scattered spectrum.

A single blade of the rotor model is shown in Figure 72. The length of the blade measured from the center of rotation is 63 m. On the right, the internal shear webs are just visible inside the open root. These internal components are modeled since the materials of the outer surface might be penetrable by the radar signal. However, no other internal materials, such as conductors for lightening protection, are modeled at this time. The three-blade rotor is shown in Figure 73. In this view, the operating rotor would turn clockwise, with the top blade moving toward the right.

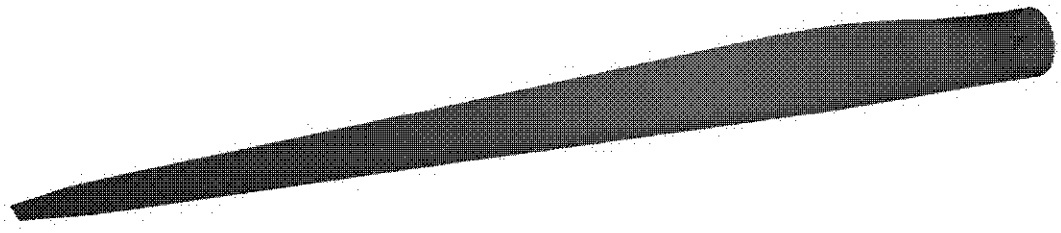

Figure 72 Illustration of the surface model of a single blade used in the wind-turbine model.

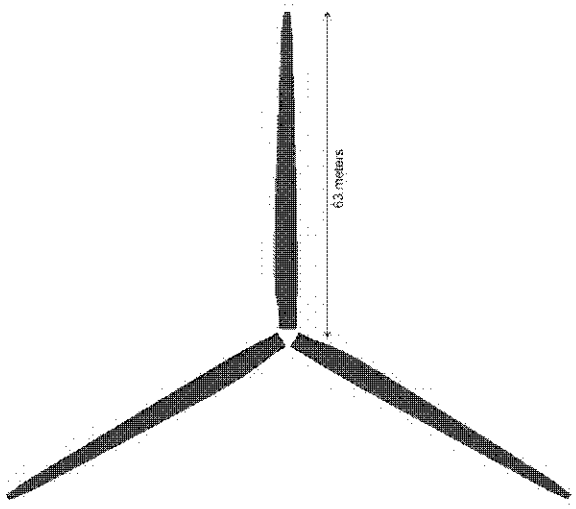

Figure 73 Front view of the three-blade rotor model.

The blades are modeled with typical fiber-composite construction, using both glass and carbon fiber materials. Fiberglass and low-density foam materials are sandwiched for blade panels where appropriate. A list of generic materials, with values for electrical properties used in the models, is contained in Table 13. The values of permittivity have been obtained from measurements of representative materials[1], except for the uniaxial carbon composite, which is modeled as described in Appendix II. The blade contains 67 different layered configurations, each comprised of 3 to 5 layers with various thicknesses, over a total of 546 different regions of the blade, giving it the appropriate mechanical properties. These range in thickness from about 10.5 cm at the

[1] The measurements were performed at Sandia National Laboratories, using GR-900 coaxial air-line to hold the samples.

root to about 0.6 cm at the tip. The thicknesses of the stacks are plotted in ascending order in Figure 74, where the abscissa is labeled with the material-stack index number. The entirety of this diversity of material configurations is contained in the computational model, unless stated otherwise. To evaluate how these various stacks respond to the radar, the computed radar cross section of a square plate of each material, measuring 1 m on each side, is plotted relative to that of an identically sized plate consisting of perfect electrical conductor (PEC) in Figure 75, for normal incidence at $f = 2.8$ GHz. The abscissa is labeled with the index number of each layered stack, as the data are ordered from lowest to highest response.

Some of the layered stacks exhibit very low RCS compared to that from the perfect electric conductor. However, this should not be mistaken for evidence of the presence of radar-absorbing materials. None of these layered configurations qualify in any way as radar-absorbing material; the low-reflections are in fact evidence of some level of transparency. Thus, it is critical to model the internal structure of the blade, because portions of the internal structure will be illuminated by the microwave signal passing through the outer shell. It should also be obvious that modeling the blade with a perfect electrical conductor on the surface is inappropriate. In fact, evidence will be presented below that shows that the internal shear web structure can be an important contributor to the total radar cross section of the blade. While the internal shear web structure is the only internal structure included in this model, other internal structures, including lightning-protection conductors, should be included. It will also be demonstrated that modeling the blade as PEC can actually lead to erroneous conclusions about the RCS response, a subtle conclusion that one might not suspect after only cursory thought.

Table 13 List of materials and electrical properties used in turbine-blade models.

material	permittivity	permeability
PEC (perfect electric conductor)	n/a	n/a
Gelcoat	2.88 –*j* 0.086	1.0 –*j* 0.0
Unidirectional glass composite	4.5 –*j* 0.068	1.0 –*j* 0.0
Double bias glass composite	4.0 –*j* 0.08	1.0 –*j* 0.0
Foam	1.15 –*j* 0.009	1.0 –*j* 0.0
Triaxial glass composite	4.35 –*j* 0.087	1.0 –*j* 0.0
Uniaxial carbon composite	800 –*j* 809	1.0 –*j* 0.0
Foam	1.15 –*j* 0.009	1.0 –*j* 0.0

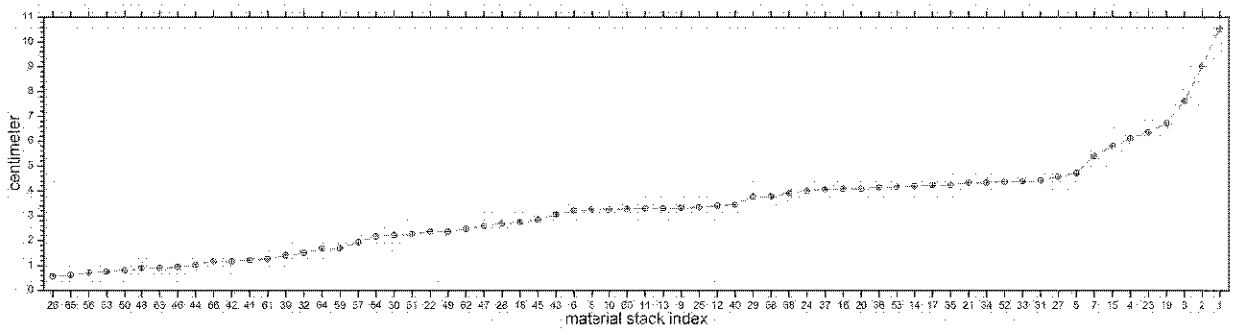

Figure 74 Thickness of material stacks, with abscissa labeled by index number.

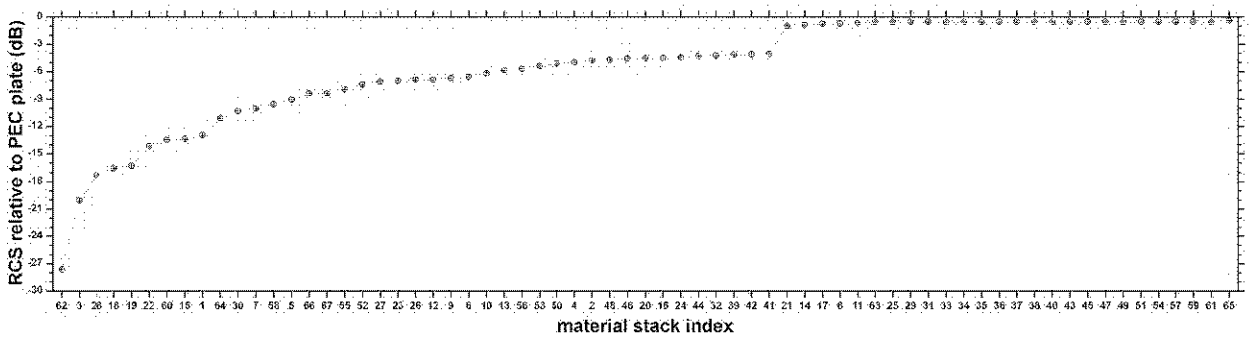

Figure 75 RCS at normal incidence for a 1-m by 1-m flat plate made of the layered material stacks relative to a PEC plate, at $f = 2.8$ GHz. The abscissa is labeled with the index number of each stack.

7.2 Static Radar Cross Section of a Wind Turbine

The static radar cross section refers to the radar response of a target when there is no relative motion between the radar and the target, while dynamic RCS refers to the time-varying response resulting from relative motion, and is related to the Doppler spectrum. In Figure 76, the computed static RCS of the fiber-composite wind turbine described above is plotted as a function of azimuth, when the elevation angle is zero. The radar frequency is 2.8 GHz, and the rotor is oriented with one blade in the vertical position, as illustrated in Figure 77, and of course, the rotor is not moving. The computed RCS of the identically shaped PEC rotor is plotted on top of the RCS from the fiber-composite model in Figure 78, for ease of comparison. It is interesting to see that the PEC rotor has a larger RCS at most, *but not all,* azimuth angles. One might assume that a PEC rotor would represent a worst-case model, and while the data in Figure 78 might be construed as supporting evidence, it will be shown below, in the section titled *Computation of the Doppler Signature*, that this assumption is not entirely accurate and can lead to ill-formed conclusions. In fact, at azimuth angles that produce some of the highest Doppler shifts, around 90° and 270° for example, the fiber-composite rotor exhibits a larger static RCS.

The response for two linear polarizations are shown; HH indicates that the electric field vector (both transmit and receive) is both normal to the vector locating the radar and lies in a plane containing both the axis of rotation and the vector locating the radar , while VV indicates that the electric-field vectors are normal to that plane. When the elevation is zero, HH indicates that the electric-field vectors lie in the horizon plane ($\hat{\mathbf{x}}$ - $\hat{\mathbf{y}}$ plane in Figure 77), and VV indicates that the electric-field vectors are parallel to $\hat{\mathbf{z}}$ in Figure 77 (vertical). Each polar plot shows the RCS response for the indicated polarization when the radar is located at a set of points on a circle around the turbine, while it remains at zero elevation. The two rectangular plots show the variation in RCS in a small region near the azimuth directions of 0° and 180°, with both polarizations plotted on the same axes. Because of the large extent of the rotor in the $\hat{\mathbf{x}}$ - $\hat{\mathbf{z}}$ plane (measured in wavelengths), not only does the largest RCS occur in these two regions, but the RCS changes very rapidly with azimuth; the amplitude changes by several decibels with as little as 0.02° change in azimuth. The variation with azimuth is not as extreme near 90° and 270°. The variation between the responses of the two linear polarizations is minimal. To capture the detail contained in the RCS signature for this rotor, the azimuthal increment for the computation was 0.0275°, resulting in over 13,000 angles being examined.[2] Computation of Doppler spectra at each of these angles will likely prove impractical, so the static-RCS computation will be a useful tool to help decide for how many and for which azimuth angles the Doppler spectra should be computed.

This rotor is quite large, with a diameter of 126 m, resulting in the computed peak RCS of 52 dBsm (decibels with respect to a square meter). To put this into perspective, the median RCS of a Boeing 737 aircraft at nose aspect at this frequency is about 10 dBsm. For the Boeing 747, this would increase to about 18 dBsm [105].

[2] The computation was performed by dividing it between 20 threads running on a dual hex-core Intel® Xeon® x5690 CPU with a clock rate of 3.47 GHz, and required the equivalent of $144^{d}\,16^{h}22^{m}38^{s}$ of total CPU time.

Although these single-number comparisons are interesting, it cannot be emphasized enough that a single number is a very poor method of characterizing a complex radar target. However, static RCS plots like Figure 76 are useful, when used with other considerations, for choosing appropriate azimuth locations for computing the dynamic RCS and the associated Doppler spectrum.

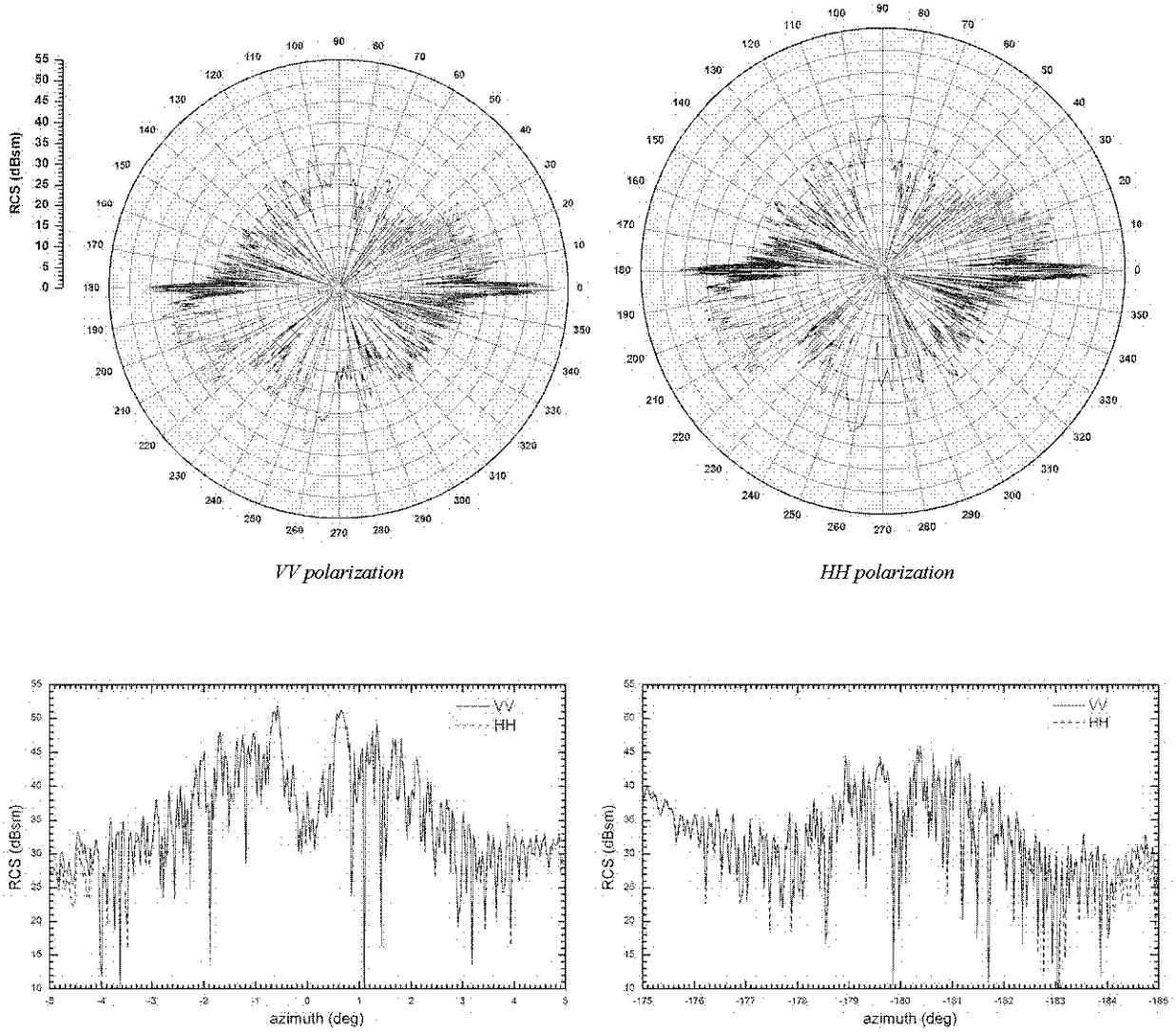

VV polarization *HH polarization*

Figure 76 RCS vs. azimuth of the untreated 3-blade rotor, computed at f = 2.8 GHz and 0° elevation with materials as described in the text.

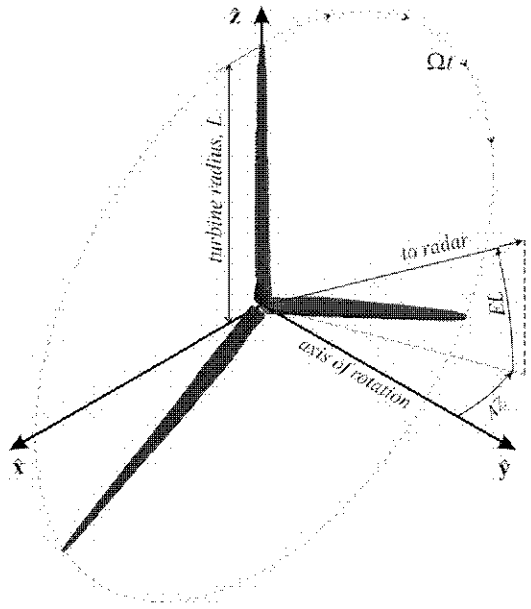

Figure 77 Three-blade rotor model with coordinate system and direction to radar.

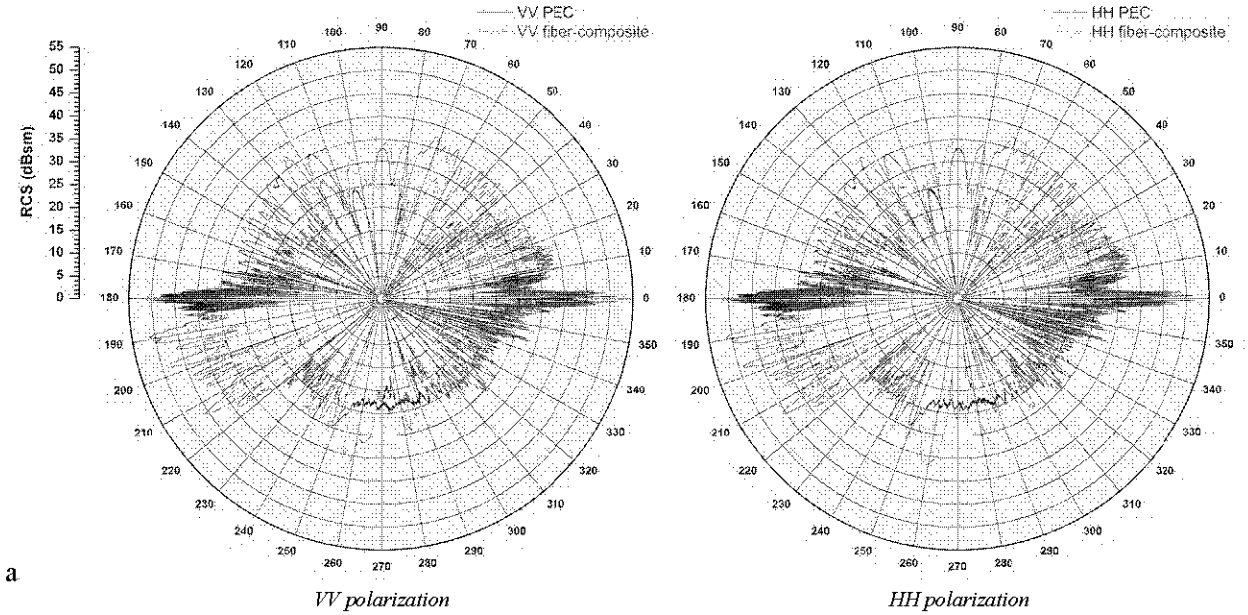

a

Figure 78 RCS vs. azimuth of the PEC 3-blade rotor (blue) compared with the RCS of the fiber-composite rotor (red), computed at $f = 2.8$ GHz and 0° elevation.

7.3 Sampling Considerations for the Computation of Doppler signature

When the rotor is illuminated by a radar signal, the scattered signal will be shifted in frequency as a result of the Doppler effect [1, 105, 106]. The Doppler shift is caused by the motion of the blade toward or away from the radar, and the process is described in considerable detail in Appendix I of reference [1]. To avoid aliasing of the Doppler frequencies, a phenomenon whereby the higher frequencies are mistaken for lower frequencies, the radar must sample the scattered signal at a rate greater than the Nyquist rate [107, 108]. Nyquist sampling requires more than two samples per period of the highest Doppler shift present in the scattered signal. As will be shown below, this requires that the modeling computation provide estimates of the amplitude and phase of the signal at appropriate angular increments, such that no portion of the blade moves toward or away from the radar by a distance greater or equal to a quarter of the radar's wavelength between two consecutive samples.

Because the angular-sampling increment is such a critical parameter for properly computing Doppler spectra, it will be derived here. Consider a radar located in the direction of the unit vector $\hat{\mathbf{r}}_{radar}$ from an object moving with velocity $\vec{\mathbf{v}}$, so the velocity toward the radar is $\vec{\mathbf{v}} \cdot \hat{\mathbf{r}}_{radar}$, and the Doppler shift is [106]

$$\Delta f_{Doppler} = f_0 \frac{2\vec{\mathbf{v}} \cdot \hat{\mathbf{r}}_{radar}}{c}, \tag{6.1}$$

where f_0 is the radar frequency in Hz, and c is the speed of light[3]. The factor of two in eqn. (6.1) accounts for the effect of the two-way propagation from the radar to the object and back to the radar. To adequately measure the Doppler spectrum, the radar must sample the scattered signal at a frequency greater than twice the maximum Doppler shift,

$$f_{sample} > 2\left|\Delta f_{Doppler}\right|_{maximum} = \frac{4f_0}{c}\left|\vec{\mathbf{v}} \cdot \hat{\mathbf{r}}_{radar}\right|_{maximum} = \frac{4}{\lambda}\left|\vec{\mathbf{v}} \cdot \hat{\mathbf{r}}_{radar}\right|_{maximum}. \tag{6.2}$$

where the wave length of the radar signal is $\lambda = c/f_0$.

Because the tips of the blades in a rotating turbine have the highest velocity of any point on the rotor, it is necessary to only consider the motion of the blade tips. With reference to Figure 77, the unit vector pointing to the radar is

$$\hat{\mathbf{r}}_{radar} = -\hat{\mathbf{x}}\cos(EL)\sin(AZ) + \hat{\mathbf{y}}\cos(EL)\cos(AZ) + \hat{\mathbf{z}}\sin(EL). \tag{6.3}$$

The tips of a 3-blade rotor are located at

$$\begin{aligned}
\vec{\mathbf{r}}_1 &= L\left[-\hat{\mathbf{x}}\sin(\Omega t) + \hat{\mathbf{z}}\cos(\Omega t)\right], \\
\vec{\mathbf{r}}_2 &= L\left[-\hat{\mathbf{x}}\sin\left(\Omega t + \tfrac{2}{3}\pi\right) + \hat{\mathbf{z}}\cos\left(\Omega t + \tfrac{2}{3}\pi\right)\right], \text{ and} \\
\vec{\mathbf{r}}_3 &= L\left[-\hat{\mathbf{x}}\sin\left(\Omega t - \tfrac{2}{3}\pi\right) + \hat{\mathbf{z}}\cos\left(\Omega t - \tfrac{2}{3}\pi\right)\right].
\end{aligned} \tag{6.4}$$

where L is the length of the blade from the center of rotation to the tip, and Ω is the rotation frequency measured in radians per second. The time reference is chosen so that at $t = 0$ s, blade 1 will be vertical (along $\hat{\mathbf{z}}$ in Figure 77). The velocity of each tip is given by

$$\begin{aligned}
\vec{\mathbf{v}}_1 &= \frac{\partial}{\partial t}\vec{\mathbf{r}}_1 = -\Omega L\left[\hat{\mathbf{x}}\cos(\Omega t) + \hat{\mathbf{z}}\sin(\Omega t)\right], \\
\vec{\mathbf{v}}_2 &= \frac{\partial}{\partial t}\vec{\mathbf{r}}_2 = -\Omega L\left[\hat{\mathbf{x}}\cos\left(\Omega t + \tfrac{2}{3}\pi\right) + \hat{\mathbf{z}}\sin\left(\Omega t + \tfrac{2}{3}\pi\right)\right], \text{ and} \\
\vec{\mathbf{v}}_3 &= \frac{\partial}{\partial t}\vec{\mathbf{r}}_3 = -\Omega L\left[\hat{\mathbf{x}}\cos\left(\Omega t - \tfrac{2}{3}\pi\right) + \hat{\mathbf{z}}\sin\left(\Omega t - \tfrac{2}{3}\pi\right)\right].
\end{aligned} \tag{6.5}$$

During the time interval from t_1 to t_2, the blade tips move a vector distance

$$\begin{aligned}
\vec{\mathbf{s}}_1 &= \int_{t_1}^{t_2} \vec{\mathbf{v}}_1 dt = L\left(-\hat{\mathbf{x}}\left[\sin(\Omega t_2) - \sin(\Omega t_1)\right] + \hat{\mathbf{z}}\left[\cos(\Omega t_2) - \cos(\Omega t_1)\right]\right), \\
\vec{\mathbf{s}}_2 &= \int_{t_1}^{t_2} \vec{\mathbf{v}}_2 dt = L\left(-\hat{\mathbf{x}}\left[\sin\left(\Omega t_2 + \tfrac{2}{3}\pi\right) - \sin\left(\Omega t_1 + \tfrac{2}{3}\pi\right)\right] + \hat{\mathbf{z}}\left[\cos\left(\Omega t_2 + \tfrac{2}{3}\pi\right) - \cos\left(\Omega t_1 + \tfrac{2}{3}\pi\right)\right]\right), \text{ and} \\
\vec{\mathbf{s}}_3 &= \int_{t_1}^{t_2} \vec{\mathbf{v}}_3 dt = L\left(-\hat{\mathbf{x}}\left[\sin\left(\Omega t_2 - \tfrac{2}{3}\pi\right) - \sin\left(\Omega t_1 - \tfrac{2}{3}\pi\right)\right] + \hat{\mathbf{z}}\left[\cos\left(\Omega t_2 - \tfrac{2}{3}\pi\right) - \cos\left(\Omega t_1 - \tfrac{2}{3}\pi\right)\right]\right).
\end{aligned} \tag{6.6}$$

---

[3] The *exact* speed of light in the vacuum is $c = 2.99792458 \cdot 10^8$ m/s, which is ultimately used to define the standard length of the meter. The speed of light in air is slower by about 0.03% to 0.05%, depending on temperature and water-vapor content.

The changes in the radar frequency due to the Doppler effect from scattering at the tips of the blades are

$$\Delta f_1 = \frac{2f_0}{c}\Omega L\left[\cos(\Omega t)\cos(EL)\sin(AZ) - \sin(\Omega t)\sin(EL)\right],$$
$$\Delta f_2 = \frac{2f_0}{c}\Omega L\left[\cos\left(\Omega t + \tfrac{2}{3}\pi\right)\cos(EL)\sin(AZ) - \sin\left(\Omega t + \tfrac{2}{3}\pi\right)\sin(EL)\right], \text{ and} \quad (6.7)$$
$$\Delta f_3 = \frac{2f_0}{c}\Omega L\left[\cos\left(\Omega t + \tfrac{2}{3}\pi\right)\cos(EL)\sin(AZ) - \sin\left(\Omega t + \tfrac{2}{3}\pi\right)\sin(EL)\right].$$

It is obvious that the frequencies associated with the blade tips are not constant as the blade rotates; the Doppler shifts vary with time, and the maximum frequency shifts associated with each tip occur at different times. The peak Doppler frequency contained in the total spectrum, for a specified radar direction, is

$$\Delta f_{peak} = \frac{2f_0 L\Omega}{c}\sqrt{\cos^2(EL)\sin^2(AZ) + \sin^2(EL)}\,. \quad (6.8)$$

The time-variation of the Doppler shifts in (6.7) suggests the need for examining not just the total spectrum (all Doppler shifts produced during a rotation period), but also the spectrogram (the time-dependent spectra that occur at different times during the rotation period).

The maximum Doppler frequency occurs when the directions of the velocity and the radar-position vectors coincide, so from (6.2) and (6.8), the minimum sample frequency can be obtained,

$$f_{sample} > f_{Nyquist} = 2\Delta f_{peak} = \frac{8\pi L}{\lambda} f_\Omega \sqrt{\cos^2(EL)\sin^2(AZ) + \sin^2(EL)}\,, \quad (6.9)$$

where $f_\Omega = \Omega/2\pi$ is the rotation frequency in rotations per second. Between samples, the rotor will move through an angle $\delta\alpha_{sample}$ given by

$$\delta\alpha_{sample} = 2\pi\frac{f_\Omega}{f_{sample}} < \frac{\lambda}{4L}\frac{1}{\sqrt{\cos^2(EL)\sin^2(AZ) + \sin^2(EL)}}. \quad (6.10)$$

If the radar is located a substantial distance away on the $\hat{\mathbf{x}}$ axis, then the tip of the blade moves a distance toward the radar given by,

$$\mathbf{s}_1 \cdot (-\hat{\mathbf{x}}) = L\sin\left(\frac{2\pi f_\Omega}{f_{sample}}\right) \le L\sin\left(\frac{\lambda}{4L}\right) \quad (6.11)$$

during the sampling interval $0 \le t \le 1/f_{sample}$. If the sample frequency is exactly the Nyquist rate (use the equal sign instead of the inequality), then the tip moves a quarter of a wavelength toward the radar during the sample interval, but the difference in the path length traversed by the radar signal from the beginning of the sample interval to the end would be a half wavelength, giving two samples per signal wavelength. To avoid aliasing, the sampling frequency must slightly exceed the Nyquist frequency, so the actual distance the tip moves toward the radar between samples must be less than a quarter of a wavelength. Table 14 shows the maximum sample interval and minimum number of samples required in a 120° arc of rotation to avoid aliasing of the Doppler shift for several frequencies and two blade lengths. As can be seen from the entries in the table, a very large number of samples will be required to avoid aliasing.

Uniformly spaced samples are needed for efficient computation of the Doppler spectrum from time-domain data, since a standard fast-Fourier-transform algorithm will be used. That is reflected in the numbers contained in Table 14. However, the analysis above can be generalized to show that all points on the rotor are required to move less than a quarter of a wavelength toward or away from the radar between two adjacent samples to avoid aliasing of the Doppler frequencies, and this fact can be utilized to reduce the number of RCS computations required. This is accomplished by appropriately choosing non-uniformly spaced points in the rotation for the

computation, such that no adjacent sample points are separated by more than one quarter wavelength, measured toward the radar. Subsequently, the requirement for evenly spaced points for the spectrum computation can be satisfied with interpolation between these non-uniformly spaced points. While greater effort is required to set up the RCS computation, a significant reduction in required CPU time is anticipated.

Table 14 Doppler-sample considerations for rotating turbine at selected radar frequencies.

band	frequency (GHz)	λ (cm)	sampling requirement for no aliased Doppler components			
			angular interval (degree)		minimum samples in 120° span	
			45-m blade	63-m blade	45-m blade	63-m blade
L	1.3	23.06	0.0734	0.0524	1,635	2,289
S	2.8	10.71	0.0341	0.0243	3,522	4,930
C	5.925	5.06	0.0161	0.0115	7,451	10,432
X	9.5	3.16	0.0100	0.0072	11,947	16,725

7.4 Computation of the Doppler Signature

The radar cross section of the wind turbine varies with time as the rotor moves. It also varies with the direction of the radar with respect to the axis of rotation. The time-variation is very rapid when the diameter of the rotor comprises many wavelengths of the radar signal. For example, Figure 79 shows the RCS vs. time for the 126-m diameter rotor, rotating at $\Omega = 12.1$ rpm, when the radar is located at $AZ = 90°$, $EL = 0°$ and is operating at $f = 2.8$ GHz (S-band). At this frequency, the rotor measures just fewer than 1,177 wavelengths in diameter, and so qualifies as electromagnetically very large. The rapid time variation gives rise to significant Doppler modulation as it rotates. The time span of 200 ms depicted in Figure 79 represents a rotation of $\pm 7.3°$ about the reference position, where one blade is vertical. The blade tips are moving at a speed of more than 178 mph, and the maximum Doppler shift is just over 1.49 KHz.

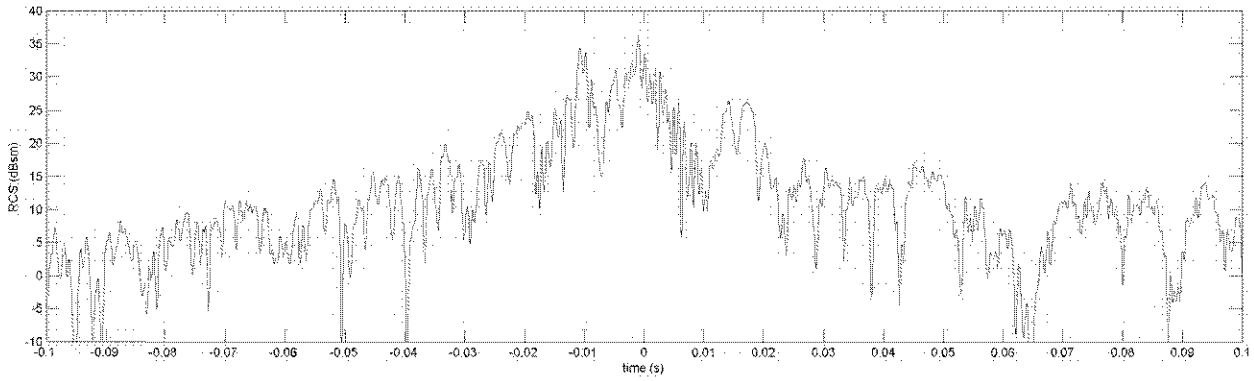

Figure 79 Computed radar cross section (VV polarization) for the 126-m diameter rotor as a function of time at frequency f = 2.8 GHz. The rotation rate is 12.1 rpm, and the plotted time corresponds to 4% of one rotation, ±7.3° from the reference position at t = 0 s, when one blade is vertical.

It should be noted in this example that the RCS can change by several decibels in the span of as little as 0.02° of rotation. Unfortunately, because of its rapid angular variations, the RCS of a turbine cannot be accurately described with a single number or even a few simple numbers. One could take the maximum RCS over all angles, rotations, and polarizations as a single-number measure, but because of the size of a wind-turbine system, the computation of this single value is an immense task. In an effort to simplify the description of the RCS response, the value of the time-averaged RCS over one rotation period, T, with the located radar at a

specified azimuth and elevation with respect to the axis of rotation, might be considered a potentially useful single-number measure of the RCS,

$$\sigma_{avg}(Az,El)=\frac{1}{T}\int_{-T/2}^{T/2}\sigma(t,AZ,EL)\,dt\,. \tag{6.12}$$

Ignoring the limitation that this measure is a function of the direction to the radar, and that it will vary considerably as that direction is varied, it is still not an entirely adequate description of the RCS signature of a wind turbine, either. However, while the maximum RCS or the time-averaged RCS have some limited value, plotting the computed RCS as a function of time can also be more useful. More useful still is the Doppler spectrum.

It is important to understand that the Doppler spectrum is the quantity of most interest when evaluating the potential for radar interference by wind turbines. The time-domain response and the spectral response are related through the Fourier transform, allowing the spectrum to be computed easily from the time-domain response. This spectral data can be presented in two useful formats. The first, called the total spectrum, is the Fourier transform of the time variation over one complete rotation period. The second, called a spectrogram, is obtained by applying the Fourier transform to a narrow time window, Δt, and moving the window through time within a rotation period, yielding an estimate of the spectrum as a function of time.

Let $\gamma(t)$ represent the complex phasor form of the scattered signal in the time domain. The total spectrum is

$$S_{total}(f_{Doppler})=\left|s_{total}(f_{Doppler})\right|^2,\ \text{where}\ s_{total}(f_{Doppler})=\int_{-T/2}^{T/2}\gamma(\tau)e^{-j2\pi f_{Doppler}\tau}d\tau, \tag{6.13}$$

and the spectrogram is

$$S(t,f_{Doppler})=\left|s(t,f_{Doppler})\right|^2,\ \text{where}\ s(t,f_{Doppler})=\int_{\Delta t/2}^{\Delta t/2}\gamma(t+\tau)e^{-j2\pi f_{Doppler}(t+\tau)}d\tau, \tag{6.14}$$

with $\Delta t \ll T$, $-T/2<t<T/2$, and T is the period of rotation. The frequency resolution of the total spectrum is considerably greater than that of the spectrogram. However, the spectrogram shows the variation in the spectral content as a function of time, while the total spectrum show the amplitude of all the frequencies that will be produced at some time during a rotation of the blades. In the context of this analysis, the scattered time-domain signal, $\gamma(t)$, is defined to have units of length, so the radar cross section is given by $\sigma=|\gamma|^2$, and the magnitude of the spectrum will be measured in m^2s^2 or m^2/Hz^2.

The total spectrum shows all of the Doppler-frequency components that will occur during a complete rotation of the blades. On the other hand, the spectrogram shows the spectrum as a function of time, giving the Doppler-frequency components present at a particular time during the rotation. However, as is obvious from (6.14), the spectrogram at a particular time t requires integration of contributions in a small time window surrounding t. As is always the case when two quantities are related through a Fourier transform, this integration over a span of time introduces an uncertainty principle. In this case, the uncertainty results in a compromise between the resolution of the spectral components and the precision of the knowledge of exactly when they occur. Large values of Δt provide greater resolution of the spectral components, but provide less certainty regarding when they occur. Similarly, small values of Δt smear the spectral components together, providing low-resolution spectra, but increasing the certainty about the time that they occur. The total spectrum provides the greatest spectral resolution, but introduces the greatest uncertainty, since it is only known that a given spectral component occurs *sometime* during the entire period T. While the total spectrum will be presented here as a continuous function, in reality it consists of a line spectrum, with the lines spaced by $\Delta f=1/T$, as a result of the periodic rotation. For a rotation rate of 12.1 rpm, which is the maximum rotation rate for the 126-m diameter rotor modeled here, the line spacing is $\Delta f=0.2$ Hz. Examples of the total spectrum and the spectrogram are illustrated in Figure 80.

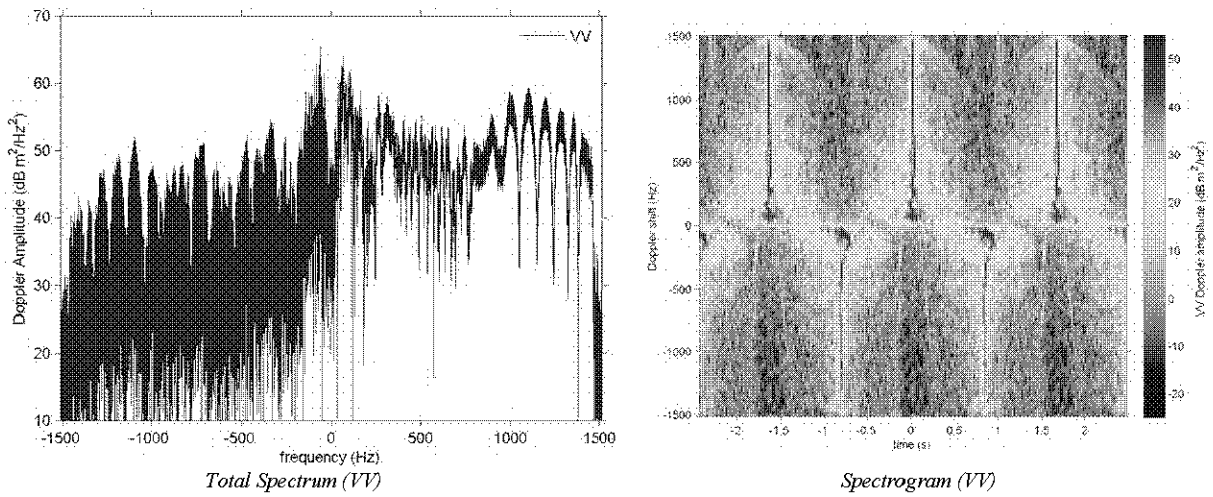

Total Spectrum (VV) *Spectrogram (VV)*

Figure 80 *The total spectrum and spectrogram of the scattering from the untreated fiber-composite 3-blade rotor, computed at $f = 2.8$ GHz, with materials as described in the text (VV polarization). A portion of the time-domain response is illustrated in Figure 79.*

It seems to be a somewhat common practice to model the RCS of wind turbines with the assumption that the blades are made of a perfect electrical conductor (PEC). While this would appear to be unrealistic since the blades are made of fiber composites, it might be assumed that it provides a worst-case (maximum scattering effect) situation. Unfortunately, that is not the case. To see this, and to see how misleading conclusions can be drawn, consider the situation with the radar located at $AZ = 90°, EL = 0°$ (see Figure 77 for reference). The time-averaged RCS of the untreated composite rotor is 6.1 dBsm for VV polarization and 6.6 dBsm for HH polarization. For the PEC rotor, the time-averaged RCS values are 8.1 dBsm for VV polarization and 8.2 dBsm for HH polarization. Clearly, the PEC rotor, when viewed at this aspect, has slightly larger average radar cross section than the composite rotor, and this might be construed as evidence in support of the (mistaken) idea that a PEC model represents the worst case. However, the Doppler spectrum, as noted above, is a critical contributor to the negative effect on the radar, and the PEC rotor produces a much *weaker* Doppler spectrum at large Doppler shifts than does the composite rotor. This is easily seen in Figure 81, where the total spectrum for each of the rotors is plotted. At many of the higher Doppler frequencies, the PEC rotor produces about 20 dB lower signal than the fiber-composite rotor. Although the time-averaged RCS number implies that the PEC rotor might represent a worst-case model, the high-frequency components of the Doppler spectrum of the fiber-composite rotor are actually much stronger than the corresponding components of the spectrum from the PEC rotor. In this case, the time-averaged RCS is misleading. Although the computation for the PEC rotor is considerably more efficient than for the complete fiber-composite model[4], it is *not* recommended that the PEC model be used because of its potential to cause misleading conclusions.

[4] The total time to compute the Doppler spectrum for the fiber-composite blade in Figure 81 was $35^{d}\ 21^{h}\ 14^{m}\ 38.7^{s}$, while for the PEC rotor, the total time was $3^{d}\ 21^{h}\ 1^{m}\ 10.6^{s}$. These times reflect CPU time for a single thread running on a single core of an Intel® Xeon® x5690 CPU running at a clock rate of 3.47 GHz.

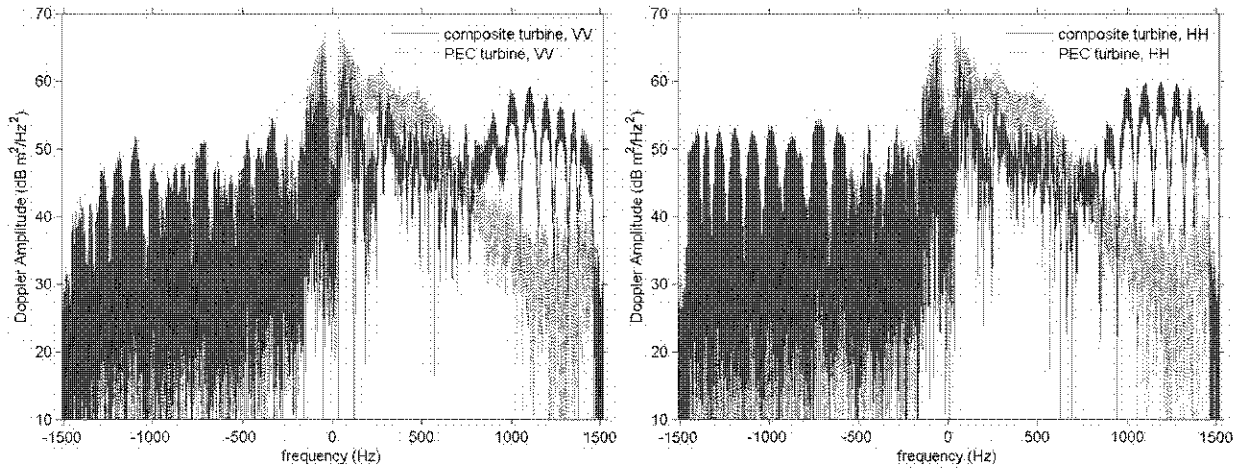

Figure 81 *Comparison of the total spectrum, computed at $f = 2.8$ GHz, for the fiber-composite rotor (red) and the PEC rotor (blue), with VV polarization on the left and HH polarization on the right. The radar is located at azimuth 90° and elevation 0°. The Doppler spectrum of the PEC rotor has considerably lower amplitude than that of the composite rotor.*

7.4.1 Characterization of the RCS Response of Different Turbine Configurations

The RCS response will be characterized by time-domain response, total spectrum, and spectrograms for VV and HH polarizations. These are shown for several rotor configurations in Figure 82 through Figure 94. In each case, the radar is operating at $f = 2.8$ GHz. For Figure 82 through Figure 87, the radar is located at $AZ = 90°, EL = 0°$ (referenced to the coordinate system in Figure 77). In Figure 88 through Figure 94, the radar is located at $AZ = 0.65°, EL = -3.0°$. In all cases, the rotor is turning clockwise at 12.1 rpm, so that the top blade is approaching the radar with its leading edge. The time reference is chosen so one blade is vertical when $t = 0$ s.

In addition to comparing the RCS performance of the PEC model with the performance of the dielectric fiber-composite model, other comparisons will be made. As previously noted, there are 67 different layered configurations of materials used in the blade construction. Some of these consist entirely of layers of different fiberglass materials, while others combine fiberglass and carbon-fiber composites. A third class consists of a thick section of low-density foam sandwiched between two thin layers of fiberglass. While there is considerable variation between members of these classes, the division into three classes is useful. With the data presented below, comparisons will be made between the RCS responses obtained when one or more of these classes are replaced with *perfect* absorber. In the context of the SBR method used to model the radar scattering, a perfect absorber is totally black; when an incident ray encounters a perfect absorber, no reflected or transmitted rays are generated, and no physical-optics currents are placed on its surface. Thus, the perfect absorber is truly black, and contributes nothing to the scattered field.

7.4.1.1 Radar Located at $AZ = 90°, EL = 0°$

The RCS characterization for the baseline rotor, modeled with the fiber-composite materials as described above, is shown in Figure 82 when the radar is located at $AZ = 90°, EL = 0°$. The time-domain response shows peaks of about 36 dBsm when a blade is oriented vertically upward, and rotating toward the radar, at times $t = 0$ s and $t = \pm 1.65$ s. The sharp peaks at $t = \pm 0.83$ s are from the trailing edge of each blade when it is oriented vertically downward, rotating away from the radar. With the radar in this location, the broadly rounded leading edge of the blade is moving toward the radar, while the sharp trailing edge recedes from the radar. This causes the asymmetry between the positive and negative Doppler components, as evidenced by the total spectrum plots. The positive (up) Doppler dominates the spectrum slightly. The spectrograms clearly show the bright flashes when a blade is vertical, both in upward and downward directions. These flashes

apparently contain frequency components ranging from nearly 0 Hz to 1,500 Hz. The flashes alternate between up-Doppler (blade approaching the radar) and down-Doppler (blade receding from the radar). The flashes occur at six times the rotation rate of the turbine, with up-Doppler and down-Doppler flashes occurring three times each during one rotation period. Between the flashes, the amplitude of the spectrum drops by as much as 30 dB.

Modeling the rotor with blades made from perfect electrical conductor (PEC) produces the RCS characterization illustrated in Figure 83. In the time-domain plots, it is obvious that the scattering from the trailing edge of the blade, while split into two closely spaced components, has been reduced significantly in amplitude. Also, distinct peaks of lower amplitude appear between the peaks associated with the vertical leading and trailing edges of the blades. These occur when the flat, closed end of the blade is facing the radar. Another significant difference from the baseline rotor response appears in the total spectrum. The amplitude of the total spectrum from the PEC rotor rolls off at the larger Doppler shifts, unlike the baseline response. Significantly lower signal is present at Doppler shifts greater than about 1,000 Hz, especially for the down-Doppler return from the trailing edge. This effect can be easily seen in the spectrograms. These differences between the response of the fiber-composite rotor and the PEC rotor are significant enough that the use of PEC models entails an unacceptable risk that erroneous conclusions will be drawn about the effect of the turbine on a radar system of interest.

Because carbon-fiber composite can be electrically conducting, the question is posed whether or not a blade using carbon fiber in the spar caps will exhibit worse RCS performance than an otherwise identical blade that uses glass fiber in the spar caps. Figure 84 shows the RCS response of the baseline rotor, but with all of the carbon-fiber spar caps replaced with identically shaped structures using fiberglass composite material. Only very subtle differences can be seen when this response is compared with the baseline response in Figure 82. These subtle differences can best be discerned in the total spectrum plots, but differences are so small as to be practically non-existent. It appears that the two constructions are virtually interchangeable regarding RCS performance.

It is important to understand what parts of the blade contribute most to the Doppler spectrum. Treating only the dominant contributors might be a viable approach to achieving desired performance at lower cost. With this thought in mind, simulations have been performed with portions of the blade replaced with "perfect absorber". In the SBR implementation of Xpatch, a perfect absorber is completely opaque and does not scatter in any way. In the computer simulation, no surface currents radiate from the perfect absorber. While a perfect absorber does not really exist, it is a quite handy concept for testing the scattering effect of certain parts of the turbine blade. For example, Figure 85 shows the RCS response of the rotor when the internal shear web structures are replaced with perfect absorber. These shear webs have flat surfaces, and the flat surface is oriented generally toward the radar as the blade rotates through the vertical position. If the radar signal penetrates the outer surface of the blades, then the shear webs (and other internal components) can contribute to the overall scattering from the rotor. Comparison of Figure 85 with the baseline response in Figure 82 shows that the shear webs are a significant contributor to the radar scattering from the rotor. The time-averaged response has been reduced from 6.1 and 6.6 dBsm to 2.8 and 3.0 dBsm, for VV and HH polarizations, respectively. The slightly better than 3-dB reduction is accompanied by a more significant reduction in the spectrum at Doppler shifts larger than 1,000 Hz, similar to the response of the PEC rotor. Comparison with the RCS response of the PEC rotor in Figure 83, especially the spectrograms, shows that the fiber-composite rotor with perfectly absorbing shear webs is slightly quieter than the PEC rotor. It should be noted that, had only the PEC model been used, the importance of the contribution of the shear webs would have gone unnoticed.

Much of the surface of the turbine blade is covered with panels consisting of low-density foam sandwiched between thin fiberglass skins. Replacing these panels with perfect absorber produces the RCS performance shown in Figure 86. These panels cover a significant portion of the blade surface, but with the radar located at $AZ = 90°, EL = 0°$, the surface-normal vectors of these panels are not pointing toward the radar. Nevertheless, the primary RCS peaks are reduced about 6 dB with respect to the baseline, while the peaks that occur with the

blade vertically downward are reduced 10 to 12 dB. The total spectrum shows a pronounced dip at a Doppler shift of about +860 Hz. The negative Doppler amplitudes are also reduced 10 to 20 dB, depending on polarization and frequency. This reduction is apparent in the spectrograms, and is particularly obvious for the HH polarization. The time-averaged RCS has dropped from 6.1 and 6.6 dBsm to 3.4 and 3.6 dBsm, for VV and HH polarizations, respectively.

When the shear webs and all components consisting entirely of fiber-glass laminate are replaced with perfect absorber (foam sandwich panels and components containing carbon-fiber remain intact), the time-averaged RCS drops significantly to –9.7 dB and –11.2 dB, respectively for VV and HH polarizations. This amounts to a reduction of 15 to 18 dB with respect to the untreated rotor. The RCS performance for this configuration is displayed in Figure 87. The primary peaks have been reduced by at least 20 dB, while the peaks associated with the downward pointing blade have been reduced by more than 20 dB for VV polarization and more than 30 dB for HH polarization. The overall reduction in RCS causes the time-domain peaks that occur when the blade tips are pointed toward the radar to become more apparent, although these peaks are reduced about 3 dB from those produced by the baseline rotor. The amplitude of the total spectrum has been reduced 20 to 30 dB, depending on Doppler shift. The spectrogram shows that the flashes that occur when the blades are in vertical orientations have been reduced very significantly.

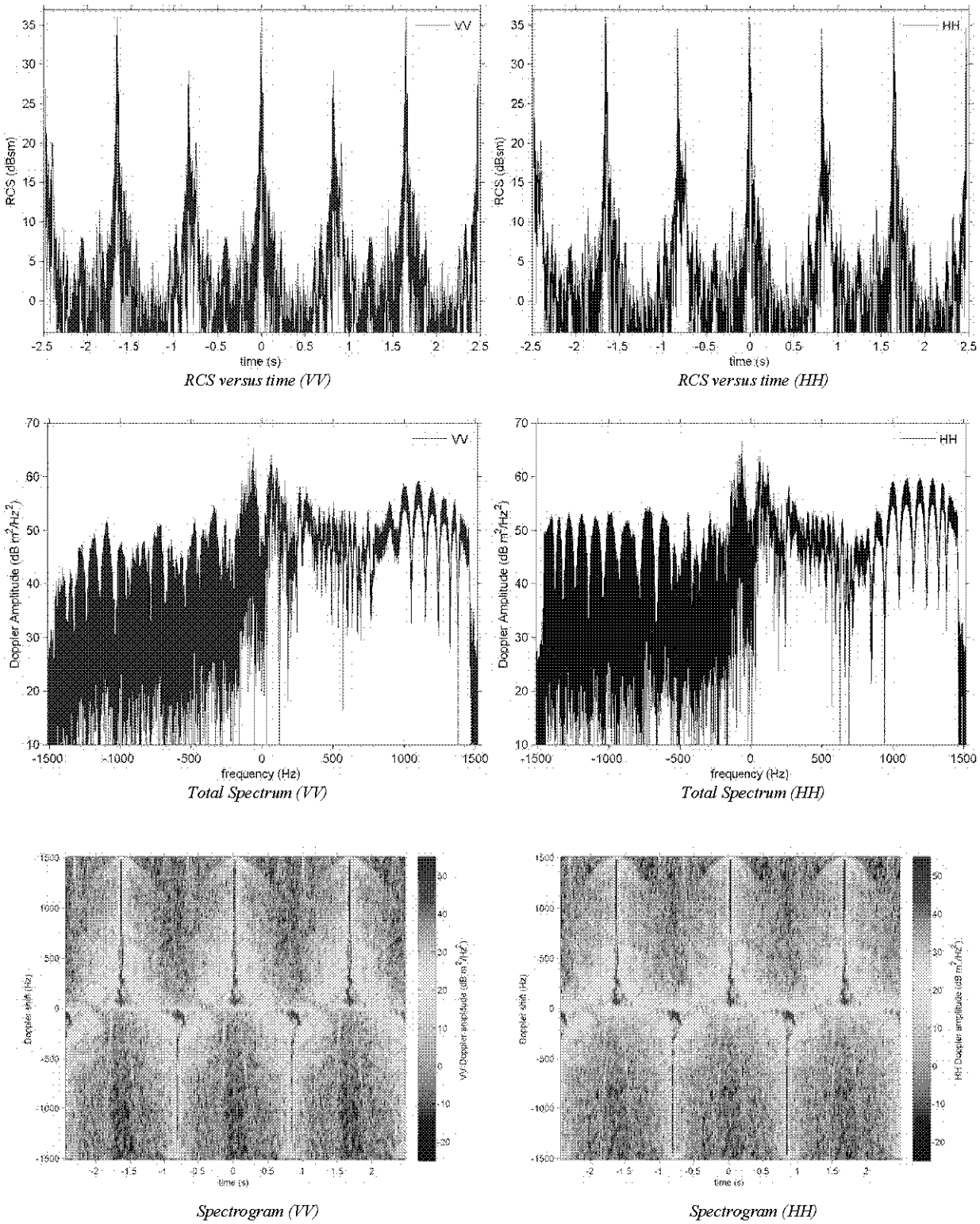

RCS versus time (VV) *RCS versus time (HH)*

Total Spectrum (VV) *Total Spectrum (HH)*

Spectrogram (VV) *Spectrogram (HH)*

Figure 82 Radar response of the untreated 3-blade rotor, computed at $f = 2.8$ GHz, with materials as described in the text.

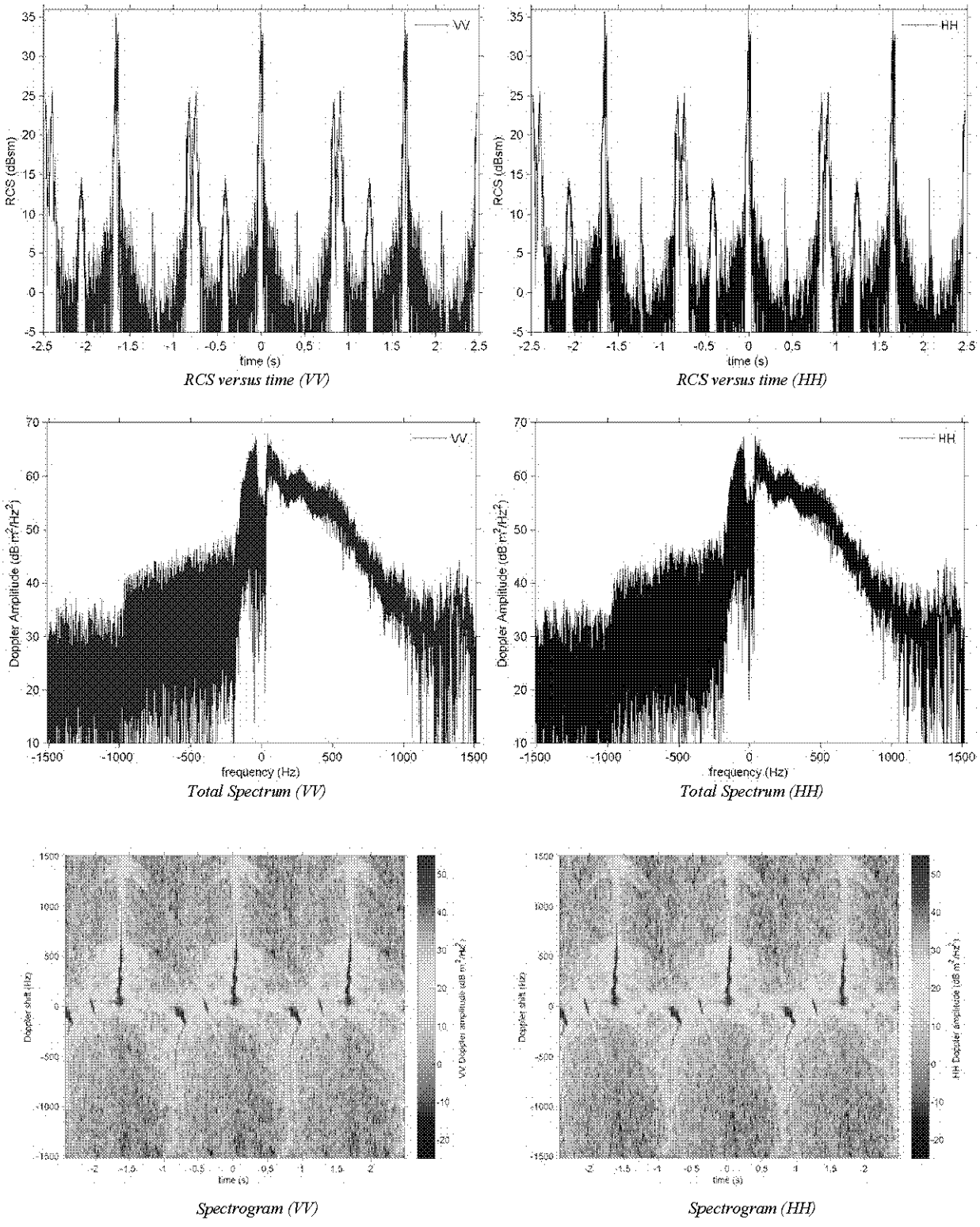

RCS versus time (VV) *RCS versus time (HH)*

Total Spectrum (VV) *Total Spectrum (HH)*

Spectrogram (VV) *Spectrogram (HH)*

Figure 83 Radar response of the PEC 3-blade rotor, computed at $f = 2.8$ GHz.

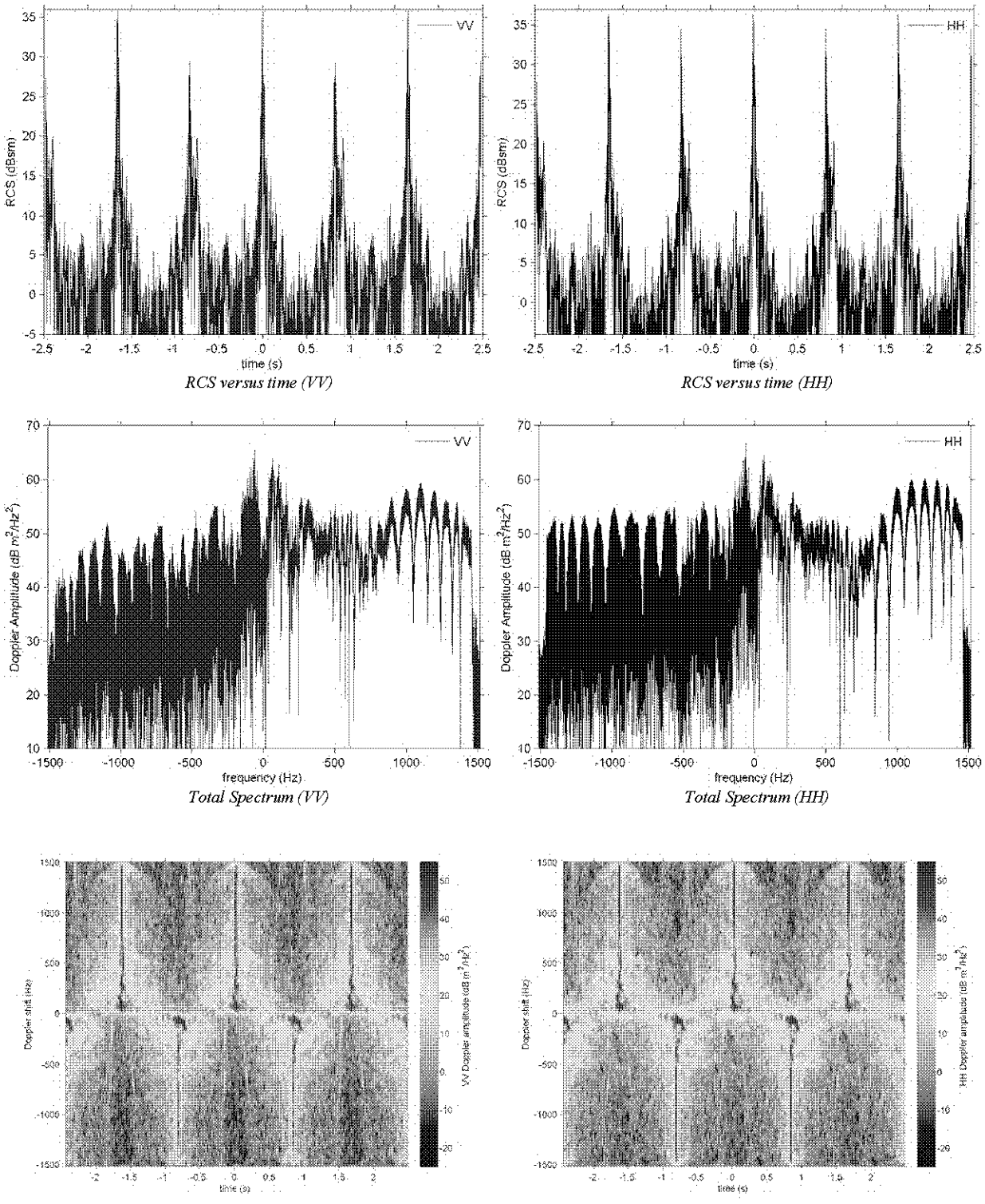

Figure 84 *Radar response of the original 3-blade rotor, but with all carbon-fiber composites replaced with uniaxial-glass composite, computed at* $f = 2.8$ GHz.

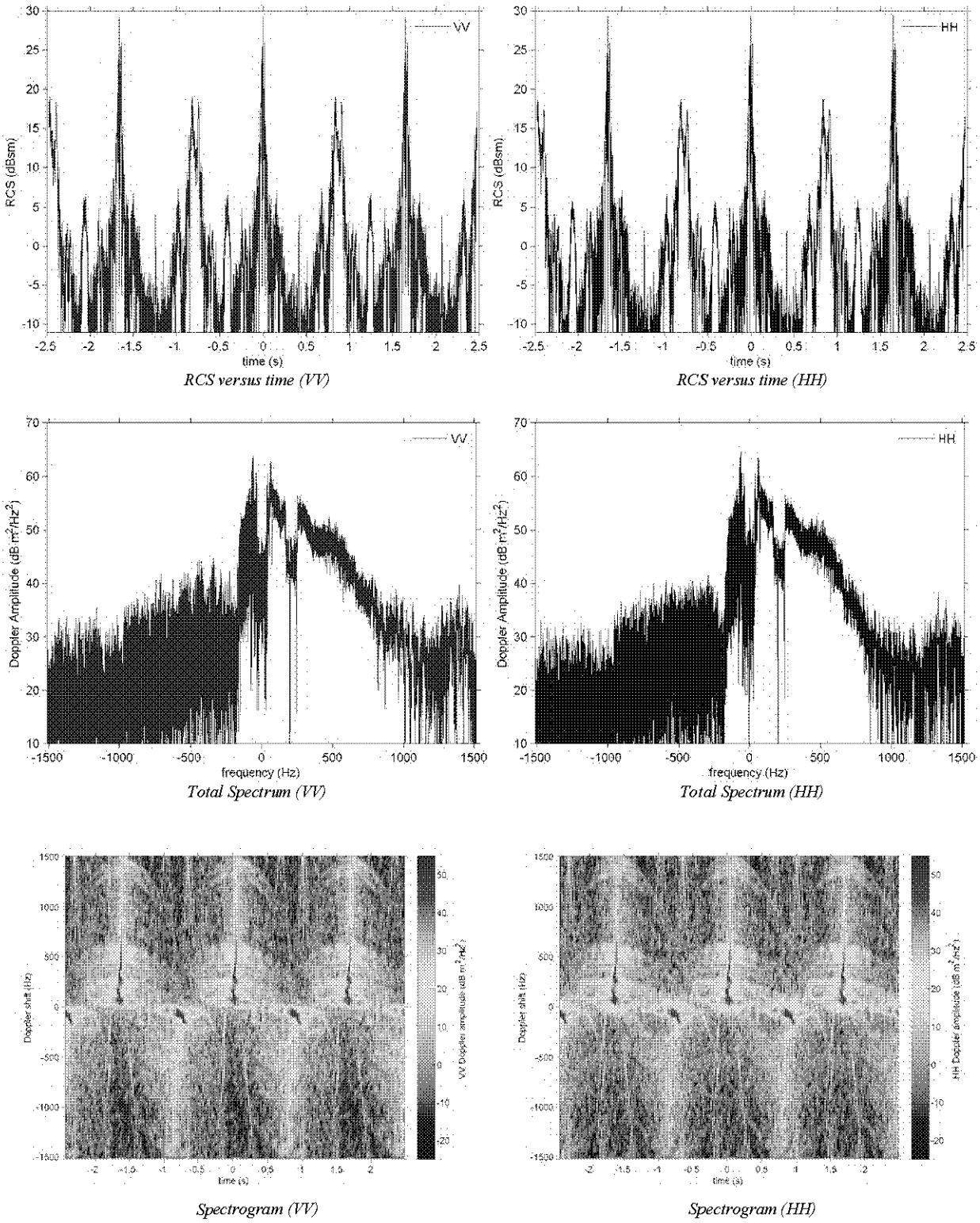

Figure 85 *Radar response of the original 3-blade rotor, but with the internal shear webs replaced with perfect absorber, computed at* $f = 2.8$ GHz.

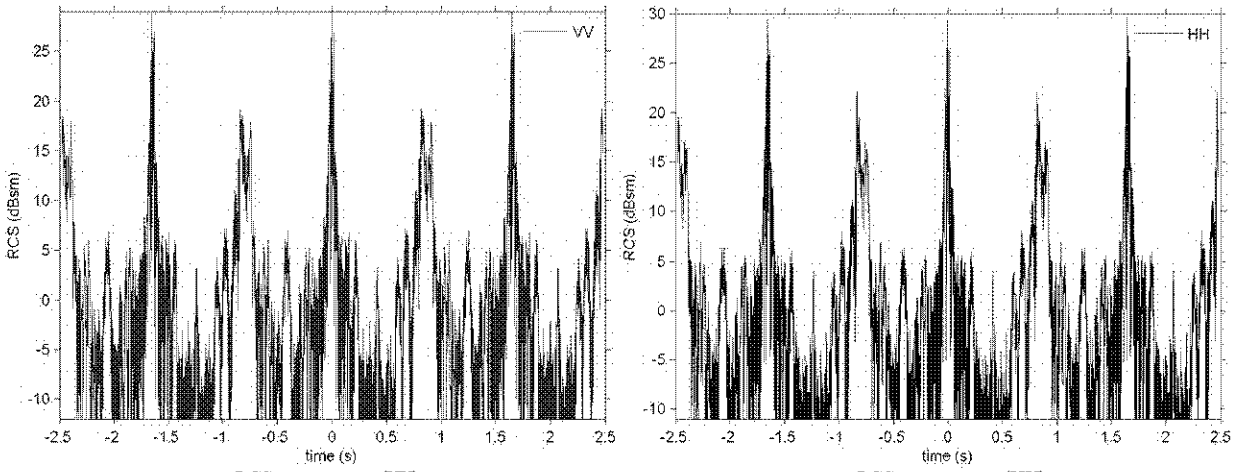

RCS versus time (VV)

RCS versus time (HH)

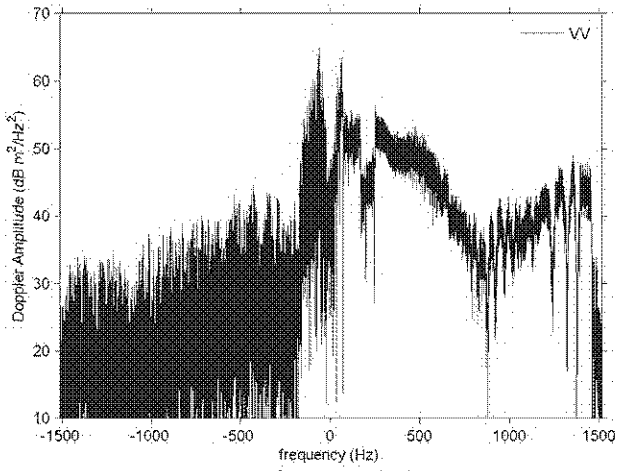

Total Spectrum (VV)

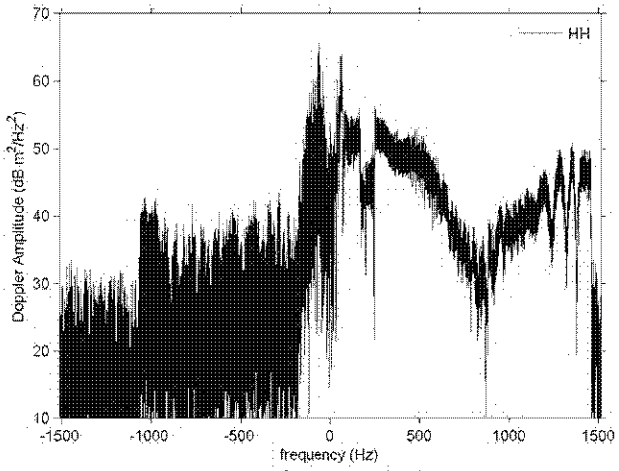

Total Spectrum (HH)

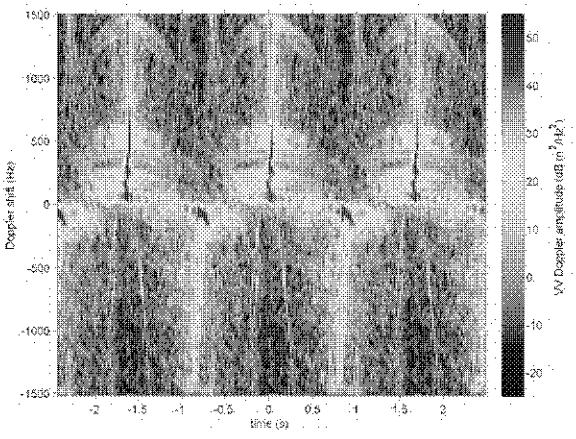

Spectrogram (VV)

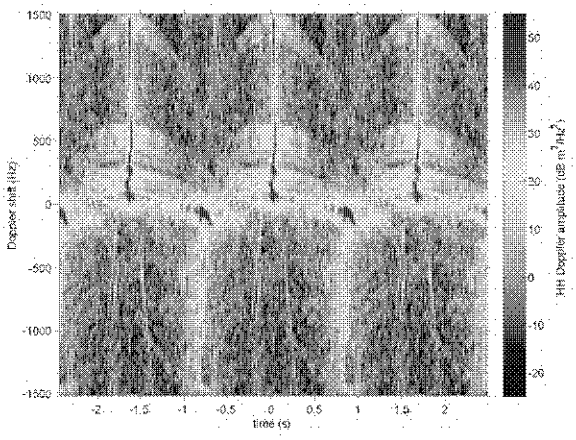

Spectrogram (HH)

Figure 86 Radar response of the original 3-blade rotor, but with the glass-foam sandwich panels replaced with perfect absorber, computed at $f = 2.8$ GHz.

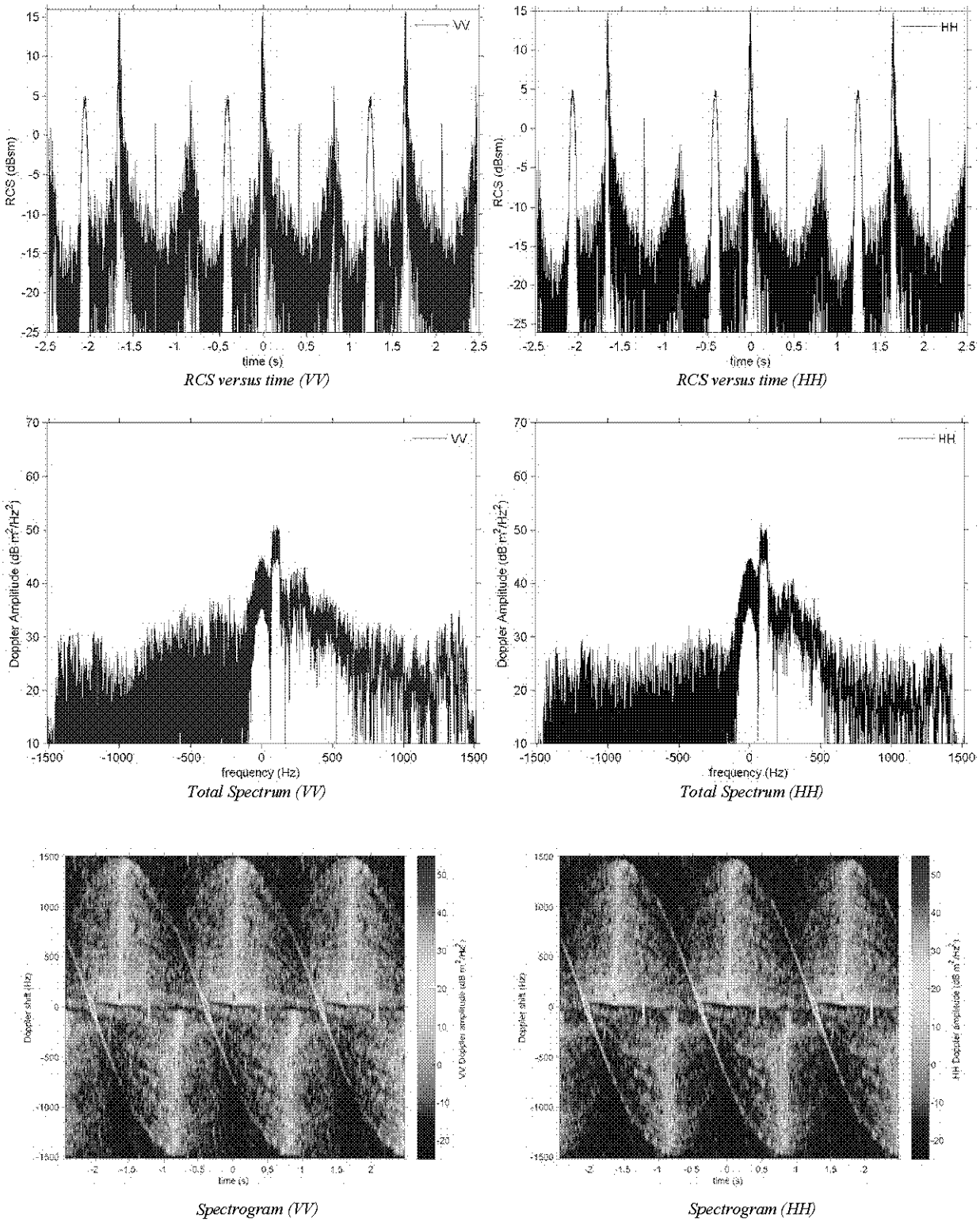

Figure 87 *Radar response of the original 3-blade rotor, but with the internal shear webs and all components comprised only of fiber-glass (no foam or carbon fiber) replaced with perfect absorber, computed at* $f = 2.8$ GHz.

7.4.1.2 Radar Located at $AZ = 0.65°, EL = -3.0°$

Consider locating the radar at $AZ = 0.65°$, which is the direction of one of the two primary peaks in the static RCS response in Figure 76. Since the radar is looking nearly down the axis of rotation, the peak Doppler shift would be very small if the elevation remained at 0°; with f = 2.8 GHz, the peak Doppler shift would only be about 17 Hz. However, if the rotor is tilted up by 3°, equivalent to placing the radar at $EL = -3°$, the peak Doppler shift increases to 79.8 Hz. At this S-band radar frequency, the peak Doppler would correspond to a target moving at 4.3 m/s or 9.6 mph.

The RCS response of the unmodified fiber-composite rotor, when viewed from this position, is displayed in Figure 88, where it is seen that the maximum RCS has risen considerably to about 52.3 dBsm, up from about 36 dBsm when the rotor was viewed at $AZ = 90°, EL = 0°$ (see Figure 82). The resulting Doppler spectrum is very strong, although it has a narrow bandwidth since the peak Doppler shift is less than 80 Hz. The character of the spectrogram has changed, and the large flashes of up-Doppler and down-Doppler have both shifted to the left, and they have also shifted closer together. The maximum up-Doppler response no longer occurs when a blade is in the vertical orientation, but instead when the blade is about 36° away from vertical. Similarly, the down-Doppler peak occurs when the blades are close to 60° away from vertical.

The PEC model of the rotor produces the RCS response shown in Figure 89, which differs somewhat from the response of the original rotor, Figure 88. These differences are more subtle at this radar position than when the radar was located at $AZ = 90°$. However, the differences are clearly visible in Figure 90, where, for each rotor model, the VV time-domain response is plotted at left, and the total spectrum is plotted on the right. The PEC model shows higher RCS in the regions centered near times $t = -1.8, -1, -0.2, +0.7, +1.5, +2.3$ s, while the original composite model exhibits greater RCS in regions around $t = -2.4, -1.2, -0.7, +0.4, +1.0, +2.07$ s. The differences in the total spectrum are also subtle, but the composite model produces more energy at Doppler shifts of –79 and +76 Hz, as well as near ±6 Hz. On the other hand, the PEC model produces significantly more energy around –18 Hz. Perhaps the most useful comparison is between the two spectrograms. While the up- and down-Doppler flashes are very similar, the spectra between the flashes differs considerably; the composite model shows about 20 dB more signal at the higher frequencies than does the PEC model in this region.

A substantial portion of the blade surface is made of a sandwich consisting of a thick layer of low-density foam placed between two thin layers of fiberglass. Figure 92 shows the RCS response when all of this material is replaced with perfect absorber. The response is not significantly different from the untreated rotor. This implies, at least at this aspect angle, that the foam sandwich material is not a dominant contributor to the overall RCS and Doppler response of the turbine. However, the data below demonstrate that this should not be construed as evidence that the sandwich material can be ignored and left untreated.

The spar caps of the blades are made from carbon-fiber composite. Replacing these parts with perfect absorber produces the RCS response illustrated in Figure 93. The peak RCS, taken over one period of rotation, has been reduced to 46.3 dBsm, about 6 dB lower than for the untreated blade (Figure 88). This indicates that the spar caps are a significant contributor when the rotor is viewed from this angle. The time-domain response shows only three prominent peaks, whereas the untreated blade show nine peaks, all within about 3 dB of each other. This results in a significant reduction of the amplitude of the total spectrum at many frequency shifts, most notably in the up-Doppler portion of the spectrum, and also at the higher down-Doppler shifts. The reduction is on the order of 10 dB or better. The spectrograms are particularly informative, showing that the up-Doppler flash has been reduced 10-15 dB, with the most reduction at the higher frequencies. The down-Doppler flash shows on the order of 20 dB reduction at the higher frequencies, but little change at the lower frequencies, below about 40 Hz. While the spar caps are clearly a major contributor to the RCS and Doppler spectrum, other portions of the blade are clearly significant contributors as well.

Replacing all the components made entirely from fiberglass or carbon-fiber composite with perfect absorber (the sandwich panels are unchanged) produces the RCS performance illustrated in Figure 94. The peak RCS has been reduced by about 9 dB, to 43 dBsm, and the Doppler spectrum shows a substantial reduction. In the spectrogram, the bright Doppler flashes are gone, and the character of the spectrogram is quite different. The lower half of the down-Doppler flash still remains, although it has been reduced somewhat from the case where only the carbon-fiber composite was replaced with perfect absorber. Note that the responses that are present in Figure 94 are due to the fiberglass and foam sandwich panels, which have now become the significant contributors.

This study, though limited to just two radar positions, has provided some useful insights into the RCS performance of a fiber-composite wind turbine. The simulations indicate that internal structures are a very important contributor when the electromagnetic wave penetrates into the interior of the blade. This is a point that would have been missed entirely if the baseline blade had been modeled as a perfect electric conductor. It has also been demonstrated that when the radar is located at $AZ = 90°, EL = 0°$, the RCS is dominated by the components built entirely of fiberglass and by the internal shear webs. Similarly, when the radar is located at $AZ = 0.65°, EL = -3.0°$, the RCS is dominated by the components built entirely of fiberglass or carbon-fiber composite. However, at these two radar positions, the sandwich panels, comprised of low-density foam and fiberglass, do not appear to be as important to the overall RCS of the untreated turbine, since replacing them alone with perfect absorber has minor effect. Nevertheless, replacing the dominating materials with perfect absorber has demonstrated that the sandwich panels must also be treated, and shows that their contribution is on the order of 10 dB lower than that of the components made entirely from fiberglass or carbon-fiber composite. Similar studies need to be performed with other radar positions, and additional cases will be included in a future report.

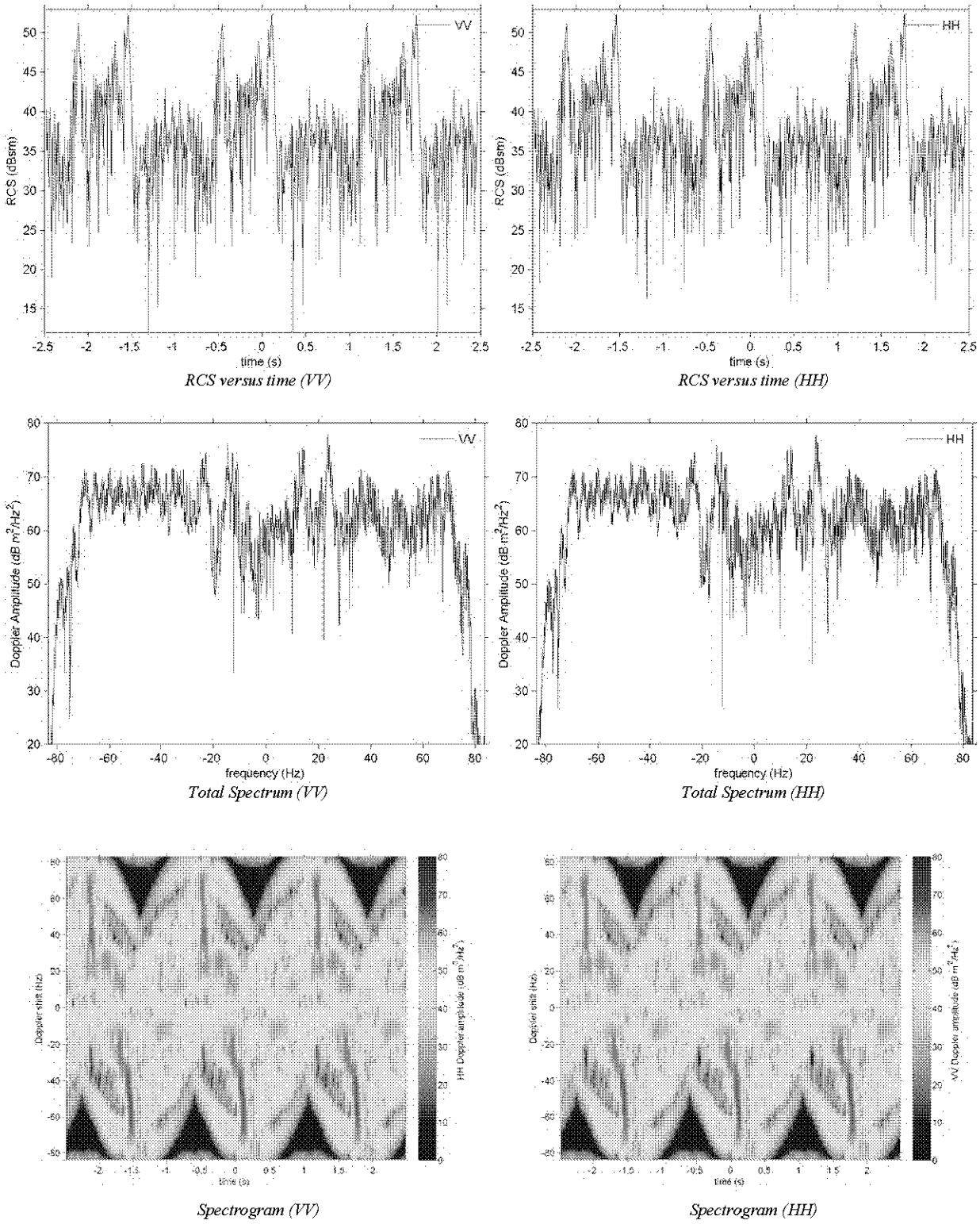

Figure 88 *Radar response of the original 3-blade rotor, with the radar located at* $AZ = 0.65°$ *and* $EL = -3.0°$, *computed at* $f = 2.8$ GHz.

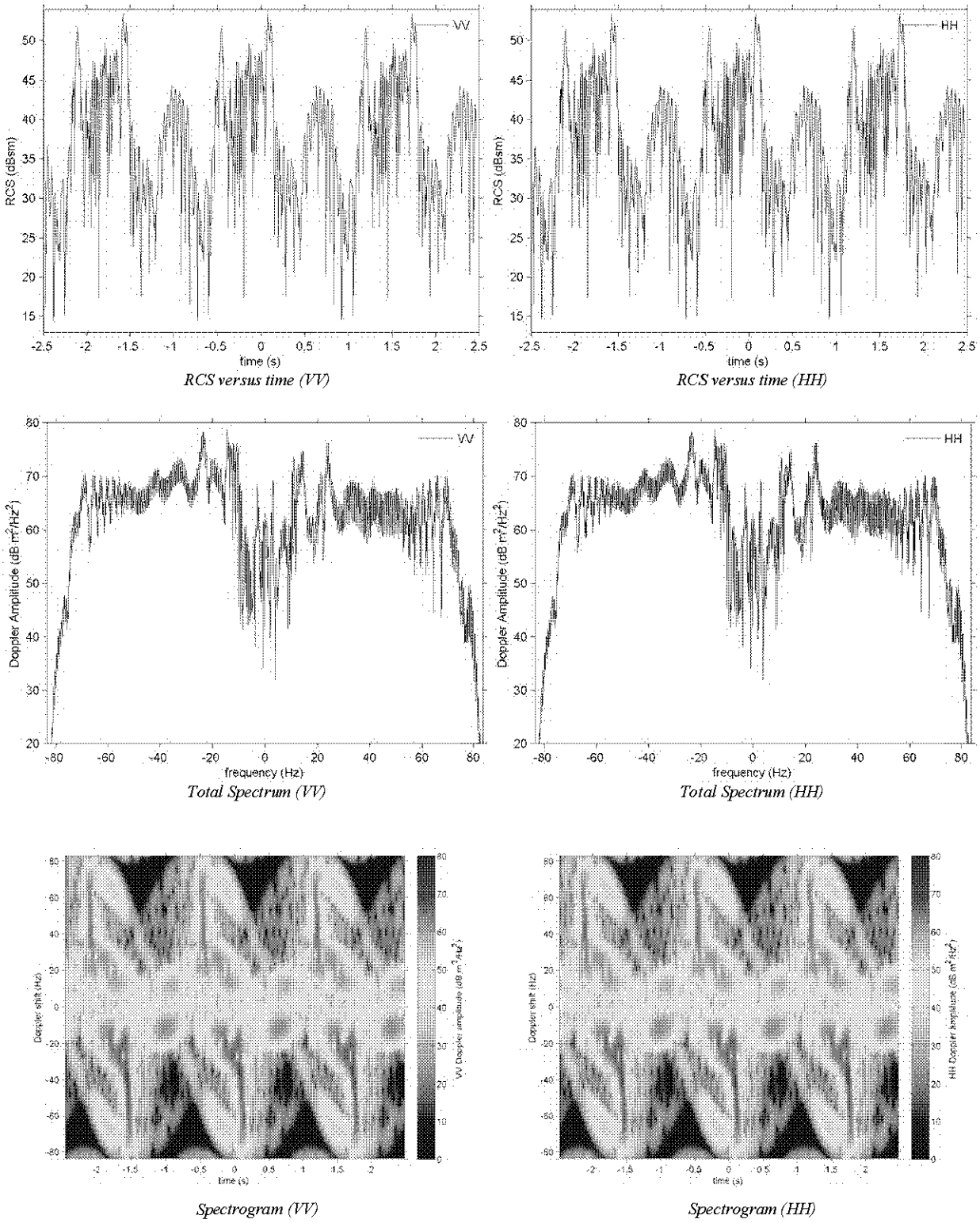

RCS versus time (VV) *RCS versus time (HH)*

Total Spectrum (VV) *Total Spectrum (HH)*

Spectrogram (VV) *Spectrogram (HH)*

Figure 89 Radar response of a PEC rotor, with the radar located at $AZ = 0.65°$ *and* $EL = -3.0°$*, computed at* $f = 2.8$ GHz.

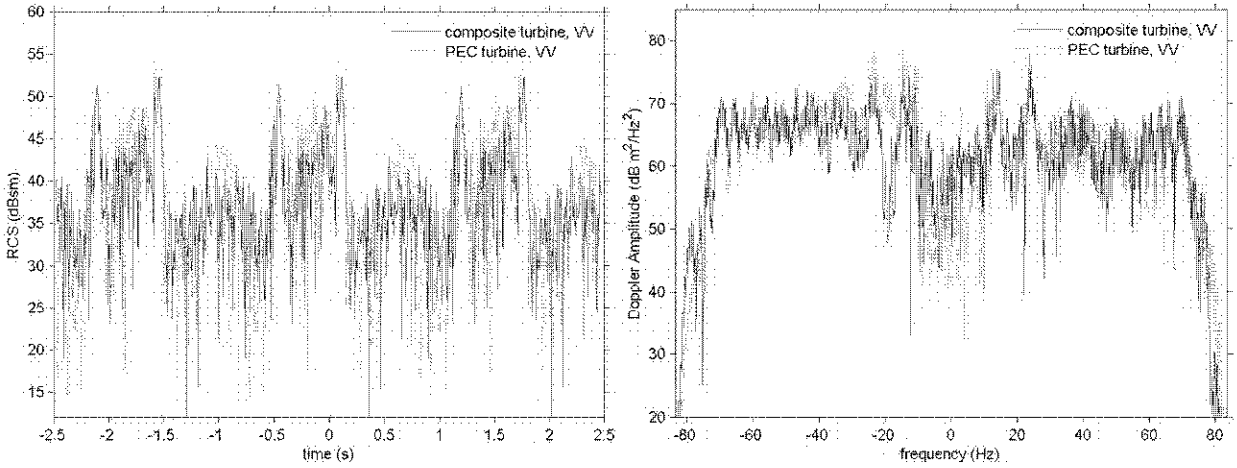

Figure 90 *Comparison of the RCS response in the time-domain (left) and the total spectrum (right) for the original composite rotor (red) and the PEC rotor (blue).*

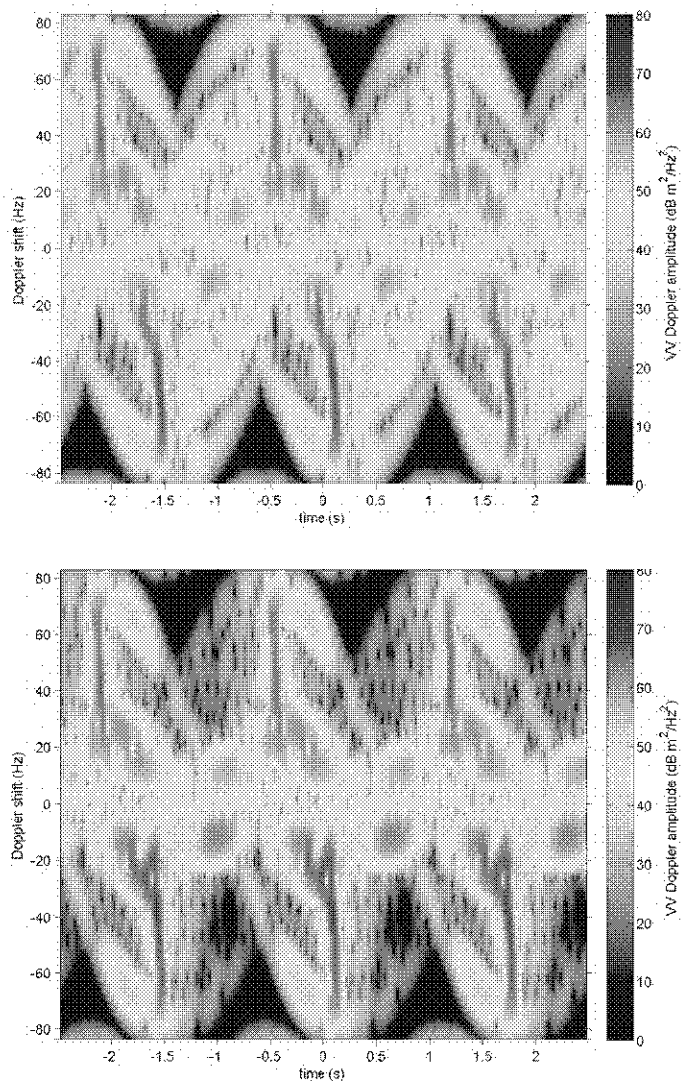

Figure 91 *Comparison of the spectrograms for the original composite rotor (top) and the PEC rotor (bottom).*

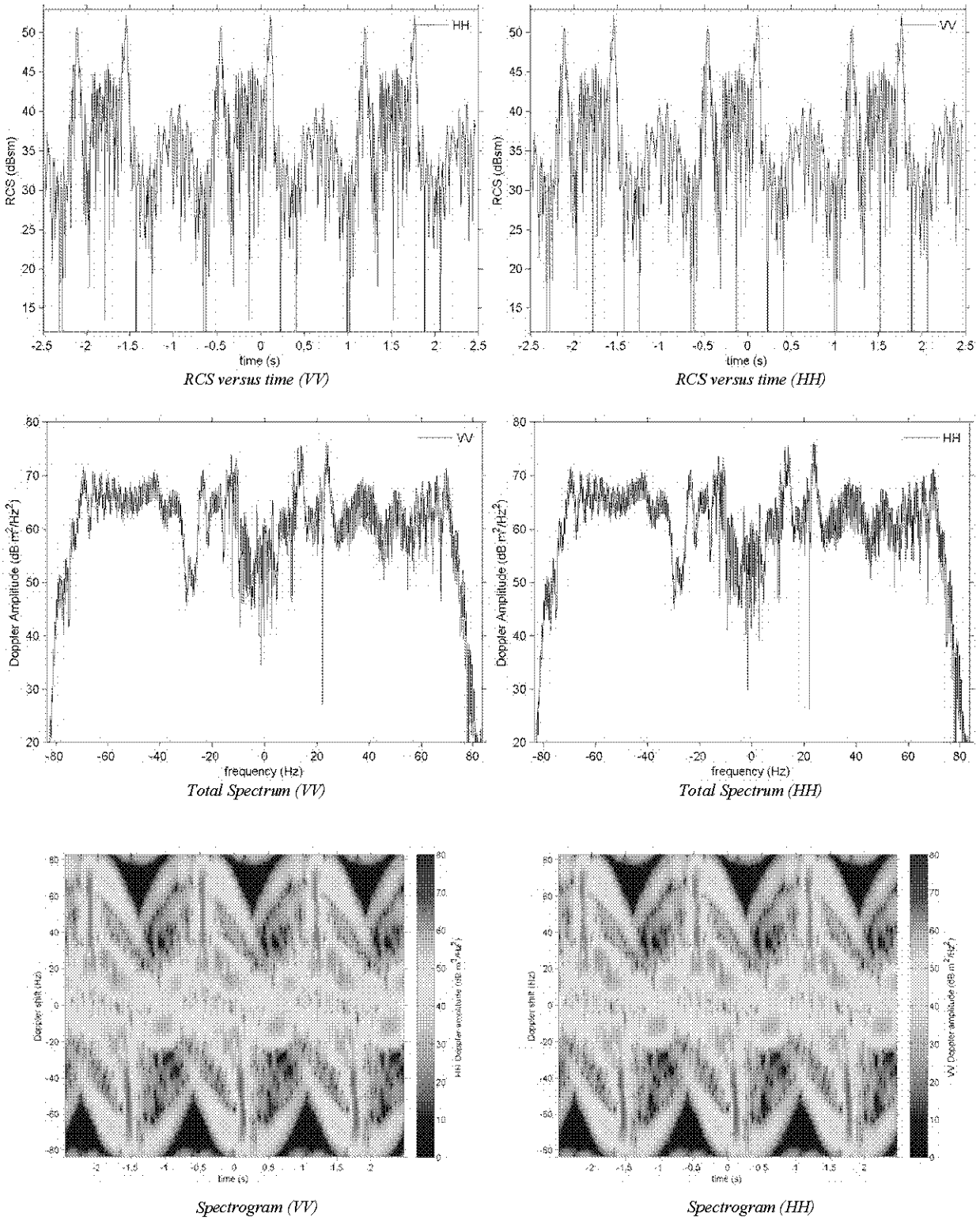

Figure 92 Radar response when the foam/fiberglass sandwich is replaced with perfect absorber, and the radar is located at $AZ = 0.65°$ *and* $EL = -3.0°$, *computed at* $f = 2.8$ GHz.

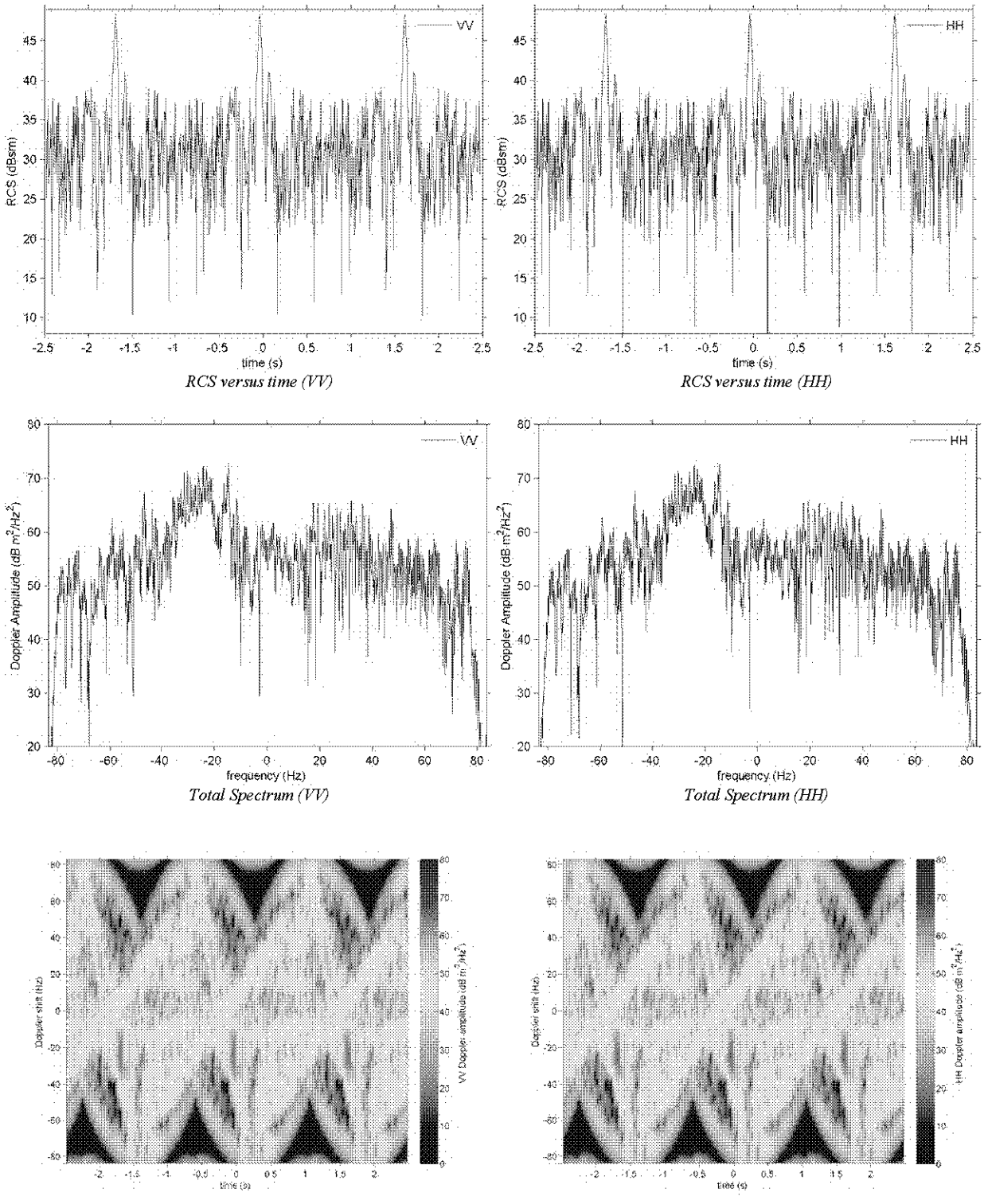

Figure 93 Radar response when carbon-fiber sections (spar caps) are replaced with perfect absorber, and the radar is located at $AZ = 0.65°$ *and* $EL = -3.0°$, *computed at* $f = 2.8$ GHz.

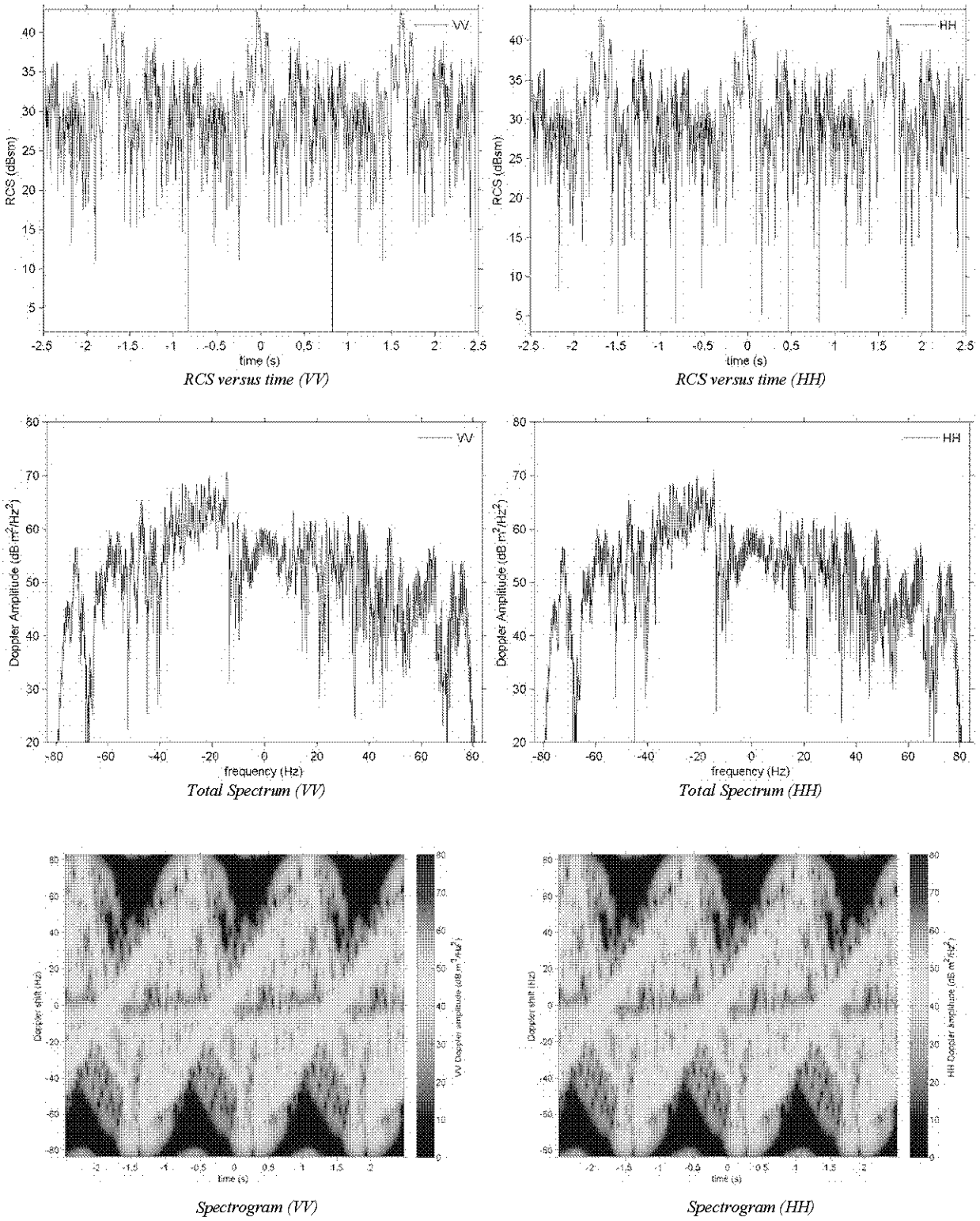

RCS versus time (VV) *RCS versus time (HH)*

Total Spectrum (VV) *Total Spectrum (HH)*

Spectrogram (VV) *Spectrogram (HH)*

Figure 94 Radar response when the fiberglass and carbon-fiber sections are replaced with perfect absorber, and the radar is located at $AZ = 0.65°$ *and* $EL = -3.0°$, *computed at* $f = 2.8$ GHz.

8. Integration Validation – Measurement Phase 2

8.1 Preliminary Measurement Results

This section summarizes preliminary RCS measurements of various flat plates, including metal plates, resistive materials, and both sandwich and spar-cap reference plates. All samples were measured using a compact range located at the Sandia Facility for Antenna and RCS Measurements on Kirkland AFB. The test samples were mounted on a low RCS foam mast, and the measurement radar calibrated using a 20-inch diameter metal sphere. Figure 95 shows the compact range and mounting of sample plates.

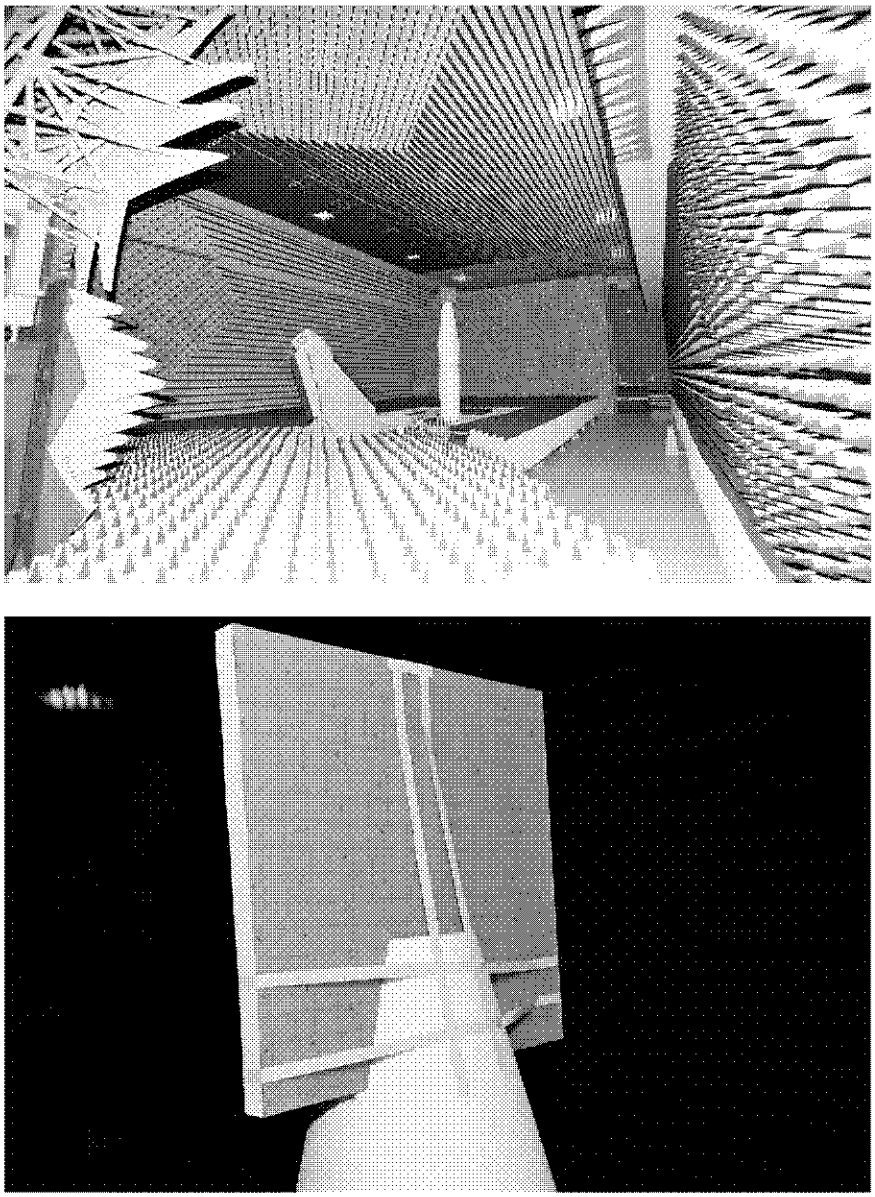

Figure 95 View of the compact range with a test sample mounted on the mast and the mounting approach.

Two small verification spheres were used to check the quality of the calibration. The measured RCS for the verification spheres, in the time domain, is shown in Figure 96. The peak response from the spheres is approximately 40 dB above the background clutter. All measured targets were significantly larger than the verification spheres.

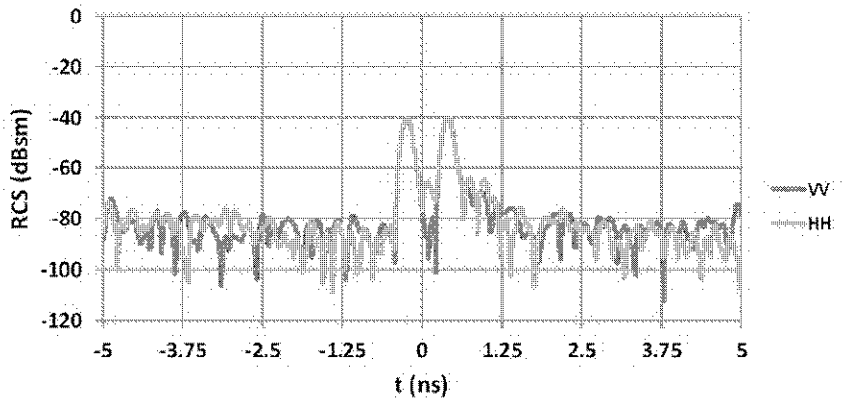

Figure 96 Time domain RCS for two 0.3125-inch diameter spheres. Both VV and HH polarizations are shown.

Two different sizes of aluminum plates were measured to validate the fidelity of the measurement system. Figure 97 contains the difference between analytic, modeled, and measured RCS for two different aluminum plate sizes. Both measured and analytical data are referenced to numerically-modeled data, as analytical results do not account for plate thickness (~ one inch for both plates), and measured data includes pointing and calibration error. Results indicate that the measured RCS is accurate to within ± 2 dB.

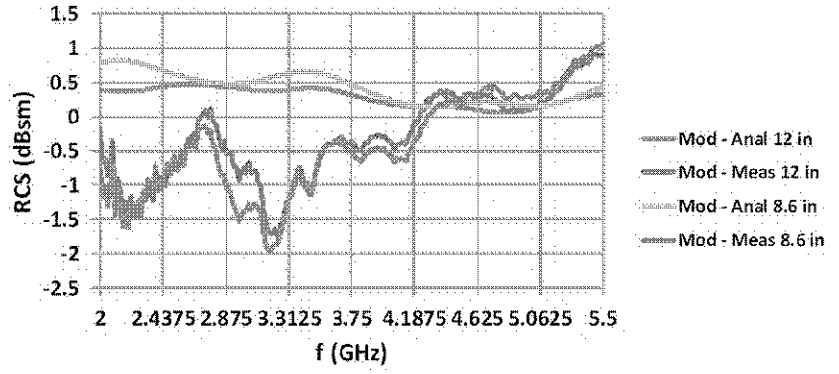

Figure 97 Measured RCS of aluminum plates compared to analytical and numerical data for plate sizes of 8.6 inches x 9.12 inches and 12 inches x 12 inches.

As outlined in *Fabrication of Test Panels*, plates representative of various structural elements common in a turbine blade were constructed using VARTM processes. The following plates were constructed and measured:

- Balsa-sandwich plate
- Foam-sandwich plate
- Glass spar-cap plate
- Carbon spar-cap plate

The spar-cap plates were extremely heavy. As a result, improper mounting on the foam mast introduced significant pointing error in measured RCS. New fixtures are currently being fabricated to properly support spar-cap plates.

Sandwich plates had no mounting issues. Figure 98 contains measured RCS of balsa- and foam-sandwich plates compared to modeled data. Differences between modeled and measured plate RCS can be attributed to variations in the fabrication process and pointing error mounted on the foam mast. The sandwich-plate RCS is significantly lower than that of an equivalently sized PEC plate.

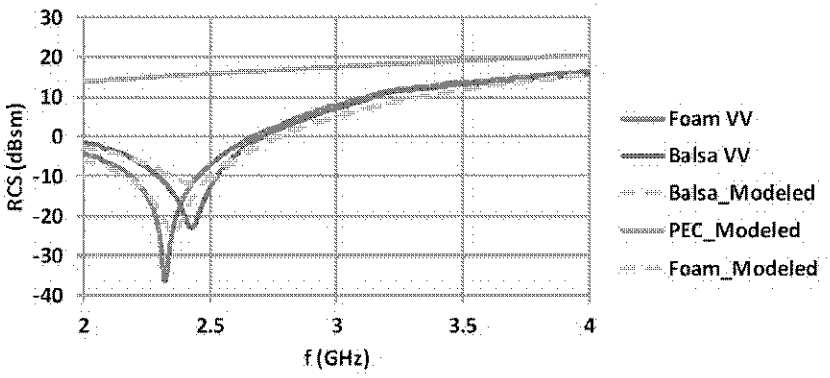

Figure 98 Measured RCS of foam and balsa-sandwich plates compared to modeled data.

Construction and measurement of sandwich and spar-cap plates was initially intended to achieve two goals: to gain understanding of VARTM processes, and to provide a non-PEC reference which could be used to establish an RCS reduction metric. Agreement with predictions from modeled plates indicates that VARTM processes are well characterized. In light of further analysis, however, flat plates do not provide a useful reference for calculating an RCS reduction metric. Flat plate samples of blade materials show a significantly reduced RCS at a narrow frequency band, as the plate thickness becomes a resonant length and the incident RF energy transmits through the plate (as seen near 2.3 GHz and 2.4 GHz in Figure 98). In a blade structure, this transmitted energy scatters from internal components, such as the shear webs, and returns to the radar (see the section *Modeling the Radar Cross Section (RCS) of a Wind Turbine*). A flat plate measurement does not include scattering from these internal components.

In terms of RCS comparison between reference plates and absorber plates, the reference plate's low RCS is due to transmission, whereas the treated plate's low RCS is due to absorption. Transmitted energy scatters from other blade elements and returns to the radar, whereas absorbed energy does not return to the radar. Consequently, comparing absorber designs to flat reference plates does not capture the complex nature of scattering in an actual blade. Measurement of flat plate absorbers does provide useful information, notably fabrication process compatibility and RCS reduction relative to PEC; however, RCS reduction compared to composite blade structures must be evaluated through modeling or measurement of actual blades.

In addition to reference plates, several resistive-sheet samples were measured to evaluate the sheet resistance (in Ω/square) against vendor claims. The following materials, in 6-inch square samples, were measured and compared to models in an attempt to extract Ω/square values:

- Eeonyx material with 300 Ω/square
- Eeonyx material with 200 Ω/square
- Eeonyx material with 300 Ω/square
- Eeonyx material with 425 Ω/square
- Cuming MW space cloth with100 Ω/square
- Cuming MW space cloth with 377 Ω/square
- Cuming MW space cloth with 1000 Ω/square
- Carbon fiber, TMGC 6003

The measured RCS of various resistive materials compared to modeled data is shown in Figure 99. Measurements of 6-inch resistive sheet samples revealed that the measurement setup does not have the precision required to extract Ω/square values with a high degree of accuracy; nonetheless, all measurements qualitatively validate vendor claims (e.g. 300 Ω/square RCS < 200 Ω/square RCS). Higher-fidelity RF measurements of resistive fabrics are currently in progress using the GR900 coaxial measurement fixture.

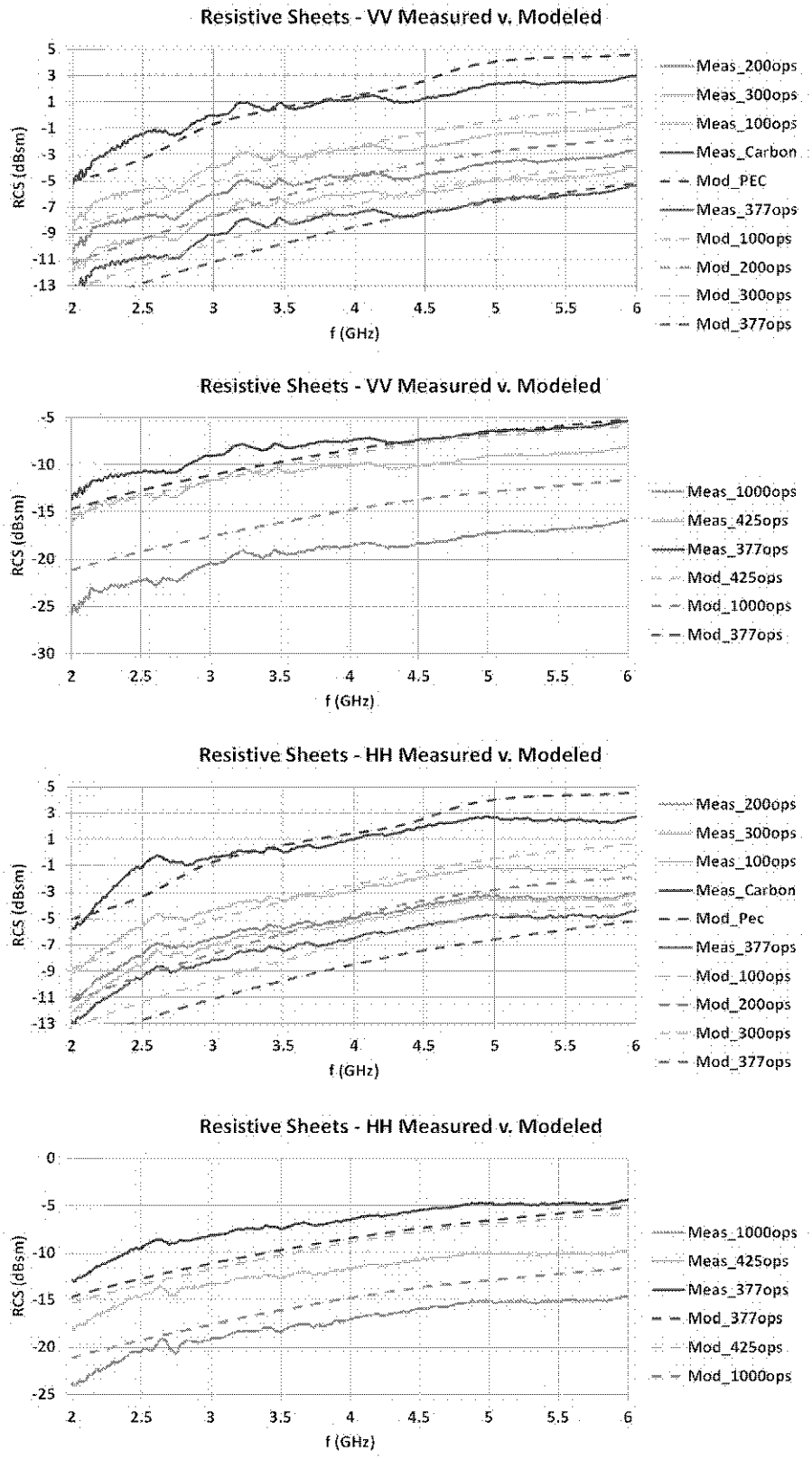

Figure 99 *Measured RCS of various 6-inch resistive fabrics compared to modeled data. Top two plots – vertical polarization, bottom two plots – horizontal polarization.*

9. Summary of Current Status and Future Directions

Towards the design and implementation of low RCS wind-turbine blades, the following tasks have been completed:

- The current state-of-the-art in absorber design and wind-turbine RCS modeling were evaluated to establish a baseline for future work.

- Electromagnetic models were developed across several tools to enable design of high performance absorbers and analysis of wind-turbine RCS.

- Common blade materials were measured to determine electrical properties. Novel materials (absorptive, electric, and magnetic) were developed in a manner compatible with common blade fabrication processes (VARTM, pre-preg). Material development and measurement enabled design of high performance absorbers capable of integration into blades.

- Absorbers were designed for integration into blade fabrication processes, based on inputs from material development and measurement. These designs indicate that high RF performance can be achieved with minimal impact on existing fabrication processes. Statistical analyses demonstrate that designs perform well over tolerances encountered with current fabrication processes.

- As prototype designs transition towards blade integration and mass production, fabrication process control will be a critical determinant of turbine RCS. A better understanding of VARTM processes was developed in support of future blade integration efforts.

- A large, 126-m diameter, wind-turbine rotor set was modeled to provide insight into turbine RCS. Both static and Doppler effects were investigated. Comparison of a composite and PEC blade reveals the need to model the actual blade structure, in terms of both shape and materials. Significant understanding was gained as to dominant scattering structures and appropriate treatment solutions.

- To support validation of the designs, reference plates, which are representative of several blade structural components, were measured. Fabrication of integrated absorber prototypes is currently underway. Integrated absorber prototypes will be measured and compared to models. This effort will be reported in Part 2 of this report.

The results presented here demonstrate the feasibility of reducing wind-turbine RCS with minimal impact to existing fabrication processes. Significant progress has been made toward an at-the-turbine solution to the problem of radar-windfarm interaction; even so, many issues still prevent large scale production of low RCS wind turbines. We believe future work on at-the-turbine solutions should focus on the following areas (in order of importance):

- Small-scale integration into prototype blades

  Although integrated absorber designs show great promise, actual performance in a full blade has not yet been modeled or measured. Building and testing small (9m-13m) blades, both treated and untreated versions, would validate the design approach, provide insight into fabrication techniques, and demonstrate a reduced radar signature in an operational environment.

- Wind-turbine RCS Modeling

Significant work remains in the area of wind-turbine RCS modeling. Wind-turbine models require an immense amount of computation, and the characterization of the RCS of wind turbines, including static, Doppler, and multipath effects, is an extremely complex endeavor. Integration with super-computing resources available at SNL would reduce computation times and enable a better understanding of turbine radar signature through more thorough and complete simulations.

Current absorber designs, though compatible with blade fabrication processes, apply to flat plate structures. The simulation of the radar scattering from absorbers integrated into a blade model would provide insight into achievable RCS reduction for an actual turbine.

- Materials Development

  Resins doped with ferrites, titanates, and glass micro-balloons expand the material options available to RF engineers. Initial progress from this effort should be continued, particularly in the area of integration with blade fabrication processes.

  Carbon has desirable electrical and mechanical properties. Carbon-based materials have been used in EMI, shielding, and absorption, indicating a wide range of electrical properties based on composition (graphene, fullerenes, fibers). As the use of carbon in structural components of large blades increases, finding the appropriate composition for both electrical and aerodynamic design could have immense cost impact.

  Material solutions developed in this study (thin metal deposition, polymer coated fabrics, doped resins) should be further investigated to determine suitability for mass production. The practicality of these technically viable approaches must be determined with regard to size and cost scaling.

- Analysis and Design Process Improvement

  The treatments designed in this study used standard computing resources and electromagnetic design tools. Optimized absorber performance is limited by available optimization techniques, whether random, gradient, or algorithmic, and by computing resources. Development of custom code and integration with supercomputing resources at Sandia would expand available optimization techniques and do more with existing techniques.

- Advanced Electromagnetic Analysis

  Although significant RCS reduction has already been achieved with a Jaumann absorber approach, many experts claim that Circuit Analog Absorbers (CAA) can improve absorber performance for a given thickness [3]. Investigation into CAA approaches could result in further RCS reduction.

  The solutions presented in this report assume a metal backed absorber. Non-metal backed absorbers would allow RF energy to penetrate into the blade structure and possibly pass through the blade. From a radar perspective, transparent turbines are preferred to absorptive turbines, since absorptive turbines would still create a shadow region where radar visibility is low. Electromagnetic analysis becomes significantly more complex for non-metal backed absorbers, but the potential benefits of applying frequency-selective surfaces [3] to make portions of the blade transparent to radar signals warrants investigation.

  Techniques using periodic structures to create novel electromagnetic behavior are finding increasing application in a wide range of RF systems. Though of limited near-term applicability, these metamaterials and artificial magnetic conductors hold promise for developing new low-observable structures, and should be considered in forward-looking research.

References

[1] Billy C. Brock, Steven E. Allen, Ward E. Patitz, Troy V. Satterthwait, James F. Carroll III, *A First Look at Modification of the Radar Cross Section of Wind-Turbine Blades*, Sandia National Laboratories report, SAND2010-8678, Albuquerque, February 2011. (Official Use Only)

[2] K.N. Rozanov, "Ultimate Thickness to Bandwidth Ratio of Radar Absorbers," *IEEE Transactions on Antennas and Propagation*, vol. 48, no. 8, pp. 1230-1234, August 2000.

[3] B.A. Munk, *Frequency Selective Surfaces: Theory and Design*, John Wiley & Sons, New York, 2000.

[4] E.F. Knott, J.F. Shaeffer, and M.T. Tuley, *Radar Cross Section, 2nd edition*, Artech House, Norwood, 1993.

[5] G.T. Ruck, D.E. Barrick, W.D. Stuart, C.K. Krichbaum, *Radar Cross Section Handbook, Volume 1*, Plenum Press, New York, 1970.

[6] G.T. Ruck, D.E. Barrick, W.D. Stuart, C.K. Krichbaum, *Radar Cross Section Handbook, Volume 2*, Plenum Press, New York, 1970.

[7] L.J. du Toit, J.H. Cloete, "Electric Screen Jauman Absorber Design Algorithms," *IEEE Transactions on Microwave Theory and Techniques*, vol. 44, no. 12, pp. 2238-2245, Dec 1996.

[8] B. Chambers, A. Tennant, "Optimised design of Jaumann radar absorbing materials using a genetic algorithm," *IEE Proceedings - Radar, Sonar and Navigation*, vol. 143, no. 1, pp. 23-30, 1996.

[9] B. Chambers, A. Tennant, "Design of wideband Jaumann radar absorbers with optimum oblique incidence performance," *Electronics Letters*, vol. 30, no. 18, pp. 1530-1532, 1994.

[10] A. Kazemzadeh, A. Karlsson, "Multilayered Wideband Absorbers for Oblique Angle of Incidence," *IEEE Transactions on Antennas and Propagation*, vol. 58, no. 11, pp. 3637-3646, Nov 2010.

[11] A. Kazemzadeh, A. Karlsson, "Capacitive Circuit Method for Fast and Efficient Design of Wideband Radar Absorbers," IEEE Transactions on Antennas and Propagation, vol. 57, no. 8, pp. 2307-2314, August 2009.

[12] A. Kazemzadeh, "Thin Wideband Absorber with Optimal Thickness," *2010 URSI Int. Symp. on Electromagnetic Theory (EMTS)*, pp. 676-679, 2010.

[13] B.A. Munk, P. Munk, J. Pryor, "On Designing Jaumann and Circuit Analog Absorbers (CA Absorbers) For Oblique Angle of Incidence," *IEEE Transactions on Antennas and Propagation*, vol. 55, no. 1, pp. 186-193, Jan 2007.

[14] Y. Kazantsev et. al., "Broadening of Operating Frequency Band of Magnetic-Type Radio Absorbers by FSS Incorporation," *IEEE Transactions on Antennas and Propagation*, vol. 58, no. 4, pp. 1227-1235, April 2010.

[15] J. Yang, Z. Shen, "A Thin and Broadband Absorber Using Double-Square Loops," *IEEE Ant. and Wireless Prop. Letters*, vol. 6, pp. 388-391, 2007.

[16] X.Wang, D.H.Werner, "Multiband Ultra-Thin Electromagnetic Band-Gap and Double-Sided Wideband Absorbers based on Resistive Frequency Selective Surfaces," *IEEE Ant. and Prop. Society Int. Symp.*, APSURSI '09, pp. 1-4.

[17] W. Tang, Z. Shen, "Simple Design of thin and wideband circuit analogue absorber," *Electronics Letters*, Vol. 43, No. 12, pp. 689-691, June 2007.

[18] X. Wang, D.H. Werner, "Multiband ultra-thin electromagnetic band-gap and double-sided wideband absorbers based on resistive frequency selective surfaces," *Antennas and Propagation Society Int. Symp 2009, APSURSI '09*, pp. 1-4, 2009.

[19] F. Terracher, G. Berginc, "Thin Electromagnetic Absorbers using Frequency Selective Surfaces," *IEEE Antennas and Propagation Society Int. Symp.*, vol. 2, pp. 846-849, 2000.

[20] S. Chakravarty, R. Mittra, N.R. Williams, "On the Application of the Microgenetic Algorithm to the Design of Broad-Band Microwave Absorbers Comprising Frequency-Selective Surfaces Embedded in Multilayered Dielectric Media," *IEEE Trans. on Microwave Theory and Techniques*, vol. 49, no. 6, pp. 1050-1059, June 2001.

[21] J.-C. Iriarte, I. Ederra, R. Gonzalo, P. de Maagt, "Dual Band RCS Reduction Using Planar Technology by Combining AMC Structures," *EuCAP 2009, 3rd European Conference on Antennas and Propagation*, pp. 3708-3709, 2009.

[22] M. Paquay, J.-C. Iriarte, I. Ederra, R. Gonzalo, P. de Maagt, "Thin AMC Structure for Radar Cross-Section Reduction," *IEEE Trans. Ant. Prop.*, vol. 55, no. 12, pp. 3630-3638, Dec 2007.

[23] F. Costa, A. Monorchio, G. Manara, "Analysis and Design of Ultra Thin Electromagnetic Absorbers Comprising Resistively Loaded High Impedance Surfaces," *IEEE Trans. Ant. Prop., vol. 58, no. 5, pp. 1551-1558, May 2010.*

[24] J.C. Iriarte, I. Ederra, R. Gonzalo, P. de Maagt, "Dual Band RCS Reduction Using Planar Technology by Combining AMC Structures," *3rd European Conference on Antennas and Propagation, EuCAP 2009*, pp. 3708-3709, 2009.

[25] R.R. Ohs, G.J. Skidmore, G. Bedrosian, "Modeling the Effects of Wind Turbines on Radar Returns," *The 2010 Military Communications Conference, MILCOM 2010*, 2010, pp. 272-276.

[26] B.C. Brock, *Scattered EM Field Due to Rotating Blades of Horizontal-Axis Wind Machines*, Sandia National Laboratories report, SAND79-0434, Albuquerque, March 1979.

[27] F. Kong, Y. Zhang, R. Palmer, Y. Bai, "Wind Turbine radar signature characterization by laboratory measurements," *2011 IEEE Radar Conference*, pp. 162-166, 2011.

[28] Y. Zhang et. al., "Using Scaled Models for Wind Turbine EM Scattering Characterization: Techniques and Experiments," *IEEE Trans. on Instrumentation and Measurement*, Vol. 60, No. 4, pp. 1298-1306, 2011.

[29] B.M. Kent et. al., "Dynamic Radar Cross Section and Radar Doppler Measurements of Commercial General Electric Windmill Power Turbines Part 1: Predicted and Measured Radar Signatures," *IEEE Antennas and Propagation Magazine*, Vol. 50, No. 2, pp. 211-219, 2008.

[30] Y.F. Lok, J. Wang, A. Palevsky, "Simulation of radar signal on wind turbine," *2010 IEEE Radar Conference*, pp. 538-543, 2010.

[31] R. Rudd, B. Rhandawa, "RCS Measurement ofWind Turbines," *3rd European Conference on Antennas and Propagation, 2009*, pp. 3642-3644, 2009.

[32] I. Angulo et. al., "Methodology for the empirical analysis of the scattering signals from a wind turbine," *Loughborough Antennas & Propagation Conference*, 2009, pp.553-556, 2009.

[33] A.C. Casanova, M.C. Ramon, L. de Haro y Ariet, P. Gonzalez, "Wind Farming interference effects," International Multi-Conf. on Systems, Signals and Devices, 2008, pp.1-6, 2008.

[34] I. Etayo, A. Satrustegui, M. Yabar, F. Falcone, A. Lopez, "Analysis of the frequency and time variation of radio signals scattered by a Wind Turbine," *2010 Proc. 4th European Conf. on Antennas and Propagation, pp. 1-3, 2010.*

[35] A. Naqvi, S. Yang, H. Ling, "Investigation of Doppler Features From Wind Turbine Scattering," *IEEE Antennas and Wireless Propagation Letters*, Vol. 9, pp. 485-488, 2010.

[36] L.S. Rashid, A.K. Brown, "RCS and radar propagation near offshore wind farms," *2007 IEEE Antennas and Propagation Soc. Int. Symp.*, pp. 4605-4608, 2007.

[37] M. Brenner, *Wind Farms and Radar*, prepared by the Mitre Corporation for the US Department of Homeland Security, January 2008.

[38] J.C.G. Matthews, C. Sarno, R. Herring, "Interaction between radar systems and wind farms," *2008 Antennas and Propagation Conference, p*p. 461-464, 2008.

[39] C. Lute, W. Wieserman, "ASR-11 radar performance assessment over a wind turbine farm," *2011 IEEE Radar Conference*, pp. 226-230, 2011.

[40] A. Theil, M.W. Schouten, A. de Jong, "Radar and wind turbines: A guide to acceptance criteria," *2010 IEEE Radar Conference, pp. 1355-1361*, 2010.

[41] A. Theil, L.J. van Ewijk, "Radar Performance Degradation due to the Presence of Wind Turbines," *2007 IEEE Radar Conference*, pp. 75-80, 2007.

[42] P. Tognolatti, A. Orlandi, "Analysis of the EMI impact of an array of wind generators on the performances of secondary surveillance radar system," *EMC Europe, 2008 Int. Symp. On Electromagnetic Compatibility*, pp. 1-4, 2008.

[43] G. Greving,W. Biermann, R. Mundt, "Wind turbines as distorting scattering objects for radar - clutter aspects and visibility," *11th International Radar Symposium 2011*, pp. 1-4, 2010.

[44] S. Turner, C. New, "Assessing the impact of wind farms on radar systems," *IET Seminar on Electromagnetic Propagation in Structures and Buildings*, 2008, pp. 1-15, 2008.

[45] E. Van Lil, D. Trappeniers, J.-w. De Bleser, A. Van de Capelle, "Computations of radar returns of wind turbines," 3rd European Conference on Antennas and Propagation, 2009, pp. 3852-3856, 2009.

[46] L.S. Rashid, A.K. Brown, "Impact modelling of wind farms on marine navigational radar," *2007 IET International Conference on Radar Systems*, pp. 1-5, 2007.

[47] G.J. Poupart, *Wind Farms Impact on Radar Aviation Interests - Final Report*, prepared by the QinetiQ Corporation for the Department of Trade and Industry, U.K., Sept 2003.

[48] Defense Technology Strategy for the Demands of the 21st Century, *The effects of wind turbine farms on ATC radar*, prepared for The Air Warfare Center, RAF, U.K., May 10, 2005.

[49] A. Belmonte, X. Fabregas, "Analysis of Wind Turbines Blockage on Doppler Weather Radar Beams," *IEEE Antennas and Wireless Propagation Letters*, Vol. 9, pp. 670-673, 2010.

[50] K.V. Mishra, V. Chandrasekar, "Signal analysis and modeling of wind turbine clutter in weather radars," *2010 IEEE Int. Geoscience and Remote Sensing Symp. (IGARSS)*, pp. 3561- 3564, 2010.

[51] F. Darcy, D. de la Vega, "A methodology for calculating the interference of wind farm on weather radar," *2009 Loughborough Antennas & Propagation Conference (LAPC)*, pp. 665- 667, 2009.

[52] B. Hernando, J.M. Ferreras, F. Martinez, F. Encabo, "Wind turbine clutter observations and theoretical validation for meteorological radar applications," *2010 IEEE Radar Conference*, Vol. 5, No. 2, pp. 111-117, 2011.

[53] B. Hernando, F. Martinez, F. Encabo, "Statistical characterization of wind turbine clutter in C-band radars," *2008 International Conference on Radar*, pp. 360-364, 2008.

[54] M.M. Butler, D.A. Johnson, *Feasibility of Mitigating the Effects of Windfarms on Primary Radar*, prepared by Alenia Marconi Systems Limited for the U.K. Department of Trade and Industry, 2003.

[55] L. Sergey et. al., "Advanced mitigating techniques to remove the effects of wind turbines and wind farms on primary surveillance radars," *2008 IEEE Radar Conference*, pp. 1-6, 2008.

[56] B. Hernando, F. Martinez, F. Encabo, "Detection and mitigation of wind turbine clutter in C-band meteorological radar," *IET Radar, Sonar & Navigation*, Vol. 4, No. 4, pp. 520-527, 2010.

[57] R.D. Palmer, "Wind turbine clutter mitigation using fully adaptive arrays," *2008 European Radar Conference*, pp. 356-359, 2008.

[58] C.A. Jackson, M.M. Butler, "Options for mitigation of the effects of windfarms on radar systems," *2007 IET International Conference on Radar Systems*, pp. 1-6, 2007.

[59] E. Aarholt, C.A. Jackson, "Wind farm Gapfiller concept solution," *2010 European Radar Conference (EuRAD)*, pp. 236-239, 2010.

[60] J. Perry, A. Biss, "Wind Farm Clutter Mitigation in Air Surveillance Radar," *IEEE Aerospace and Electronic Systems Magazine*, Vol. 22, No. 7, pp. 35-40, 2007.

[61] C.A. Jackson, M.M. Butler, "Options for mitigation of the effect of wind farms on radar systems," IET International Conference on Radar Systems 2007, October 2007.

[62] Spaven Consulting, *Wind Turbines and Radar: operational experience and mitigation measures*, report to a consortium of wind energy companies, December 2001.

[63] Office of the Director of Defense Research and Engineering, *The Effect of Windmill Farms on Military Readiness*, report to The Congressional Defense Committees, 2006.

[64] Janetos Georgopoulos et. al., *Assessing radar mitigation options for wind farm developers*, prepared by Pager Power Unlimited, U.K. for EWEC 2009, March 17, 2009.

[65] V. Peesapati et. al., "Resolving Performance Conflicts in New Wind Turbine Blade Designs," Supergen V Wind Energy Theme, prepared for the Engineering and Physical Sciences Research Council, UK.

[66] A. Tennant, B. Chambers, "Wind turbine generators with active radar signature control blades," *Proc. of the SPIE*, vol. 5389, pp. 486-495, 2004.

[67] A. Tennant, B. Chambers, "Signature management of radar returns from wind turbine generators," *Smart Materials and Structures*, vol. 15, pp. 468-472, 2006.

[68] B. Chambers, A. Tennant, "Active Dallenbach radar absorber," *IEEE Ant. and Prop. Soc. Int. Symp.*, pp. 381-384, 9-14 July 2006.

[69] A. Tennant, B. Chambers, "Radar signature control of wind turbine generators," *2005 IEEE Antennas and Propagation Society Int. Symp.*, Vol. 4A, pp. 489-492, 2005.

[70] B. Chambers, K.L. Ford, A. Tennant, "Effect of element failure in active coatings for wind turbine generator blades," *2008 IEEE Antennas and Propagation Soc. Int. Symp.*, pp. 1-4, 2008.

[71] J. Pinto et. al., "Radar signature reduction of wind turbines through the application of stealth technology," *Antennas and Propagation. European Conference. 3rd 2009*, 2009, pp. 3886-3890.

[72] J. Pinto, J.C.G Matthews, G.C. Sarno, "Stealth technology for wind turbines," *IEEE Trans. on Instrumentation and Measurement*, Vol. 60, No. 4, pp. 1298-1306, 2011.

[73] J.C.G Matthews, J. Pinto, and C. Sarno, "Stealth solutions to solve the radar-wind farm interaction problem," *2007 Antennas and Propagation Conference*, 2007, pp. 101-104.

[74] L. Rashid, A. Brown, "Partial Treatment of Wind Turbine Blades with Radar Absorbing Materials (RAM) for RCS Reduction," *2010 Proc. Fourth European Conf. on Antennas and Propagation*, 2010, pp. 1-5. 49

[75] S.G. Appleton, *Design and Manufacture of Radar Absorbing Wind Turbine Blades – Final Report*, prepared by QinetiQ for the Department of Trade and Industry, U.K., Feb 2005.

[76] H. Knight, "Qinetiq coating allays wind farm fears," *The Engineer*, Vol. 291, No. 7600, May 3, 2002.

[77] Advanced Design System (ADS®) code suite, ver. 2009, Agilent Technologies, 2009.

[78] High Frequency Structure Simulator (HFSS®) code suite, ver. 13.0.1, Ansys Corporation, 2011.

[79] Computer Simulation Technology, Microwave Studio (CST MWS®) code suite, ver. 2011.03, Computer Simulation Technology, 2011.

[80] Xpatch® code suite, ver. 4.10, SAIC / DEMACO, a division of Science Applications International Corporation, 2010.

[81] J.R. Wait, *Electromagnetic Wave Theory*, Harper & Row, New York, 1985.

[82] C. Sudhendra, V. Mahule, A. Mohanty, "A Novel Space Cloth Using Resistor Grid Network for Radar Absorbers in Stealth Applications," *International Conference on Communications and Signal Processing*, pp. 83-86, 2011.

[83] W.E. Patitz, B.C. Brock, E.G. Powell, *Measurement of Dielectric and Magnetic Properties of Soil*, Sandia National Laboratories report, SAND95-2419, Albuquerque, Nov 1995.

[84] A.M. Nicolson, G.F. Ross, "Measurement of the Intrinsic Properties of Materials by Time-Domain Techniques," *IEEE Trans. On Instrumentation and Measurement*, vol. IM-19, no. 4, pp. 377-382, Nov 1970.

[85] W.B. Weir, "Automatic Measurement of Complex Dielectric Constant and Permeability at Microwave Frequencies," *Proceedings of the IEEE*, vol. 62, no. 1, pp. 33-36, Jan 1974.

[86] A. Boughriet, C. Legrand, A. Chapoton, "Noniterative Stable Transmission/Reflection Method for Low-Loss Material Complex Permittivity Determination," *IEEE Trans. Microwave Theory and Tech.*, vol. 45, no. 1, pp. 52-57, Jan 1997.

[87] P.G. Bartley, S.B. Begley, "A New Technique for the Determination of the Complex Permittivity and Permeability of Materials," *2010 IEEE Instrumentation and Measurement Technology Conference*, pp. 54-57, Jan 2010.

[88] T. Hayashi, Y. Hirai, H. Tanaka, and T. Nishi, "Frequency-Dependent Conductivity in Polyaniline," *Japanese Journal of Applied Physics*, Vol. 26, No. 11, pp. L1800-L1802, Novvember 1987.

[89] H. Hovhannisyan et. al., "Investigation of polyaniline-based microwave absorbing nanocomposites," *34th European Microwave Conference, 2004*, vol. 2, pp. 793-794, 2004.

[90] D.S. Hecht, L. Hu, G. Gruner, "Electronic properties of carbon nanotube/fabric composites," *Current Applied Physics*, September 2005.

[91] N. Zhao, T. Zou, C. Shi, J. Li,W. Guo, "Microwave absorbing properties of activated carbonfiber felt screens (Vertically-arranged carbon fibers)/epoxy resin composites," *Materials Science and Engineering:B*, Vol. 127, No. 2-3, pp. 207-211, 25 February 2006.

[92] C.P. Neo, V.K. Varadan, "Optimization of Carbon Fiber Composite for Microwave Absorber," *IEEE Transactions on Electromagnetic Compatibility*, Vol. 46, No. 1, pp. 102-106, February 2004.

[93] K.A. Jose, Y. Sha, V.K. Varadan, C.P. Neo, "FSS embedded microwave absorber with carbon fiber composite," *IEEE Ant. and Prop. Society Int. Symp.*, vol. 2, pp. 576-579, 2002.

[94] A. Saib et. al., "Carbon Nanotube Composites for Broadband Microwave Absorbing Materials," *IEEE Trans. Microwave Theory and Tech.*, vol. 54, no. 6, pp. 2745-2754, June 2006.

[95] D. Micheli et. al., "Broadband Electromagnetic Absorbers Using Carbon Nanostructure- Based Composites," *IEEE Trans. Microwave Theory and Tech.*, vol. 54, no. 6, pp. 2745-2754, June 2006.

[96] Haiyan Zhang, et al, "Electromagnetic characteristic and microwave absorption properties of carbon nanotubes/epoxy composites in the frequency range from 2 to 6 GHz", J. Appl. Phys. 105, 054314 (2009); available http://dx.doi.org/10.1063/1.3086630.

[97] Roger F. Harrington, *Time-harmonic Electromagnetic Fields*, McGraw-Hill Book Co., New York, 1961, 1987.

[98] John D. Kraus, *Electromagnetics,* third edition, McGraw-Hill Book Co., New York, 1984.

[99] Constantine A. Balanis, *Advanced Engineering Electromagnetics*, John Wiley & Sons, Inc., New York, 1989.

[100] H. Ling, R. Chou, S. Lee, "Shooting and bouncing rays: Calculating RCS of an arbitrary cavity", *Digest of the IEEE Antennas and Propagation Society 1986 International Symposium*, Vol. 24, June 1986, pp 293-296.

[101] Hao Ling, Ri-Chee Chou, and Shung-Wu Lee, "Shooting and Bouncing Rays: Calculating the RCS of an Arbitrarily Shaped Cavity", *IEEE Trans. Antennas and Propagation*, Vol 37, No. 2, February 1989, pp 194–205.

[102] Prabhakar H. Pathak,and Robert J . Burkholder, "Modal, Ray, and Beam Techniques for Analyzing the EM Scattering by Open-Ended Waveguide Cavities", *IEEE Trans. Antennas and Propagation*, Vol 37, No. 5, May 1989, pp 635–647.

[103] Rajan Bhalla and Hao Ling, "A Fast Algorithm for Signature Prediction and Image Formation Using the Shooting and Bouncing Ray Technique", *IEEE Transactions On Antennas And Propagation*, Vol. 43, No. 1, July 1995, pp 727-731.

[104] A. M. Marzougui, S. J. Franke, "Scattering from rough surfaces using the `shooting and bouncing rays' (SBR) technique and comparison with the method of moments solutions", *IEEE Antennas and Propagation Society International Symposium, 1990, AP-S Digest 'Merging Technologies for the 90's'*, vol.4, 7-11 May 1990 pp 1540-1543.

[105] Fred. E. Nathanson, *Radar Design Principles,* 2nd edition, McGraw-Hill, Inc., New York, 1991.

[106] Merrill I. Skolnik, ed., *Introduction to Radar Systems,* 2nd edition, McGraw-Hill Book Co., New York, 1980.

[107] Alan V. Oppenheim and Ronald W. Schafer, *Digital Signal Processing,* Prentice-Hall, Inc., Englewood Cliffs, New Jersey, 1975.

[108] Alan V. Oppenheim, Alan S. Willsky, with Ian T. Young, *Signals and Systems*, Prentice-Hall, Inc., Englewood Cliffs, New Jersey, 1983.

Appendix I – Brief Discussion of Alternate Absorptive Methods

Mono-static RCS reduction of wind-turbine blade can be accomplished by controlling the way impinging electromagnetic waves deflect from, pass though, and flow around the blade with various degrees of attenuation. Regardless of the details of the method, in all cases it is necessary to provide a good impedance match at the outer surface to reduce the back-scattered field.

The design approach applied thus far provides impedance matching through phase cancellation using resonant structures, and introduces absorption by way of resistive sheets sandwiched in between discrete multi-layer dielectrics having various values of relative permittivity, ε_r, with the entire structure backed by a conductive sheet to stop the pass through. Sheet resistivity typically decreases from front to back, typically following a quadratic taper [I-1]. Fractional bandwidth of the absorber can be increased by increasing thickness in these designs. At low frequencies greater thickness is required, but thickness may be reduced by using magnetic materials with relative permeability, μ_r, greater than unity. For example, ECCOSORB® SF is a series of commercially available magnetically loaded, thin, but heavy, resonant absorbers that are designed for use in the 2 GHz to 18 GHz range, claiming –20 dB RCS reduction when backed by a metal surface [I-2]. Frequency tuning is accomplished by adjusting thickness, with increasing thickness and weight required for lower frequencies. Although these commercial materials are not directly suitable for current blade construction, we are evaluating the feasibility of incorporating magnetic particles into the resin of the glass composites.

Another way of introducing absorption is to control the complex impedance of the various dielectric layers. Impedance matching is accomplished, not by resonant means, but by gradually tapering the impedance from a value close to the free-space value to some desired terminal impedance. Absorption is achieved through the imaginary part of the refractive index, $\sqrt{\mu_r \varepsilon_r}$. At lower frequencies, magnetic losses, introduced through complex values of permeability, are needed. Designs using permittivity gradient alone require a minimum of 0.3 free-space wavelengths thickness in order to reach 20 dB RCS reduction [I-1]. At 2.8 GHz, this corresponds to 32 mm (1.25 in). Hence, magnetic loss is a must to reduce the thickness further, but this will again increases weight. A commercial product that utilizes an impedance gradient is ECCOSORB® AN, which is a series of microwave absorbers, claiming better than –17 dB RCS reduction, made from polyurethane foam that is treated with carbon to generate a controlled conductivity gradient [I-2]. This product uses only a complex permittivity gradient, without any magnetic materials, and is thus relatively thick at low frequencies. Although light-weight compared to magnetic materials, in this form it is not suitable for use with wind-turbine blades.

In comparing the merits of resonant designs to those of graded index methods, one must take into account methods of construction. Although the graded index method does not require laying down layers of impedance sheets, the approach may not be compatible with or supported by current construction processes.

Finally, certain regions of the blade, such as the tip and trailing edges, are thin with respect to the wavelength. In these regions, frequency-selective-surface (FSS) techniques [I-3] may be employed to provide an impedance match at the incident surface, and thus enhance transmission through the blade, but with low absorption. Similarly, circuit-analog absorber (CAA) methods [I-3] can be used to introduce reactive components to the sheet impedance, providing additional design freedom.

It is likely that some of the above concepts may conflict with specified constraints. However, examining performance limits that can be obtained if certain constraints are relaxed may pave the way for novel future turbine design possibilities.

[I-1] E. F. Knott, J. F. Shaeffer, and M. T. Tulley, *Radar Cross Section Its Prediction, Measurement and Reduction*, Dedham, MA: Artech House, 1985

[I-2] Emerson & Cuming Microwave Products, a wholly-owned subsidiary of Microwave Materials Group (MMG), Geel, Belgium. Available: http://www.eccosorb.eu/eccosorb-0

[I-3] B.A. Munk, *Frequency Selective Surfaces: Theory and Design*, John Wiley & Sons, New York, 2000.

Appendix II – Dielectric model for mixture with electrically conducting component

When two materials are combined in a mixture, it is desirable to estimate the effective permittivity of the mixture. Consider the situation when one of the materials is electrically conducting. A complex electric permittivity can be defined for a conducting material,

$$\varepsilon = \varepsilon' - j\,\sigma/\omega\,,$$

where ε is the real part of the permittivity, σ is the conductivity, and $\omega = 2\pi f$ is the radian frequency of the electric field.

Let $\varepsilon_1 = \varepsilon_1'\varepsilon_0 - j\,\sigma_1/\omega$ and $\varepsilon_2 = (\varepsilon_2' - j\varepsilon_2'')\varepsilon_0$ where ε_0 is the permittivity of free space[5]. The relative permittivity of a mixture containing x volume fraction of the first material is given by[6]

$$\varepsilon_{mix} = \left(\varepsilon_1' - j\frac{\sigma_1}{\varepsilon_0\omega}\right)^x \left(\varepsilon_2' - j\varepsilon_2''\right)^{1-x}.$$

When the first material is sufficiently conductive that $\sigma_1 >> \varepsilon_1'\varepsilon_0\omega$, then[7]

$$\varepsilon_{mix} \cong (-j)^x \left(\frac{\sigma_1}{\varepsilon_0\omega}\right)^x \varepsilon_2'^{1-x}.$$

Notice that the real part of the first permittivity is irrelevant when the conductivity is large. Since $-j = e^{\,j(\pi/2\ \ 2n\pi)} = \cos(\pi/2 + 2n\pi) - j\sin(\pi/2 + 2n\pi),\ \ n \in \mathit{Integers}$, we see

$$(-j)^x = e^{\,jx(\pi/2\,|\,2n\pi)} = \cos(x\pi/2 + 2xn\pi) - j\sin(x\pi/2 + 2xn\pi),\ \ n \in \mathit{Integers}.$$

The question arises: What is the correct value for n? Consider that $0 \le x \le 1$. If n takes any integer value other than $n = 0$, the real and imaginary parts will change sign as x is varied, as indicated in Figure 100. Since that would not be consistent with a physically realizable material, it is necessary to set $n = 0$. Thus, the relative dielectric permittivity of the mixture containing a conducting material can be approximated as

$$\varepsilon_{mix} \cong (-j)^x \left(\frac{\sigma_1}{\varepsilon_0\omega}\right)^x \varepsilon_2'^{1-x} = \left(\frac{\sigma_1}{\varepsilon_0\omega}\right)^x \varepsilon_2'^{1-x} \left(\cos(x\pi/2) - j\sin(x\pi/2)\right).$$

---

[5] The constants for the electromagnetic field are:

$$\varepsilon_0 = \frac{1}{\mu_0 c^2} \cong 8.854\cdot 10^{-12}\ \text{F/m},\quad \mu_0 = 4\pi\cdot 10^{-7}\ \text{H/m},\quad c = 299,792,458\ \text{m/s}$$

[6] Based on Lichtenecker logarithmic mixing formula, $\ln\varepsilon_{mix} = x\ln\varepsilon_1 + (1-x)\ln\varepsilon_2$ (see section 4.3.1)

[7] Applying the binomial theorem to expand the powers,

$$\varepsilon_{mix} = \left(\varepsilon_1' - j\frac{\sigma_1}{\varepsilon_0\omega}\right)^x \left(\varepsilon_2' - j\varepsilon_2''\right)^{1-x} = (-j)^x \left(\frac{\sigma_1}{\varepsilon_0\omega}\right)^x \varepsilon_2'^{1-x} \left(1 + j\frac{\varepsilon_1'\varepsilon_0\omega}{\sigma_1}\right)^x \left(1 - j\frac{\varepsilon_2''}{\varepsilon_2'}\right)^{1-x}$$

$$= (-j)^x \left(\frac{\sigma_1}{\varepsilon_0\omega}\right)^x \varepsilon_2'^{1-x} \left(1 + jx\frac{\varepsilon_1'\varepsilon_0\omega}{\sigma_1} + \frac{1}{2}x(1-x)\frac{\varepsilon_1'^2\varepsilon_0^2\omega^2}{\sigma_1^2} + \cdots\right)\left(1 - j(1-x)\frac{\varepsilon_2''}{\varepsilon_2'} + \frac{1}{2}x(1-x)\left(\frac{\varepsilon_2''}{\varepsilon_2'}\right)^2 + \cdots\right) \cong (-j)^x \left(\frac{\sigma_1}{\varepsilon_0\omega}\right)^x \varepsilon_2'^{1-x}$$

d

For graphite, the conductivity ranges from $\sigma = 3.8 \cdot 10^4\ S/m$ to $\sigma = 10^5\ S/m$ [II-1]. A typical epoxy resin might have $\varepsilon_2 = 2.88 - j0.03$. The relative permittivity of a mixture containing epoxy and graphite cloth can be estimated as

$$\varepsilon_{\substack{carbon \\ composite}} \cong \left(\frac{7 \cdot 10^4}{2\pi f \varepsilon_0} \right)^x (2.88 - j0.03)^{(1-x)} \left(\cos(x\pi/2) - j \sin(x\pi/2) \right). \qquad \text{(II-1)}$$

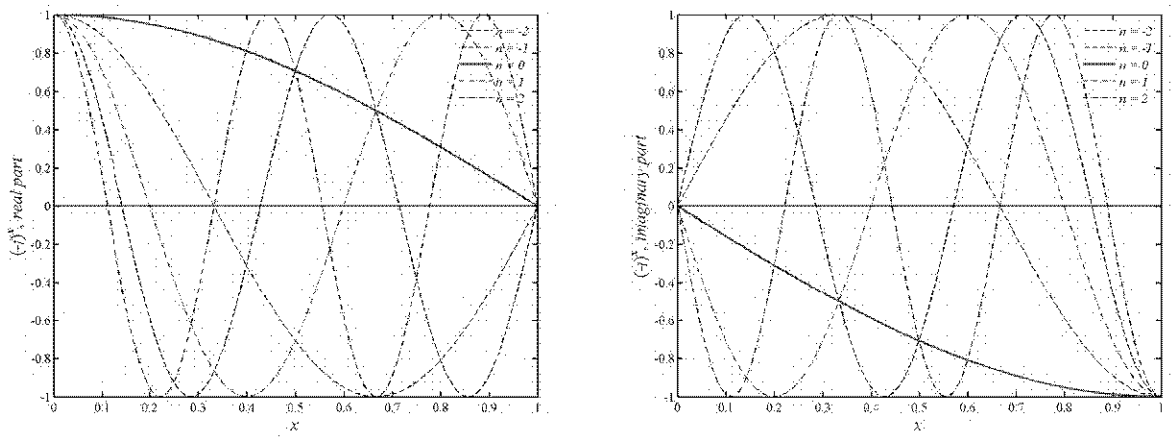

Figure 100 Real (left) and imaginary (right) parts of $(-j)^x$ for several values of n.

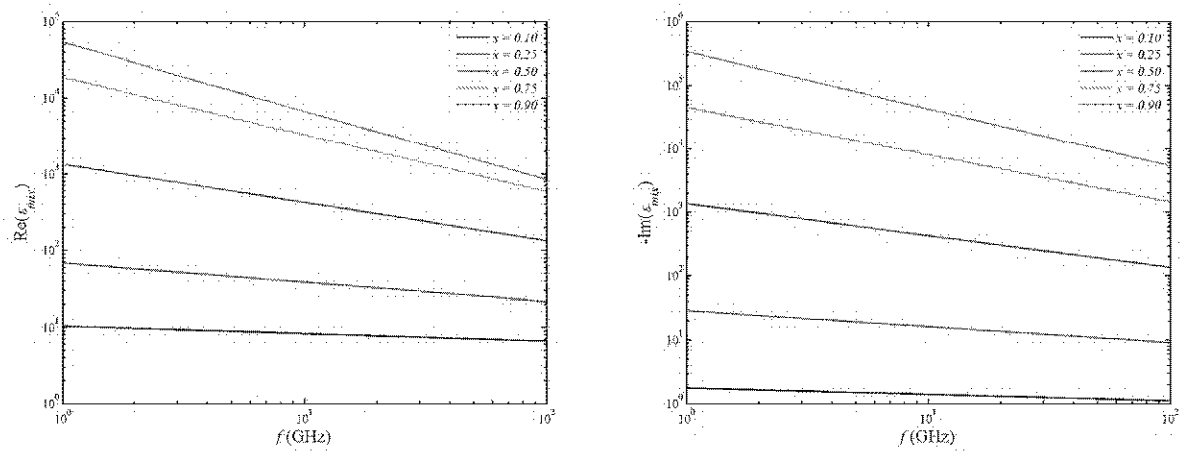

Figure 101 Real (left) and imaginary (right) components of the electric permittivity of a graphite/epoxy mixture computed from (II-1).

Reference

[II-1] K.J. Lodge, "The electrical properties of joints in carbon fibre composites", *Composites*, Volume 13, Issue 3, July 1982, Pages 305-310; available: http://www.sciencedirect.com/science/article/pii/0010436182900143

Appendix III – Nomenclature

AMC	Artificial Magnetic Conductor
CAA	Circuit Analog Absorber
CCA	Capacitive Circuit Absorber
CER	Carbon Enhanced Reinforcement
EM	Electromagnetic
EMI	Electromagnetic Interference
FDTD	Finite Difference Time Domain
FEM	Finite Element Method
GHz	Giga-Hertz
HIS	High Impedance Surface
LO	Low Observable
MHz	Mega-Hertz
PCB	Printed Circuit Board
PEC	Perfect Electrical Conductor
PNA	Programmable Network Analyzer
RAM	Radar Absorbing Material
RCS	Radar Cross Section
RF	Radio-Frequency
SNL	Sandia National Laboratories
TE	Transverse Electric
TM	Transverse Magnetic
VARTM	Vacuum-Assisted Resin-Transfer Molding

Distribution

6 Cece Sterling
Attention : Brian Connor
Michael Derby
Mark Higgins
Jim Ahlgrimm
Jose Zayas
Wind & Hydropower Technologies
EE-2B Forrestal Building
U.S. Department of Energy
1000 Independence Ave. SW
Washington, DC 20585

1 William Van Houten
Office of the Deputy Secretary of Defense (Installations and Environment)
3400 Defense Pentagon
Washington, DC 20301-3400

1	MS 0503	N. Padilla	5343
1	MS 0509	K. D. Meeks	5300
1	MS 0519	S. P. Castillo	5346
1	MS 0519	D. M. Brouhard	5349
1	MS 0519	A. W. Doerry	5349
1	MS 0532	J. J. Hudgens	5340
1	MS 0532	B. L. Burns	5340
1	MS 0532	W. H. Hensley	5344
1	MS 0532	T. J. Trodden	5348
1	MS 0533	S. Gardner	5342
1	MS 0533	K. W. Sorensen	5345
1	MS 0533	D. F. Dubbert	5345
3	MS 0533	S. E. Allen	5345
1	MS 0533	K. C. Branch	5345
5	MS 0533	B. C. Brock	5345
1	MS 0533	T. Christian	5345
1	MS 0533	G. K. Froehlich	5345
1	MS 0533	H. Loui	5345
5	MS 0533	J. J. McDonald	5345
1	MS 0533	W. E. Patitz	5345
1	MS 0533	T. V. Satterthwait	5345
1	MS 0533	M. D. Sena	5345
1	MS 0533	B. H. Strassner	5345
1	MS 1104	J. J. Torres	6120
10	MS 1124	D. G. Minster	6121
1	MS 1124	J. A. Paquette	6121
1	MS 1124	B. R. Resor	6121
1	MS 1349	Paul Clem	1816
1	MS 0958	W. Miller	1833
1	MS 0958	D. A. Calkins	1833
1	MS 0899	RIM-Reports Management	9532 (electronic copy)

Sandia National Laboratories